# TECHNIQUES FOR THE DETECTION OF A NEW PHYSICS SIGNATURE WITH THE CMS EXPERIMENT

A Dissertation

Presented to the Faculty of the Graduate School

of Cornell University

in Partial Fulfillment of the Requirements for the Degree of

Doctor of Philosophy

by

Jennifer Jaye Vaughan

May 2011

TECHNIQUES FOR THE DETECTION OF A NEW PHYSICS SIGNATURE WITH THE CMS EXPERIMENT

Jennifer Jaye Vaughan, Ph.D.

Cornell University 2011

This document investigates experimental and theoretical issues relating to the detection of physics beyond the Standard Model using the Compact Muon Solenoid (CMS).

First, the structure of the CMS detector is reviewed. Particular attention is paid to the hardware and software components of the pixel tracking system. A description is presented of the algorithms that are used to reconstruct physics objects such as electrons and jets.

Next, theoretical motivations are given for seeking new physics processes in the energy regime that is accessible by CMS. Two different theories, the Minimal Supersymmetric Standard Model and the Littlest Higgs model with T-parity, are introduced as extensions of the Standard Model. Their experimental signatures are considered, and a technique for discriminating between them using CMS observations is studied with Monte Carlo computer simulations.

The remainder of the document focuses on a search for evidence of a new physics signature using CMS events that contain two electrons, two jets, and large missing transverse energy. A data-driven technique for estimating the QCD background due to fake electrons is developed, tested, and applied to this channel. The other background estimates are obtained from Monte Carlo simulations, and several sources of systematic uncertainty are surveyed. A correction factor to the Monte Carlo backgrounds is calculated from the electron recon-

struction efficiencies in data and in simulation, which are measured using a tag and probe procedure. A statistical model is developed for propagating all of the background uncertainties to the calculation of the signal. Both Bayesian and semi-frequentist measures of significance are considered. The expected value of the signal is $\langle s \rangle = 0.238 \pm 0.996\ (\text{stat}) \pm 0.304\ (\text{sys})$ events, and its 95% confidence interval is $[0, 4.4]$.

## BIOGRAPHICAL SKETCH

Jennifer Jaye Vaughan received her A.B. in Physics and Mathematics from Bryn Mawr College in 2004. She obtained her Master's and Ph.D. in Physics at Cornell University. Her research experience includes a summer at Fermilab and two years at CERN. Beginning in September 2011, she will be attending the University of Toronto in pursuit of a second Ph.D. in Mathematical Physics.

This document is dedicated to procrastination.

**ACKNOWLEDGEMENTS**

I would like to thank my advisor, Julia Thom, and the members of my Special Committee, Maxim Perelstein and Jim Alexander, for their guidance and support. I am grateful to the research group consisting of Julia Thom, Peter Wittich, Werner Sun, Darren Puigh and Avishek Chatterjee for many helpful suggestions and informative discussions. I also want to thank Steve Demjanenko for his coding expertise. Finally, I thank my mother, Maryann Vaughan, for reminding me of life outside of work, and my father, David Vaughan, for commiserating about computers and keeping my mathematics honest.

## TABLE OF CONTENTS

## LIST OF TABLES

## LIST OF FIGURES

CHAPTER 1

# INTRODUCTION

The Large Hadron Collider (LHC) is the site of the most energetic artificially created particle collisions in the world. It was constructed to investigate the major open questions in particle physics today, such as the existence of the Higgs boson, and the nature of particle interactions at the 1 TeV energy scale, which is the energy regime where theoretical and experimental arguments suggest that physics beyond the Standard Model will be observable. This document surveys several techniques that can be used to observe and identify a new physics signature. These techniques are applied to a sample of early data obtained from the first ten months of LHC operation.

The Compact Muon Solenoid (CMS) is one of four particle detectors in operation at the LHC. All of the data used in this document were obtained from observations taken by CMS. Elementary particles are produced in proton-proton collisions and interact with the different layers of the detector. The interactions are used to reconstruct particle properties such as charge, position and momentum. Chapter 2 contains an overview of the CMS detector subsystems. The pixel tracking system, which is the innermost layer of the detector, is considered in detail, including the hardware components and the structure of the software. Chapter 2 also describes the algorithms through which collision events are reconstructed.

The Standard Model is reviewed in Chapter 3, with emphasis on its use of the Higgs mechanism of spontaneous symmetry breaking to generate mass terms for fermions and gauge bosons. One piece of evidence for the incompleteness of the Standard Model is the scalar Higgs boson mass, which acquires quadrat-

ically divergent quantum corrections. To avoid fine-tuning of the bare mass parameter, a new physics theory is required that cancels these divergences above approximately 1 TeV. Evidence of physics beyond the Standard Model should therefore be within the reach of LHC collisions.

Several theories have been posited regarding the nature of physics beyond the Standard Model. In Chapter 3, two potential new physics theories are described: Supersymmetry, specifically the Minimal Supersymmetric Standard Model (MSSM) and its simplification, Minimal Supergravity (mSUGRA); and the Littlest Higgs model with T-Parity (LHT). These models are based on very different theoretical underpinnings, but they lead to similar phenomenologies.

If a new physics signature is observed at CMS, a crucial question will be whether the observation supports or excludes a particular new physics hypothesis. Chapter 4 presents a study, performed on Monte Carlo simulations, of a technique for model discrimination. This technique is shown to potentially rule out large regions of the LHT parameter space using a set of observations that were generated by the MSSM.

The remaining chapters present an analysis of early CMS observations. Events are considered that contain two electrons, two jets, and large missing transverse energy. This is the decay channel in which a search for a new physics signal is performed. The Standard Model backgrounds in this channel are estimated either from Monte Carlo simulations or by data-driven methods. Chapter 5 describes the signature of interest, and presents an overview of the observations and measurements required for the new physics search.

One set of Standard Model background events occur when hadronic jets

from QCD events are misidentified as electrons in the CMS detector. This effect is difficult to model in computer simulations, so the background must be estimated using a data-driven process. A measurement of the rate at which jets lead to fake electrons is presented in Chapter 6. The fake rate can be used to construct a prediction for the number of fake electrons in a given set of data. Several tests of the accuracy of the fake rate prediction are performed, after which it is used to estimate the fake electron background in the multi-electron channel.

Many sources of systematic uncertainty must be considered when background estimates from Monte Carlo simulations are applied to data. One in particular is the electron reconstruction efficiency, which may be different in data than in simulation. The tag and probe method for measuring the electron reconstruction efficiency is presented in the first half of Chapter 7, and the results are used to construct a correction factor to the Monte Carlo backgrounds. Other systematic uncertainties are also evaluated.

Finally, all of the background estimates must be combined and subtracted from the events in data to determine whether there was a nonzero signal. To assess the statistical significance of the signal, the uncertainties on all of the components of this calculation must be propagated. The second half of Chapter 7 presents a statistical model for performing these calculations. The observation in the multi-electron channel is assessed in two ways: for evidence of a new physics signal, and for compatibility with specific new physics hypotheses from within the mSUGRA parameter space. Although a signal is not conclusively observed, the techniques that are employed will be of continued utility in new physics searches and model discrimination studies as more CMS observations are accumulated.

CHAPTER 2

# THE COMPACT MUON SOLENOID DETECTOR

## 2.1 Detector and Collider Fundamentals

The Compact Muon Solenoid (CMS) detector is one of the general-purpose particle detectors commissioned for use at the Large Hadron Collider (LHC), which is a proton-proton collider in operation at CERN. The LHC occupies an underground tunnel, 27 km in circumference, that crosses the border between Switzerland and France [1]. The CMS detector is located in a cavern 100 m underground outside the town of Cessy.

Under optimal running conditions, the LHC is designed to collide two beams, each of which is composed of protons that have been accelerated to an energy of 7 TeV, for a total center-of-mass energy of $\sqrt{s} = 14$ TeV. A beam consists of 3564 bunches of protons, of which 2808 have real collisions. The bunch crossing rate is 40.08 MHz, which corresponds to 25 ns between bunch crossings. These conditions result in a total instantaneous luminosity of $10^{34}$ $\text{cm}^{-2}\text{s}^{-1}$ [2].

The data considered in this document were obtained during the first physics runs at the LHC, which occurred from March to November 2010. The beams ran at 3.5 TeV each, with instantaneous luminosities from $4 \times 10^{29}$ $\text{cm}^{-2}\text{s}^{-1}$ to $2 \times 10^{32}$ $\text{cm}^{-2}\text{s}^{-1}$ [3]. The total integrated luminosity obtained for this analysis is 33.84 $\text{pb}^{-1}$.

The CMS detector is designed for efficient and accurate particle measurements that can be applied to a wide variety of physics events. From the cen-

ter outward, the detector layers are the tracking system, the electromagnetic calorimeter (ECAL), the hadron calorimeter (HCAL), and the muon system. The tracker and the calorimetry systems are contained within the superconducting solenoid, which is 13 m long and has a 5.9 inner diameter, and generates a 4 T magnetic field. The muon system is outside the solenoid, alternating in layers with the iron plates that guide the return magnetic field. Overall, the detector is 21.6 m in length, 14.6 m in diameter, and weighs 12500 tons [4].

A schematic of the detector is given in Figure 2.1. The detector design is extensively documented in a report by the CMS collaboration, "CMS Physics Technical Design Report, Volume 1: Detector Performance and Software" [5], and more recently in the 2008 *JINST* article "The CMS Experiment at the CERN LHC" [6]. The following descriptions of the detector subsystems and event reconstruction procedures are summaries of information compiled from these reports.

The tracking volume is a cylinder that is 5.8 m in length and 2.6 m in diameter. The system consists of three layers of silicon pixel detectors and ten layers of silicon microstrip detectors. As charged particles pass through the tracker, they interact with the silicon semiconductors. The positions and energies of these interactions are recorded, allowing the trajectories of the particles to be reconstructed. The fine granularity and multiple layers of the tracker allow for precise track reconstruction and good momentum resolution. The inner layers close to the interaction point facilitate b jet and $\tau$ tagging.

The electromagnetic calorimeter uses lead tungstate ($PbWO_4$) crystals, which emit blue-green scintillation light upon interaction with electrons and photons. The light is collected by avalanche photodiodes (APDs) in the barrel,

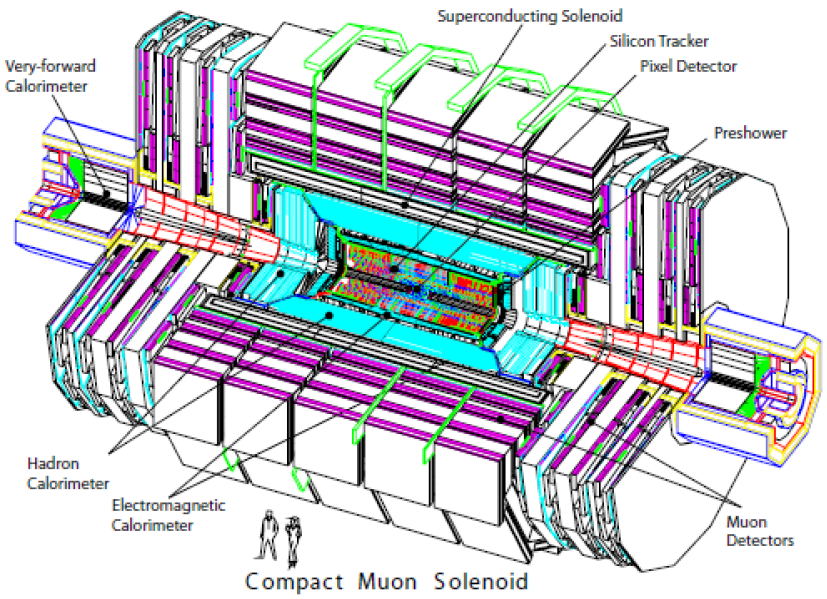


Figure 2.1: Schematic of the CMS detector, with the subdetector systems labeled. Image taken from "The CMS Experiment at the CERN LHC, Section 1.1: Overall concept" [4].

and vacuum phototriodes (VPTs) in the endcap. A preshower system composed of alternating lead layers and silicon strip detectors is positioned in front of the ECAL endcap for $\pi^0$ rejection. The priorities of the ECAL design are to provide wide geometric coverage, and to allow for accurate momentum resolution and efficient photon and lepton isolation.

The hadron calorimeter consists of plastic scintillators alternating with brass or iron absorber plates. The scintillation light is read out by wavelength-shifting (WLS) fibers that are embedded in the scintillator tiles and spliced to clear fibers that lead to the readout system, which is based on hybrid photodiodes (HPDs). Coverage in the very forward region is provided by a steel/quartz fiber calorimeter, and additional calorimetry layers outside of the magnet solenoid serve to increase the effective thickness of the system and improve energy resolution. The combined electromagnetic and hadron calorimetry systems provide

hermeticity and energy resolution for the accurate reconstruction of jets and missing energy.

The muon system consists of three different types of gaseous detectors. Aluminum drift tubes (DT) are in the barrel, and cathode strip chambers (CSCs) are in the endcap. Resistive plate chambers (RPCs) are used in both regions, and provide a second source of position and momentum measurements. Between the detector layers are the iron plates that constitute the magnet return yoke. The CMS detector is particularly well suited to muon identification, charge determination, and momentum resolution.

At the maximum projected instantaneous luminosity, CMS can expect to observe approximately $10^9$ events per second [4]. However, events can be fully recorded at a rate of only 100 Hz. To select those events that are most likely to contain interesting physics, a trigger system is implemented in two levels: the Level 1 trigger and the High Level Trigger. The Level 1 (L1) trigger reduces the event readout to 100 kHz. Because of the speed with which a decision must be rendered, this trigger is implemented in the readout electronics of the calorimetry and muon systems. The High Level Trigger (HLT) performs the remaining reduction in readout to 100 Hz. Its decision is based on event analysis that is performed by software.

The observations taken by the different subdetector systems are used to reconstruct physics objects such as muons, photons, electrons, jets and missing energy. The reconstruction that is performed in real time by the HLT is referred to as online. The more detailed reconstruction that is performed on archived events is referred to as offline. The collection of software that performs these and other tasks for CMS events is called CMSSW. The following sections pro-

vide overviews of the detector components, and of the algorithms that result in reconstructed physics objects.

## 2.2 Coordinate System and Experimental Observables

All kinematic quantities will be measured with respect to the following coordinate system [7]. The origin is the nominal collision point at the center of the CMS detector. The $y$-axis is directed vertically upward. The $x$-axis is directed radially inward with respect to the curve of the LHC tunnel. The $z$-axis is tangential to the beam direction. The azimuthal angle, which is measured from the $x$-axis in the $xy$ plane, is denoted $\phi$. The polar angle, which is measured from the $z$-axis, is denoted $\theta$. The pseudorapidity $\eta$ is defined by

$$\eta \equiv -\ln \tan(\theta/2)\,. \tag{2.1}$$

Using this definition, $\eta \to +\infty$ as $\theta \to 0$, and $\eta \to -\infty$ as $\theta \to \pi$. The transverse plane has an $\eta$ value of zero.

In a proton-proton collision at the LHC, the total energy of each proton is known, but the distribution of that energy amongst the individual partons is not. Therefore, the total energy of the interaction is not a known quantity. However, in the center-of-mass frame, if the beam is aligned correctly, then the net momentum in the $xy$ plane should be zero. Therefore, particular attention is paid to the transverse components of kinematic quantities, which are computed from $x$ and $y$ components. The transverse momentum of a particle is given by

$$p_T = \sqrt{p_x^2 + p_y^2} = p \sin\theta. \tag{2.2}$$

The transverse energy is defined by

$$E_T = E \sin\theta = \frac{E}{p} p_T, \tag{2.3}$$

which suggests that $x$ and $y$ components of energy can be defined by

$$E_x = \frac{E}{p} p_x, \tag{2.4}$$

$$E_y = \frac{E}{p} p_y. \tag{2.5}$$

Using these components, one can perform a vector sum of the transverse energies of different objects. Finally, the transverse mass is defined by

$$m_T = \sqrt{p_x^2 + p_y^2 + m^2}. \tag{2.6}$$

Events can be globally described by taking sums of energy or momentum over all of the reconstructed objects in the event. Of particular interest is the missing transverse energy. If all of the products of a particular collision event are correctly observed and reconstructed, then the net transverse energy in the event should be zero. However, if the event contains a particle such as a neutrino that is not observed by the detector, or if a particle is emitted sufficiently close to the beamline that it does not intersect any of the subsystems, or if one or more of the reconstructed energies are mismeasured, then the net transverse energy will not be zero. The missing transverse energy in an event, $\not{E}_T$, is defined to be the negative of the net transverse energy.

## 2.3 Triggers

The Level 1 trigger and High Level Trigger are designed to reduce the initial rate of inelastic events at CMS from $10^9$ Hz to 100 Hz, which represents the

limit of the rate at which all of the information associated with an event can be recorded [8]. Decisions made by the trigger system must be reached quickly and with accurate identification of potentially interesting physics processes. The hardware and software that perform these tasks are collectively referred to as the Trigger and Data Acquisition System (TriDAS).

The Level 1 trigger makes use of the calorimeters and the muon system. Basic $E_T$ or $p_T$ thresholds are applied to partially reconstructed hits in these systems, which are later used to seed muons, photons, electrons and jets. The L1 trigger also looks at global sums of $E_T$ and $\not{E}_T$. Its output rate is approximately 100 kHz. The L1 trigger is permitted 3.2 $\mu$s to make a decision on any given event. During that time, the rest of the data must be held in buffers. Due to the speed required, decisions are reached within the detector electronics.

If a Level 1 Accept (L1A) is issued, the stored data are sent to front end readout buffers. The Front End Drivers (FEDs), of which there are approximately 600 throughout all of CMS, read out a total of about 75M electronic channels. These event fragments are transferred to the Data Acquisition system (DAQ) by 64-bit serial links (S-Links). The event content received from a FED includes a header that has information identifying the subsystem and the event number. The DAQ Event Builder then assembles all of the fragments associated with a particular event. This information is sent to a Filter Unit upon request, which computes the HLT decision. The Filter Units, of which there are several hundred operating in parallel, are housed on a processor farm. Figure 2.2 shows the flow of information amongst the different components of the trigger system.

There are many different HLTs that an event might satisfy, based on the presence of jets, one or more electrons, one or more photons, one or more muons,

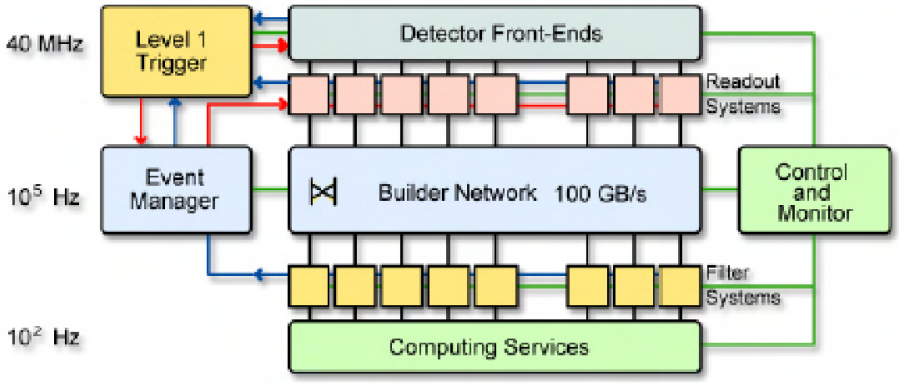


Figure 2.2: Schematic of the trigger system, showing the flow of information between its components. Image taken from "CMS Physics Technical Design Report, Volume 1: Detector Performance and Software, Section 2.3: Event Filter" [9].

total energy, missing energy, or combinations of these features. For example, the `HLT_Jet30U` trigger requires the presence of a jet whose uncorrected $p_T$ is above 30 GeV. The `HLT_Ele15_LW_L1R` trigger requires the presence of an electron that has $p_T > 15$ GeV and that passes certain basic cleaning cuts. The decision associated with each trigger is contained in the event content.

The accepted events are forwarded to the Storage Manager. An event becomes part of one or more primary datasets depending on which triggers it satisfies. The CMS data used in this document come from the jet, photon and electron primary datasets. Once all of the event information has been read out and archived, the offline reconstruction modules can take over. The reconstruction procedures will be described in Section 2.5, following a more detailed discussion of the detector subsystems.

## 2.4 The Detector Subsystems

### 2.4.1 Pixel Tracker: Hardware

The pixel system is the innermost layer of CMS [10]. In the barrel, there are three layers of pixels, which are found at 4.4, 7.3, and 10.2 cm from the beamline. In the forward region, there are two disks in the $+z$ direction and two disks in the $-z$ direction, located at $z = \pm 34.5$ cm and $z = \pm 46.5$ cm. Figure 2.3 shows the layout of the pixel system.

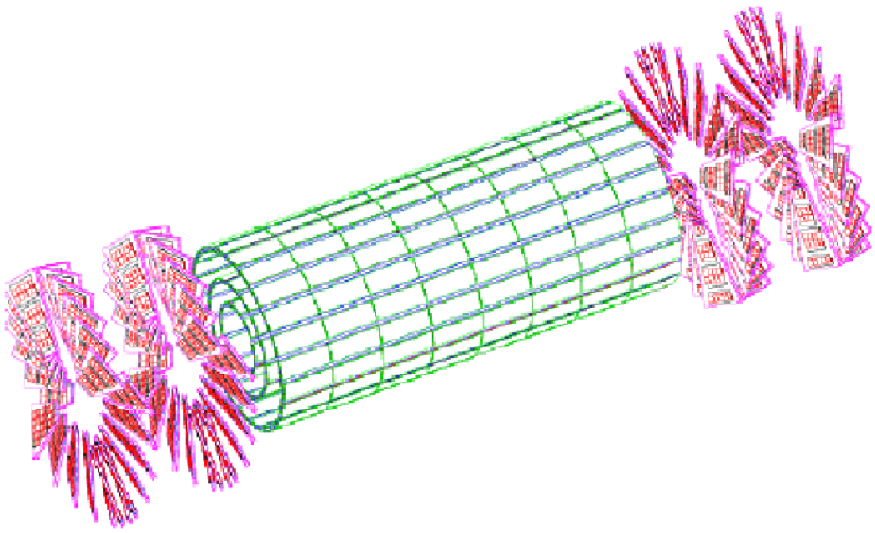

Figure 2.3: Schematic of the pixel system, showing the three layers in the barrel region and two disks in each forward region. Image taken from "CMS Physics Technical Design Report, Volume 1: Detector Performance and Software, Section 1.5: CMS: the overall concept" [11].

The barrel is constructed from modules, where eight modules form a ladder, and ladders and half-ladders form a half-cylinder. Two half-cylinders form one layer of the pixel barrel. In the forward system, seven panels are arranged into a blade. Twenty-four blades, arranged radially as shown in Figure 2.3, form a

disk. In both the barrel and the forward systems, the components are designed to overlap so that charged particles will intersect at least one and probably multiple modules.

One pixel is a silicon semiconductor with an area of $100 \times 150\,\mu\text{m}^2$ [12]. There are 66M pixels in total, giving the pixel detector a total surface area of 1 $\text{m}^2$. The pixels are grouped into read out chips (ROCs), where one ROC consists of 4160 pixels arranged in eighty rows and twenty-six double columns, as shown in Figure 2.4. Each double-column has buffers in which signals are stored until the ROC reads them out. When a charged particle intersects a part of the pixel tracker, it induces a charge in the silicon semiconductor. The charge, the time stamp, and the identity of the pixel that was hit are stored in the buffers associated with that double-column. Hits are read out upon receipt of a Level 1 Accept.

A Token Bit Manager (TBM) manages up to 24 ROCs, which are arranged in a module or a panel. The TBM sends the trigger, clock and other commands such as resets to the ROCs, and it takes in their readouts one at a time. The flow of information between the TBM and the ROCs is illustrated in Figure 2.5, and the layout of a panel is shown in Figure 2.6.

The output of the TBM is an analog signal in which information about the pixel hits is encoded. For example, the pixel address is converted to base six, and the digits are encoded using six predetermined amplitude levels. The ROC address is similarly encoded within a sequence of amplitudes. A single pulse encodes the energy of the observed pixel hit. A sample output from one ROC is shown in Figure 2.7.

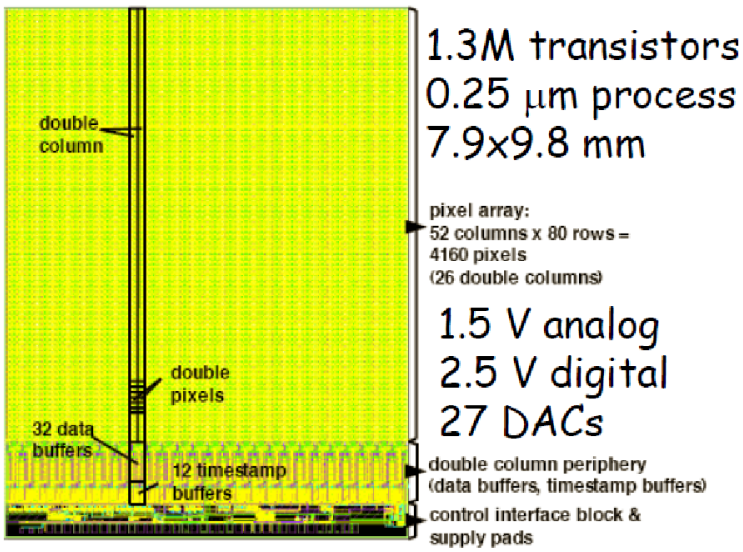


Figure 2.4: A pixel read out chip (ROC), showing a double-column and the data buffers. Image taken from pixel online software reference website [13].

The analog readout proceeds from the TBM to to a Front End Driver (FED) via an Analog Optical Hybrid (AOH). The FED is a circuit board whose firmware decodes all of the information from the ROCs, converts it to digital information, and sends it through a serial link (S-Link) to the DAQ system. The signal from each pixel is contained within a 32-bit word, formatted as follows: 6-bit link id (0-35), 5-bit ROC id (0-23), 5-bit double-column id (0-25), 8-bit pixel ID (0-179), and 8-bit analog to digital conversion (ADC) value which represents the pulse height. The pixel system has 36 FEDs in total, each with its own S-Link.

The process of transmitting calibration information and commands from the online software to the front end electronics begins with a circuit board called the Front End Controller (FEC). It communicates with the TBMs via a pixel Digital Optical Hybrid (pDOH). The pDOH and AOH are both hosted on a portcard, which is responsible for maintaining the correct timing between the

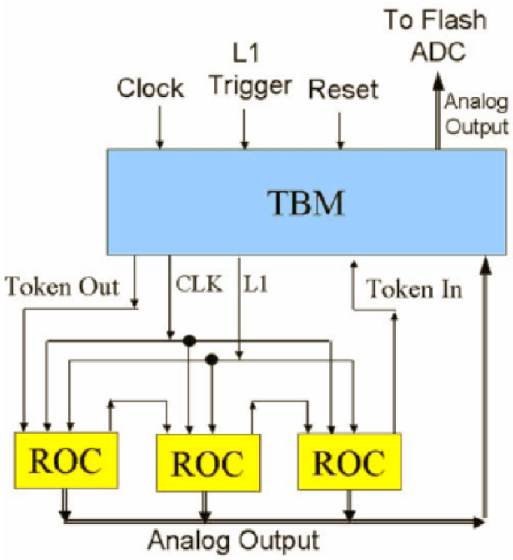


Figure 2.5: Flow of information between a token bit manager (TBM) and the ROCs that it manages. The TBM is responsible for transmitting the clock signal, Level 1 trigger, and reset commands. Image taken from pixel online software reference website [13].

system clock and the transmission of signals. This timing must be calibrated; to that end, a second set of FECs called the Tracker FECs (TKFECs) transmit settings to the portcards via a DOH.

The other circuit boards associated with the pixel system are the Timing and Trigger Controller (TTC) and the Local Trigger Controller (LTC). The primary function of the TTC is to receive the Level 1 Accept from the central trigger controller and pass it to the pixel system. The TTC also transmits the official clock signal, and a set of other CMS-wide commands such as Start, Stop, and Reset [14]. When active physics runs are not being performed, the LTC can take the place of the central trigger and generate the same set of L1As and other commands. This functionality is used to simulate physics running during certain calibration routines.

While the system is running, the hardware is controlled by the Pixel Online

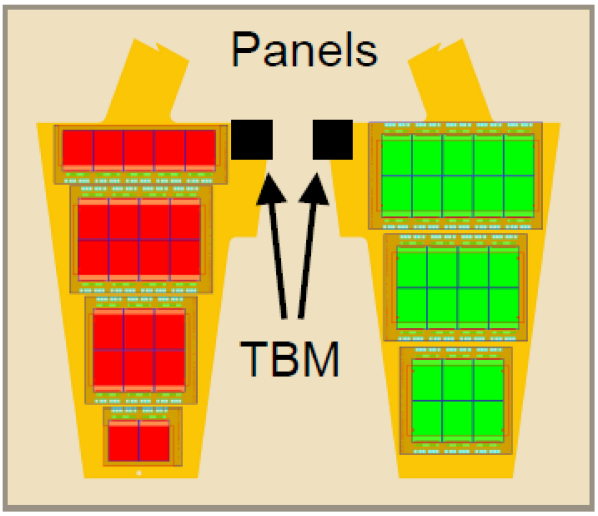


Figure 2.6: Layout of a panel in the forward pixel system. One TBM manages either 21 or 24 ROCs. In the barrel, there is one TBM per module, where it manages either 8 or 16 ROCS. Image taken from pixel online software reference website [13].

Software, which will be described in the next section.

### 2.4.2 Pixel Tracker: Software and Calibrations

Pixel Online Software (POS) [15] refers to software that runs while the pixel system is active, whether during physics runs or while performing calibrations. POS is composed of a hierarchy of C++ applications that operate within the Cross-platform Data Acquisition framework, XDAQ. The top-level application is called PixelSupervisor. It receives its instructions either from the Run Control and Monitoring System (RCMS), or from user inputs via a graphical user interface (GUI).

The level belowPixelSupervisor consists of one XDAQ application for each type of circuit board in the pixel system. Corresponding to the FEDs, FECs

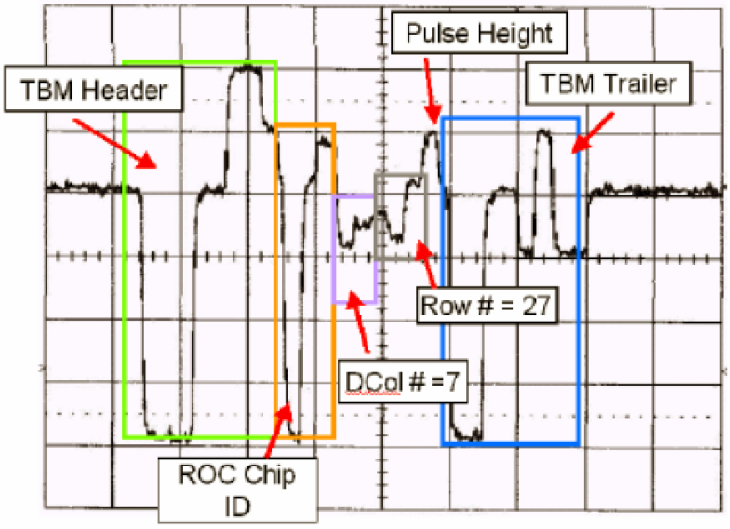


Figure 2.7: Example of analog output from a TBM that has only one ROC. The ROC ID, pixel address, and pulse height of the pixel hit are contained between the TBM header and trailer. Image taken from pixel online software reference website [13].

and TKFECs are the PixelFEDSupervisor, PixelFECSupervisor and PixelTKFEC-Supervisor. The TTC and LTC are operated using the CMS standard software package, in which the XDAQ application is called TTCciControl. The front end circuit boards are housed in VME crates, and the corresponding software applications are hosted on the CPUs that are connected to these crates. The XDAQ framework facilitates communication amongst software that is spread over multiple CPUs. The XDAQ applications communicate with each other via a Simple Object Access Protocol (SOAP).

During physics running, the main purpose of the online software is to maintain coordination with the rest of run control. When the PixelSupervisor receives the command to Configure from RCMS, it uses the pixel configuration database to access the settings for a configuration that is appropriate to physics running, and communicates this choice to the rest of the XDAQ applications.

They in turn transmit the chosen settings to the front end electronics. Similarly, PixelSupervisor receives the other standard RCMS commands such as Start, Pause, Resume, and Halt, and disseminates them to the system components.

More specialized software is dedicated to calibration routines, which are performed prior to the commencement of physics running. Many quantities must be calibrated in order to ensure that information from the pixel system will be encoded and interpreted correctly. Among the necessary calibration routines are:

- The FED address level calibration. Recall that the address of a pixel hit is encoded in six amplitude levels within the analog TBM output. These levels must be calibrated for each ROC so that the addresses can be accurately read.
- The FED phase calibration. The FED interprets the analog signal by sampling from it at a particular point within one clock cycle. This point must be selected so that all features of the signal are observed.
- The FED baseline calibration. The baseline from which voltages are measured must be set in such a way that the entire analog signal is within the dynamic range of the analog to digital converter.
- The PixelAlive, Gain Calibration, and SCurve. These calibrations are executed at the level of the individual pixel. The purpose of the PixelAlive routine is to identify and mask dead pixels. The Gain Calibration and SCurve routines inject a certain charge into the pixel, and measure its efficiency and measured charge, respectively. This information is used to set trim bits and gains for each pixel.

A collection of software classes are used to run all of the calibrations. The coding structure will be discussed in detail in the context of a specific example: the Delay25 calibration.

The Delay25 chip is a component of the portcard, and it controls the relative timing between the system clock and a signal from the FEC to the TBM or vice versa. There are separate delays for signals that are being sent to the TBM and signals that are being returned from it. The settings of the Delay25 chip are controlled by the tracker FEC. In order to calibrate the Send Data and Return Data delays, the calibration routine must transmit Delay25 settings to the TKFEC, and it must instruct the FEC to test communication with a TBM. Therefore, the code that executes this calibration requires access to the PixelFECSupervisor and the PixelTKFECSupervisor.

There are two classes associated with the Delay25 calibration: PixelDelay25Calibration and PixelTKFECDelay25Calibration. Correspondingly, two base classes exist to facilitate the communication between the different components of POS during this calibration: PixelSupervisorConfiguration and PixelTKFECSupervisorConfiguration. These sets of classes perform parallel functions for PixelSupervisor and for PixelTKFECSupervisor.

- PixelSupervisorConfiguration contains all of the addresses needed to send SOAP commands to the Supervisors; both PixelSupervisor and PixelDelay25Calibration inherit from it, and therefore both are able to communicate with all of the subordinate Supervisors.
- PixelTKFECSupervisorConfiguration contains the PixelFECSupervisor SOAP addresses, and the device addresses for the portcards; both PixelTKFECSupervior and PixelTKFECDelay25Calibration inherit from it, and

therefore both are able to communicate with PixelFECSupervisor, and to write new setting information to the portcards.

All calibration routines follow this same basic structure. A calibration has its associated PixelCalibration class, which inherits from PixelSupervisorConfiguration. Optionally, a PixelCalibration class associated with the FED or TKFEC application may also be created, depending on the specific hardware components involved in the calibration.

The calibration procedure begins with the PixelSupervisor GUI, where the user selects a Delay25 calibration. The PixelSupervisor communicates the choice of calibration to the rest of the Supervisors, which call up the associated entry in the pixel configuration database and communicate the settings to the hardware. The PixelSupervisor also creates an instance of the PixelDelay25Calibration class, and the PixelTKFECSupervisor creates an instance of the PixelTKFECDelay25Calibration class.

Once all of the subordinate Supervisors return messages to indicate that configuration is complete, the PixelSupervisor enters the Configured state, and the user has the option to start the calibration. Upon receipt of the Start message, the PixelSupervisor enters the Running state, where it performs the PixelDelay25Calibration::execute() command. This sends a SOAP message to the PixelTKFECSupervisor, which in turn performs the PixelTKFECDelay25Calibration::execute() command. All of the code for the Delay25 calibration routine is located within the latter member function.

The Send Data (SDa) and Return Data (RDa) delays can take on values from 0 to 127, where each step represents 0.5 ns. A delay of 128 units is equivalent to

a delay of 0. The range of possible settings form a 2D grid. The first step in the calibration routine is to perform a scan of the available SDa and RDa settings. A step size of four units is found to strike a good balance between detail and speed. The step size is part of the configuration information for this calibration.

At each test point on the grid, the PixelTKFECDelay25Calibration object writes the SDa and RDa settings in question to the portcard. Next, the PixelTKFECDelay25Calibration object sends a SOAP message to the PixelFECSupervisor, instructing it to test its communication with the TBM. The PixelFECSupervisor sends a signal to the TBM, and checks to see whether that information was successfully received. If the signal is not received three times in a row, the point is abandoned. Otherwise, ten successive tests of the communication are performed. The PixelFECSupervisor sends a return SOAP message when the tests are complete, which includes the number of successes. The PixelTKFECDelay25Calibration accumulates a list of all SDa-RDa points that have a perfect communication record; these are the candidate points.

Next, an algorithm is applied to these points to determine the optimal settings. The goal of the algorithm is to select the most stable point possible; that is, a point in the middle of the largest continuous region of good points. The process is complicated by the observation in certain cases of (1) good regions that have gaps in them, or (2) good regions that consist of two discrete pieces. Both of these cases make a simple position average impractical, as the average of all of the good points might be a rejected point.

The final selection is made by an "expanding stable region" (ESR) algorithm. For each candidate, the algorithm asks whether its nearest neighbors on the grid are also good points. Neighboring good points are sought horizontally,

vertically, and on the two diagonals from the candidate point in question. If at least one point passes the test at a particular step, then all of the points that fail are removed from the list of candidates.

If multiple candidate points remain that are surrounded by good neighbors, then the procedure is repeated, now searching for good neighbors at a distance of half of the previous grid size. Similarly, if all of the candidate points fail a particular test, then it is repeated using a smaller step size. If a tie still remains after the step size has been reduced to one unit, then the point is selected that is closest to the center of the grid. Thus, the stable region surrounding the candidate points is pushed outward in all directions, until the point that is returned is in the center of the largest region of good points. Figure 2.8 shows two sample outputs from this algorithm, including the good region and the selected point.

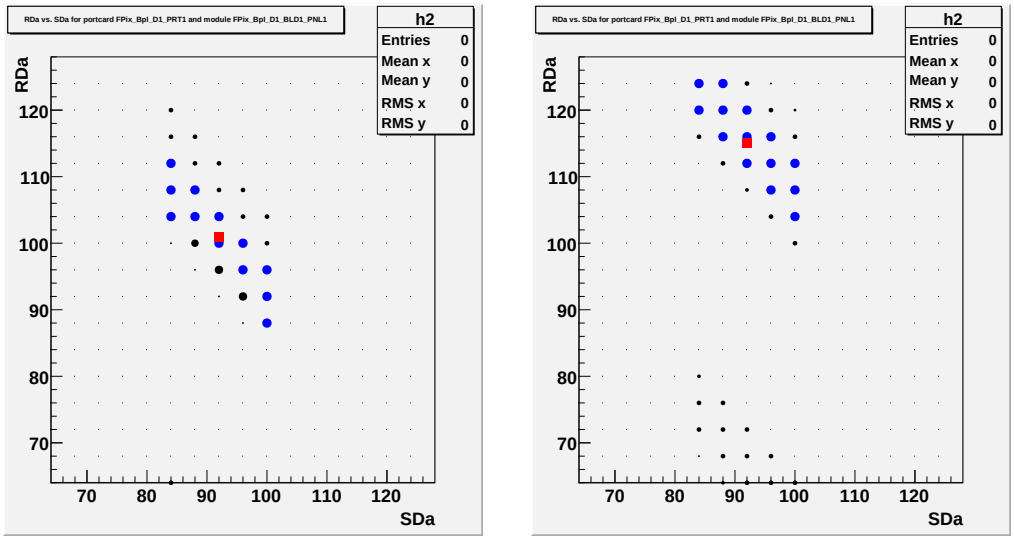


Figure 2.8: Two examples of the expanding stable region algorithm for portcard SDa/RDa settings. The large blue circles represent points with perfect communication, and the red square is the point that was chosen by the algorithm. On the left, the good region is simply connected, and the result of the ESR algorithm is just the position average of all good points. On the right is an example in which the good region might have consisted of two discrete pieces. The ESR algorithm will always select the center of the larger piece.

Once the algorithm has made its selection, the TKFEC updates the settings of the portcard in question to the newly determined optimal point. Unless otherwise specified, the routine is designed to loop over all portcards in the pixel configuration database. Once all portcards have been calibrated, the PixelTKFECDelay25Calibration::execute() function returns. This has the effect of sending a response SOAP message back to the PixelSupervisor, the receipt of which allows the PixelDelay25Calibration::execute() function to return. The user now has the option to send the Halt command, which writes the new settings to the database. At this point, the POS is ready for a new calibration, or to switch to physics running.

### 2.4.3 Silicon Strip Tracker

Surrounding the pixel system is the silicon strip tracking system [16]. The barrel section has a total of ten layers, which are between 25.5 and 116 cm away from the beam line. The endcap section has twelve disks in each of the $+z$ and $-z$ sections that reach up to 280 cm from the interaction point. There are 9.6M silicon strips in the system, and the total surface area of the detector is 200 $m^2$.

The Tracker Inner Barrel (TIB) comprises four of the ten barrel layers. Each layer is divided into four shells, and each shell contains modules that are arranged in strings. The TIB uses the smallest and the thinnest of the silicon strips, with a thickness of 320 $\mu$m, and minimum dimensions of 10 cm $\times$ 80 $\mu$m. They are arranged so that the position of hits can be resolved to within 34 $\mu$m in the $r - \phi$ direction and 230 $\mu$m in the $z$ direction.

The Tracker Outer Barrel (TOB) comprises the remaining six barrel layers. In

this section, which is further from the interaction point and therefore subject to lower radiation levels, the silicon strip sensors are 500 $\mu$m thick, and up to 25 cm $\times$ 180 $\mu$m. The resulting resolution of position measurements is within 52 $\mu$m in the $r - \phi$ direction and 530 $\mu$m in the $z$ direction.

The Tracker End Cap (TEC) has nine disks at distances from 124 cm to 280 cm from the interaction point. Each disk is made of nine petals. Within each petal, the modules are arranged in up to seven rings, which are centered on the beamline. The Tracker Inner Disk (TID) fills the region between the TIB and the TEC. It is divided into three disks, and each disk has modules arranged in three rings. The TID and the three inner rings of the TEC use silicon strips that are 320 $\mu$m thick, and the rest of the TEC uses silicon strips that are 500 $\mu$m thick.

The electronics readout system for the silicon strips shares many features with that of the pixel system. When a charged particle interacts with a silicon strip, the induced charge in the semiconductor is stored, along with the address of the strip in question. This information is transmitted via an analog signal to one of the Front End Drivers for the tracker, where it is digitized and sent on to the global DAQ system.

### 2.4.4 Electromagnetic Calorimeter

The electromagnetic calorimeter (ECAL) [17] is the next layer of the CMS detector after the tracking system. It consists of 61200 lead tungstate ($PbWO_4$) crystals in the central barrel and 7324 crystals in each endcap.

Lead tungstate crystals were chosen because they are dense and they emit

their scintillating light quickly. $PbWO_4$ has a density of 8.28 g/cm$^3$, a radiation length of 0.89 cm, and a Molière radius of 2.2 cm. The crystals emit blue-green scintillation light, with a wavelength maximum at 420 nm. They are expected to emit 80% of their scintillation light within 25 ns. This is on the same time scale as the bunch crossing rate, which makes these crystals appropriate for use in the CMS environment. The crystals have a relatively low light yield ($30\gamma$/MeV), so sensitive photodiodes are needed that will function efficiently in a high magnetic field.

The ECAL barrel (EB) is composed of 36 supermodules, each covering 20° in $\phi$. These are further subdivided into 360 granular segments in $\phi$, and $(2 \times 85)$ segments in $\eta$, covering the range $|\eta| < 1.479$. The result is 61200 crystals in total. The front face of a crystal is at a radius of 129 cm from the interaction point, where its cross sectional area is $22 \times 22$ mm$^2$. This widens to $26 \times 26$ mm$^2$ at the rear face. The total length of a crystal is 230 mm, or 25.8 radiation lengths. Scintillation light is detected by avalanche photodiodes (APDs), which are arranged two to a crystal and have an active surface area of $5 \times 5$ mm$^2$.

The ECAL endcaps (EEs) are situated 315.4 cm from the interaction point, and cover the range $1.479 < |\eta| < 3.0$. A group of $5 \times 5$ crystals is called a supercrystal. An endcap is composed of two Dees, each of which has 3662 crystals in 138 supercrystals and 18 partial supercrystals. The crystals and supercrystals are arranged in a grid parallel to the $xy$ plane. The cross section of one crystal at the front face is $28.62 \times 28.62$ mm$^2$, and it widens to $30 \times 30$ mm$^2$ at the rear face. One crystal is 220 mm long, or 24.7 radiation lengths. The photodetectors in this region are vacuum phototriodes (VPTs). They are 25 mm in diameter, and one is attached to each crystal.

In front of each endcap is a preshower detector composed of two layers of lead radiators, alternating with silicon strip sensors. Its main purpose is to identify neutral pions. The lead layers cause pions to radiate electromagnetic showers, which are then measured by the silicon layers. The endcap preshower covers the range $1.653 < |\eta| < 2.6$. The relative positions of barrel, endcap and preshower are show in Figure 2.9.

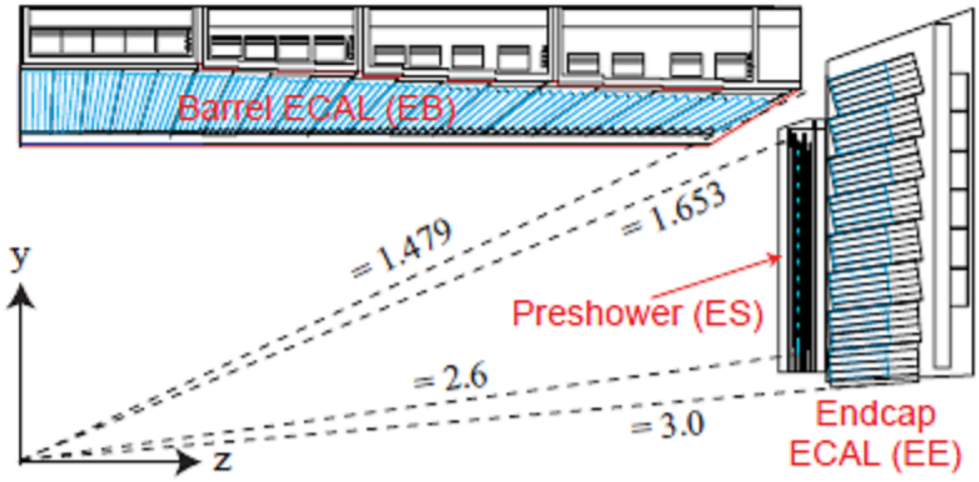


Figure 2.9: The electromagnetic calorimeter, including the barrel, endcap and preshower components, and the $\eta$ ranges they cover. Image taken from "CMS Physics Technical Design Report, Volume 1: Detector Performance and Software, Section 4.1: Description of the ECAL" [18]

The front end electronics of the ECAL amplify and shape the signal received from the photosensors. The position of the observed signal, the time of its arrival, and the amount of energy deposited are all buffered until a Level 1 Accept is received, at which point the data are transmitted to the DAQ system.

The ECAL is one component of the Level 1 trigger. Therefore, a portion of the front end electronics is designed to construct trigger primitives and transmit the ECAL decision to the central trigger system. A trigger primitive refers

to information obtained from a single tower of deposited energy. The L1 trigger considers the summed $E_T$ in the tower, and its compactness. After this information is transmitted, the accept signal returns in about 3 $\mu$s.

Before the ECAL was installed within CMS, its energy resolution was tested using an electron beam. A parameterization of the resolution is

$$\left(\frac{\sigma}{E}\right)^2 = \left(\frac{S}{\sqrt{E}}\right)^2 + \left(\frac{N}{E}\right)^2 + C^2, \tag{2.7}$$

where $S$ represents the stochastic contribution, $N$ represents the noise, and $C$ is a constant. Using the test beam, the values of these parameters were measured to be $S = 2.8\%$, $N = 0.124$ GeV, and $C = 0.30\%$. The result is a resolution of less than 0.45% for an electron with an initial energy of 120 GeV.

### 2.4.5 Hadron Calorimeter

The hadron calorimeter (HCAL) [19], with the ECAL, forms a complete calorimetry system for the measurement of jet and missing transverse energy. The HCAL surrounds the ECAL and is the outermost detector component that is housed within the magnet solenoid. It is composed of absorber plates made of brass alloy or stainless steel, alternating with plastic scintillator tiles.

The Hadron Barrel (HB) has an inner radius of 177 cm and an outer radius of 295 cm, and it covers the range $|\eta| < 1.3$. It is split into two half barrels, which are further subdivided into 18 wedges that each cover 20° in $\phi$. One wedge is composed of flat absorber plates that are parallel to the beam axis. The innermost and outermost layers are made of stainless steel, while the rest are of brass alloy. Between the absorber plates are 17 layers of active plastic scintillator

tiles. The innermost tile, which is twice the thickness of the rest, is immediately behind the ECAL. An individual tile covers a solid angle of $\Delta\eta \times \Delta\phi = 0.087 \times 0.087$.

The Hadron Endcap (HE) is tapered to overlap with the HB and to interlock with it. It covers the range $1.3 < |\eta| < 3.0$. Wedges in the endcap use only brass absorber plates, and contain 19 plastic scintillator layers. They are arranged in the same 18-fold geometry as employed in the barrel. Up to $|\eta| = 1.74$, the $\Delta\eta \times \Delta\phi$ solid angle covered by one tile is $0.087 \times 0.087$, as in the barrel. Beyond that, they become progressively wider in $\eta$ and $\phi$. The layout of the hadron calorimeter is shown in Figure 2.10.

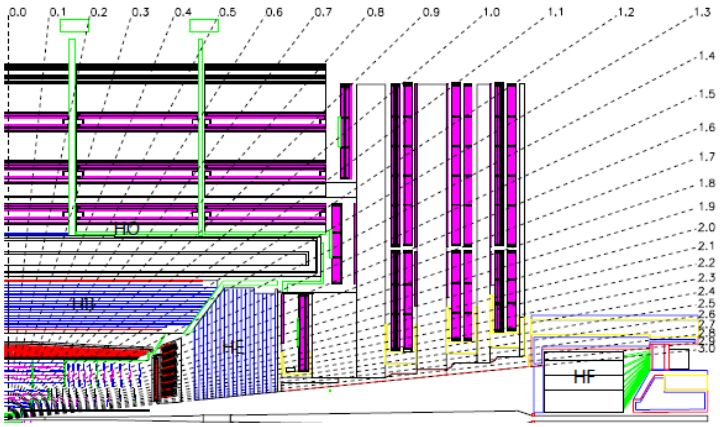


Figure 2.10: The barrel and endcap sections of the hadron calorimeter, showing the relative positions and $\eta$ ranges of the components. Image taken from "The CMS Experiment at the CERN LHC, Chapter 5: Hadron calorimeter" [19].

There are additional layers of scintillator material in the Hadron Outer (HO), which is located outside the magnet solenoid. These layers are housed in the magnet return yoke, and therefore their geometry is similar to that of the muon system. There are five rings, each of which is centered on the beamline and parallel to the $xy$ plane. A ring is divided into twelve sectors. With the exception

of the middle ring, these sectors have single layers of 10 mm thick scintillator tile at a radial distance of 4.07 m. In the middle ring, there are two such layers at 3.82 m and 4.07 m, surrounding 18 cm of an iron absorber. The HO covers the range $|\eta| < 1.3$.

Finally, the Hadron Forward (HF) section provides coverage between $3.0 < |\eta| < 5.0$. Its front face is 11.2 m from the interaction point. The absorber material in this section is stainless steel, and Cerenkov light is emitted by quartz fibers which are welded into grooves in the steel plates. Each module, one in the $+z$ direction and one in the $-z$ direction, consists of 18 wedges, with the quartz fibers arranged parallel to the beam line.

Optical signals from the barrel, outer and endcap systems are detected and converted to electric signals by multichannel hybrid photodiodes (HPDs). In the forward system, where the magnetic field is less intense, the optical signals are detected by standard photomultiplier tubes.

The HCAL is another component of the Level 1 Trigger. Like in the ECAL, a portion of the front end electronics is designed for constructing trigger primitives out of the information from individual towers. This is sent to the regional calorimeter trigger. If a Level 1 Accept is received, the front end electronics read out the rest of the hits and transmit this information to the DAQ system.

Energy resolution in the HCAL has a complex dependence on the energy and position of an incident particle. This topic will be discussed in Section 2.5.6, in the context of jet reconstruction.

### 2.4.6 Muon System

The muon detector system [20] is the outermost layer of CMS. It is located in the magnet return yokes, outside the superconducting solenoid.

The muon system is composed of three different kinds of gaseous detectors. The barrel muon detector, which covers the range $|\eta| < 1.2$, employs drift tube (DT) chambers. The endcaps, which cover up to $|\eta| < 2.4$, have cathode strip chambers (CSCs). Both the barrel and the endcap also use resistive plate chambers (RPCs). Compared to the others, RPCs have a faster response time but coarser position resolution.

The barrel is divided into five wheels, labeled YB-2, YB-1, YB0, YB+1, YB+2. The number indicates the position of the wheel along the $z$ axis. Each wheel contains 12 sectors, where a sector covers 30° of azimuthal angle $\phi$. The barrel system has 250 drift chambers in total, which are arranged in four layers, or stations. The two innermost stations, MB1 and MB2, consist of units of one DT between two RPCs. The two outermost stations, MB3 and MB4, have DTs coupled to one, two or four RPCs in a layer. In the three innermost chambers, one DT consists of 12 layers of drift tubes in four staggered superlayers of three each. In MB4, a DT has only two superlayers. Each superlayer is designed to yield a measurement of the $r - \phi$ coordinates of an incident muon, with a resolution of 100 $\mu$m.

The muon endcap contains a total of 468 CSCs. Each endcap is divided into four stations, arranged perpendicular to the beam line. A station is composed of either two or three concentric rings. A CSC is trapezoidal in shape and consists of six gas gaps arranged in overlapping layers, where each layer can return a

measurement of the $(r, \phi)$ coordinates of a muon with a resolution of 150 $\mu$m. Figure 2.11 shows the layout of the muon system, including the distributions of DTs, CSCs and RPCs within the barrel and endcap sections.

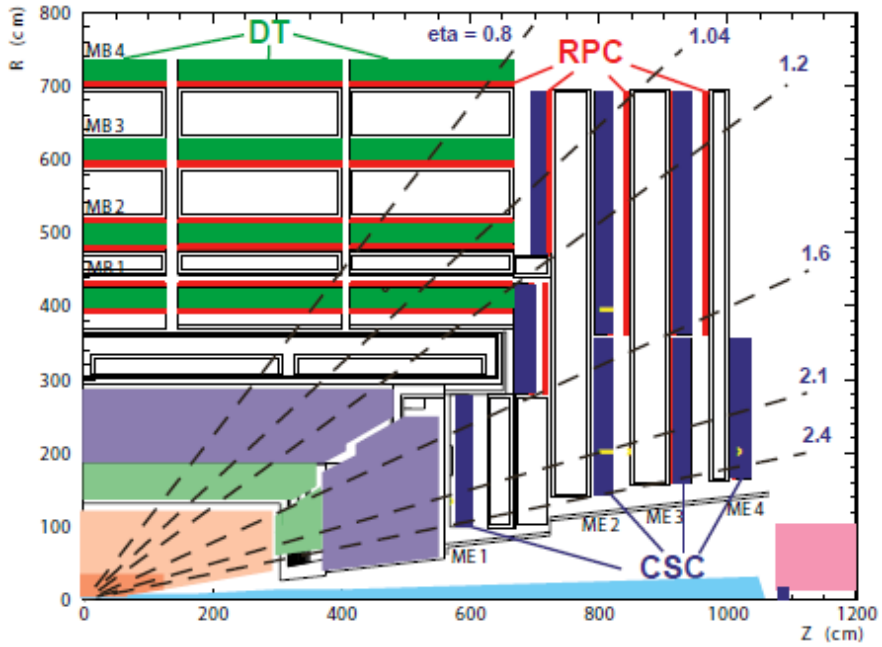


Figure 2.11: Layout of the muon barrel and endcap systems. The placements of the DTs, CSCs and RPCs within the system are indicated, as are the $\eta$ ranges covered. Image taken from "CMS Physics Technical Design Report, Volume 1: Detector Performance and Software, Section 1.5: CMS: the overall concept" [11].

The muon system is the final component to the Level 1 trigger. Each of the three types of muon detector components contribute to the L1 decision. The trigger electronics return one vector per muon per station, each of which is a trigger primitive. These are combined by the global muon trigger to construct overall muon candidates, and the results are forwarded to the global trigger.

## 2.5 Event Reconstruction with CMS Software

### 2.5.1 Structure of CMS Software

An extensive collection of C++ software packages are employed to perform detector simulation and event reconstruction [21]. This software as a whole is referred to as CMSSW, and it encompasses many different tasks. For example, as previously discussed, the HLT uses software to perform primary dataset processing. After the HLT decision has been rendered and the primary datasets have been archived, additional software is needed to perform offline reconstruction of all of the physics objects in the selected events. CMSSW is also used to perform Monte Carlo computer simulations of all steps in the data-taking process. Calibrations and data quality management are performed using software, plus additional tasks that are specific to certain subdetectors.

The framework for CMSSW is the Event Data Model (EDM). Its focus is the Event, which is accessed by the EventSetup. The Event holds all of the data taken by the detector, or simulated to have been taken. It is run through modules which add or remove information.

Monte Carlo studies of background and signal processes are used in a variety of ways in physics analysis. The feasibility of detecting a new physics signal in a particular decay channel can be studied in Monte Carlo simulations, allowing physicists to focus their attention on those channels with the greatest potential for new discoveries. Many detection studies, such as the one that will be considered in this document, depend on Monte Carlo estimates of certain Standard Model backgrounds. An accurate computer simulation of the CMS detector is

essential for all of these purposes.

Monte Carlo simulations proceed in several steps. First, one requires a physics generator such as MadGraph [22] or Pythia [23]. This step generates the desired physics process from the initial proton-proton collision, and calculates momentum vectors for the subsequent decay products of the particles that are produced. The generator software typically records this information in HepMC format [24].

The next step simulates hits in the detector. This segment of CMSSW uses the GEANT4 simulation toolkit [25] to create a highly detailed computer model of the geometry of the detector and the materials of which it is constructed. Based on the output of the generation step, the interaction of the output particles with the detector material can be modeled.

These simulated interactions become the input to the digitization step. CMSSW models the response of the detector electronics to the hits produced by the incident particles. The outputs contain the same digitized information that would be transmitted to the DAQ system from the Front End Drivers.

The final step is the reconstruction of physics objects. This process is applied to the outputs of the digitization step, whether it was performed in software as part of a Monte Carlo simulation or by the front end electronics in the course of physics running. Reconstruction proceeds in three phases: local, global, and combined. Local reconstruction collects information about the amount and position of energy deposits within a given subdetector. Global reconstruction isolates the best measurements from all of the different outputs of a given subdetector, but it does not combine information from more than one subdetector.

Finally, combined reconstruction uses all of the information from the event to create higher level physics objects such as muons, photons, electrons, jets or missing energy.

The Physics Analysis Toolkit (PAT) [26] is an extra analysis layer that is performed on the reconstructed objects. It stores all of the information from the reconstruction step in an easily accessible format, and it calculates commonly used quantities such as isolations. PAT photons, electrons, jets and $\not\!\!E_T$ are the primary software objects used in the analyses that will be detailed in this document.

### 2.5.2 Muon Reconstruction

Reconstruction of muons [27] takes place both online and offline. The muon system is part of the Level 1 Trigger, and therefore very quick online reconstructions of muons are performed for the L1 Trigger and the HLT. Later, more detailed muon reconstruction is performed offline, and the results are incorporated into the event content. Both types of reconstruction begin at the same point: with hits in individual chambers in the muon system.

The Level 1 muon identification is performed using custom electronics that are incorporated into the muon system. Different systems and trigger logics are applied to the DTs, CSCs, and RPCs. Hits in the DTs and CSCs are analyzed for patterns and processed into one vector per muon per station, which is referred to as a trigger primitive. Candidates from the RPCs are reconstructed separately based on information from all stations. Finally, the two sets of candidates are compared, and the four best muon candidates are sent to the Global Trigger.

Part of this assessment involves extrapolating the muon tracks to towers in the calorimeter.

The muon candidates from the L1 muon trigger are used to seed the reconstruction that is performed by the HLT. To save time, the HLT reconstruction takes a very local approach. Each seed candidate defines a region of interest in which more detailed reconstruction is performed. Hits outside these regions are not considered. This procedure is called Level 2 or standalone reconstruction. For offline reconstruction, in which high-speed performance is not the primary goal, a more global approach is used. This is Level 3 or global reconstruction.

In the Level 2 phase, the vectors produced during L1 reconstruction are organized from the innermost layer outward, with observed vectors in the next layer being compared to the momenta predicted by the previous layer. In this fashion, a trajectory through the muon system is reconstructed and bad hits are rejected. Another such procedure is then applied from the outermost layer of the detector and working inward, until the track parameters that yield the best fit can be defined at the innermost station. The reconstruction of the track is also influenced by whether it can be extrapolated back to the interaction point.

The HLT muon candidate is used to seed the Level 3 reconstruction, which now includes information from the tracker. The trajectory for a standalone muon is extrapolated to the outer layer of the tracker, where a region of interest within the tracker is defined. A $\chi^2$ track reconstruction algorithm is performed on the hits within this region. The potential trajectories are correlated with the muon signals in different ways in an attempt to detect bremsstrahlung or other sources of energy loss that the muon might have experienced before reaching the muon system.

There also exists a separate muon identification algorithm, which starts from the tracker and progresses outward. This procedure has the advantage of potentially identifying low-$p_T$ muons that do not reach the outer layers of the muon tracker. The initial objects are the tracks, which are then matched to energy deposits in the calorimeters and finally to hits in the muon detectors.

### 2.5.3 Electromagnetic Supercluster Reconstruction

Photons and electrons are expected to deposit most of their energy in the ECAL [28]. The difference between them is that an electron is also expected to interact with the tracker, while a photon is not. The reconstruction algorithms for these two objects begin with the patterns of energy deposits in the ECAL.

An electron or photon, when it is incident on the ECAL, will leave 94% of its energy within a $3 \times 3$ block of calorimeter crystals, and 97% of its energy within a $5 \times 5$ block. Since the particle trajectories curve in the presence of the magnetic field, the energy deposits are spread out in $\phi$. This spread is modeled by assembling a supercluster, which is a cluster of clusters that are presumed to come from the same object.

There are a variety of superclustering algorithms that are applicable to different situations. The problem of collecting all of the energy due to a single object is a complicated one due to the many possible trajectories and behaviors of electromagnetic objects. The distribution of energy from an electron is expected to be broader than that from a photon. Electrons may exhibit bremsstrahlung by emitting photons as they pass through the ECAL, and photons may convert to a pair of electrons. Each of these scenarios requires a different approach.

The Hybrid algorithm for reconstructing superclusters is suitable for reconstructing high-$p_T$ electrons and unconverted photons. It uses a fixed number of crystals in the $\eta$ direction, either 3 or 5, and attempts to gather all related crystals in the $\phi$ direction. Superclusters are composed of clusters that are grouped in $\eta$. An alternative is the Island algorithm, which starts from seed crystals that are above a certain energy threshold, and progresses alternately in the $\phi$ and $\eta$ directions to collect all related crystals into a cluster. Clusters are then grouped into superclusters using the same procedure. Both of these algorithms have to correct for a series of geometric issues, such as the degree to which the majority of the energy is centered on the total area of the shower, the nearness of the supercluster to borders or cracks, and bremsstrahlung or photon conversion due to the tracker material.

The position that is assigned to a particular cluster comes from an energy-weighted mean of crystals in the cluster. Rather than a simple average, a more accurate algorithm uses logarithms of the crystal energies. The position $x$ is given by

$$x = \frac{\sum_i x_i W_i}{\sum_i W_i}, \tag{2.8}$$

where $x_i$ is the position of the $i$th crystal and $W_i$ is its weight, defined by

$$W_i = W_0 + \log \frac{E_i}{\sum_j E_j}. \tag{2.9}$$

The position of the supercluster then becomes the energy-weighted average of the positions of the clusters.

The ECAL is another component of the L1 trigger. At Level 1, which does not distinguish between photons and electrons, there are three electromagnetic triggers: single isolated, double isolated, and double relaxed. Events pass the L1 trigger if they contain electromagnetic objects that satisfy one of these sets

of conditions. Electron and photon reconstruction proceeds from these seed objects.

The HLT is composed of three steps, which are labeled Level 2, Level 2.5 and Level 3. Like the Level 1 trigger, the Level 2 phase makes use of calorimeter information only, and does not attempt to distinguish between electrons and photons. It validates the L1 decision and applies $E_T$ and $\eta$ cutoffs to the reconstructed superclusters.

Level 2.5 includes pixel detector information to test the hypothesis that the supercluster came from an electron. If hits are not found, the electron hypothesis is rejected. Photon candidacy is retained even if pixel hits are observed, in order to allow for the possibility that the photon was emitted by an electron.

Finally, Level 3 applies isolation requirements that incorporate information from other subdetectors. A potential electron is required to be isolated in the ECAL, the HCAL and the tracker. In the ECAL or HCAL, the total energy is collected within a cone that is centered on the supercluster, and this energy is required to be below a certain threshold. In the tracker, the scalar sum of the $p_T$ values is calculated over all tracks that are within a cone around the electron candidate, excluding the track that is due to the electron candidate itself. Also, the energy of the ECAL supercluster and the momentum of the track associated with it are required to match to within a certain fraction. Electromagnetic objects that fail these requirements are rejected as electron candidates.

Offline photon and electron reconstruction proceeds from the candidate objects that are reconstructed by the HLT. More detailed energy correction algorithms are applied, and more requirements are imposed that distinguish pho-

tons from electrons. These procedures are discussed in the following sections.

### 2.5.4 Offline Photon Reconstruction

The main challenge for photon reconstruction algorithms [29] is to distinguish between photons that arose from the primary interaction and photons that are the decay products of particles such as the $\pi^0$. An important tool for rejecting the latter type of photon is the application of isolation requirements in the tracker, ECAL and HCAL.

In the tracker, the isolation variables that are considered are the sum of the $p_T$ values of track within a cone about the ECAL cluster, the number of tracks within such a cone, and the angle between the ECAL cluster and the nearest tracks. In the ECAL, the variables that can be considered include:

- the total $E_T$ from all clusters within a cone that do not belong to the candidate supercluster;
- the total $E_T$ from clusters between an inner and an outer cone around the supercluster;
- $R_9$, the fraction of the total supercluster energy that is located within a $3\times3$ array of crystals that are centered on the highest energy crystal.

In the HCAL, the isolation is assessed by calculating the sum of the $E_T$ values of HCAL towers in a cone around the candidate, and the hadronic fraction $H/E$, which is the ratio of the energy in the HCAL tower just behind the supercluster to the energy of the supercluster. In all cases, the energy due to objects other than the photon candidate is required to be beneath a certain threshold.

It is common for photons that originate from the primary interaction vertex to convert in the tracker material. Identifying such photons allows for an appropriate choice of energy reconstruction algorithm. Electrons from a converted photon are tracked back to the point where they converted. This requires its own seeding technique, followed by a track reconstruction process to determine whether two suitable candidate electrons have convergent trajectories. Photon conversion candidates are required to be opposite sign electron pairs.

Once a photon has been identified, its energy can be reconstructed using one of the superclustering algorithms described in the previous section.

### 2.5.5 Offline Electron Reconstruction

A primary electron [30] consists of a track that originates from the primary interaction vertex, and that is matched to an electromagnetic supercluster. Electrons are identified within the fiducial region of the ECAL, which is the range $|\eta| < 2.5$.

Electrons traversing the silicon tracker radiate bremsstrahlung photons. The trajectory of the electron curves in the magnetic field, which causes the energy to be spread out in $\phi$. From half to as much as 95% of the initial energy of the electron can be radiated by photons before reaching the ECAL. These secondary photons can also shower in the tracker material. Soft secondary electron-positron pairs further complicate the energy patterns. Correct reconstruction of electron energy must account for all of these factors.

As with photon reconstruction, the first step in reconstructing an electron is to assemble the supercluster. The challenge that is specific to electron recon-

struction is to collect all of the bremsstrahlung photons. Different reconstruction algorithms are selected depending on the shape of the energy distribution.

Next, the position of the supercluster is used to locate potential seeds for tracks in the pixel system. A seed consists of the two innermost track hits. The matching between supercluster and seed is based on the fact that the energy-weighted average position of the supercluster, if all of the bremsstrahlung photons are properly included, corresponds to the actual position of a non-radiating electron of the same initial momentum.

Once a seed has been identified, the next step is to reconstruct the track. Algorithms are required that are specific to electron reconstruction, because the electron experiences non-Gaussian energy losses due to bremsstrahlung photons. The algorithm in use is a Gaussian Sum Filter (GSF) process.

The reconstructed track and the supercluster are now judged on several different criteria:

- Energy-momentum agreement between the supercluster and the track. The ratio of these values is required to be $E_{sc}/p_{in} < 3$.
- Agreement between the $\eta$ coordinates of the supercluster and the track, where the track is extrapolated to the point that is closest to the supercluster. These values are required to satisfy $|\Delta\eta_{in}| < 0.1$.
- Agreement between the $\phi$ coordinates of the supercluster and the track under the same conditions. This is required to be $|\Delta\phi_{in}| < 0.1$.
- Ratio of hadronic energy to electromagnetic energy. The energy in the HCAL tower that is just behind the electromagnetic seed cluster is compared to the energy of that seed cluster, and must satisfy $H/E < 0.2$.

Objects that fail these cluster shape and track matching criteria are removed from consideration as electron candidates.

Electron isolation, particularly track isolation, is an effective means of rejecting electron candidates that originated from jets, rather than true electrons. The track isolation is defined to be the sum of the $p_T$ values of all tracks within a cone about the electron candidate, except for the electron track. Similarly, the ECAL and HCAL isolations are defined by summing the ECAL or HCAL energy deposits within a cone about the electron, excepting those associated with the electron. The relative isolation is calculated by dividing the absolute isolation by the electron $p_T$.

Other quantities that are used to identify electrons are the shower shape covariances $\sigma_{i\eta i\eta}$ and $\sigma_{i\phi i\phi}$. These are weighted covariances of the distributions of ECAL energy crystals in the $\eta$ and $\phi$ directions. Electron candidates are rejected if the covariances are too large.

During electron reconstruction, relatively loose restrictions are placed on all of the above variables. This has the effect of preserving as many electron candidates as possible. However, jets may also satisfy all of the identification requirements, and therefore they will be erroneously reconstructed as electrons. The phenomenon of fake electrons will be addressed in detail later in this document.

### 2.5.6 Jet Reconstruction

QCD events with high-$p_T$ jets have very large cross sections at the LHC, and so a considerable portion of the CMS detector is devoted to jet reconstruction [31]. Accurate measurements of jet energies and momenta are necessary in order to reliably assess the missing transverse energy, $\not{E}_T$, in an event.

The initial objects used in jet reconstruction are calorimeter towers, which consist of hits in both the ECAL and the HCAL. Since the granularity in the ECAL is finer than that in the HCAL, the energy in all of the ECAL crystals that correspond to an individual HCAL segment are summed. This collection constitutes a tower.

A variety of jet reconstruction algorithms are in use at CMS. There are jet-based triggers which employ a quick and relatively simple process, the iterative cone algorithm. For offline reconstruction, the jets that will be used in this document are reconstructed by the anti-$k_T$ algorithm [32].

In addition to the reconstruction algorithm, which selects the input objects that are assigned to a given jet, the reconstruction procedure also depends on the means by which the energies and momenta of the inputs are combined. The two options are the energy scheme, in which the components are added as four vectors, and the result is a massive jet; or the $E_T$scheme, where the $E_T$ values of the components are summed as scalars, and the result is a massless jet. In the latter scheme, the direction is chosen by either $\sin\theta = \sum E_T/E$ for cone algorithms or $\eta = \sum E_{Ti}\eta_i/\sum E_T$ and $\phi = \sum E_{Ti}\phi_i/\sum E_T$ for $k_T$ algorithms.

First, consider the iterative cone algorithm. The starting point is a list of input particles and calorimeter towers that have been ordered by $E_T$. A cone of

radius $R$ in $(\eta, \phi)$ space is fixed around the first entry on the list, assuming that its $E_T$ is above a certain threshold. The objects inside the cone are used to calculate a preliminary jet direction and energy using the $E_T$ scheme. This intermediate object is referred to as a proto-jet. The resulting direction becomes a new seed, and the iteration is repeated until the change between steps is $< 1\%$ in energy and $< 0.01$ in $\Delta R$. All of the input objects that contribute to the final step are then removed from the master list, and the sequence is repeated with the next object on the list that is above the minimal threshold. The process is complete when no more seeds above the threshold remain on the master list

A variant of this is the midpoint cone algorithm. The difference is that objects are not removed from the master list after each proto-jet is created. Therefore, by the end of the iterations, one input object might belong to multiple proto-jets. For any two proto-jets that are closer together than the cone diameter, their midpoint is used to seed another proto-jet. If the proto-jet of the highest $p_T$ does not share any objects with other proto-jets, then it becomes a jet and is removed from the list of proto-jets. Otherwise, the amount of energy shared with the neighbor of next-highest $E_T$ is compared to the total energy of the proto-jet. If the fraction is above a certain threshold, then the proto-jets are merged. Otherwise, each shared object is assigned to the closer of the two seeds. This splitting and merging process is repeated, beginning with the proto-jet of next highest $E_T$, until no more remain.

The anti-$k_T$ algorithm is one instance of a class of algorithms that can be described as follows. As before, the starting point is a list of particles and calorimeter cells that are the input objects. Let them be indexed by $i$. For each object $i$

and each pair $(i, j)$, define the following quantities:

$$d_i = (k_{Ti})^{2p} R^2, \tag{2.10}$$

$$d_{ij} = \min\left\{k_{Ti}^{2p}, k_{Tj}^{2p}\right\} R_{ij}^2. \tag{2.11}$$

In the above expressions, $k_{Ti}$ is the transverse momentum of the $i$th object, and $R_{ij}^2 = \left(\eta_i - \eta_j\right)^2 + \left(\phi_i - \phi_j\right)^2$. The quantity $R^2$ is usually set to unity, and $p$ parametrizes the class of algorithms. The case $p = 1$ is called the inclusive $k_T$ algorithm, while the case $p = -1$ is the anti-$k_T$ algorithm. In all cases, the algorithm proceeds as follows. The smallest value is selected out of all of the $d_i$ and $d_{ij}$ values. If it is of the type $d_{ij}$, then objects $i$ and $j$ are removed from the list, merged, and added as a new combined object. If the minimum value is of the type $d_i$, then object $i$ is designated a jet. This procedure repeats until only jets remain.

When $p = 1$, the effect of the algorithm is to merge objects that have $R_{ij} < R$, and therefore the resulting jets all have $R_{ij} > R$. When $p = -1$, the behavior is less straightforward, but it still leads to reasonable jet definitions. In this case, the value of $d_{ij}$ is dominated by the higher-$k_T$ jet, and so soft jets will tend to be collected by the hard jets in their vicinity before they cluster among themselves. If two jets of roughly the same $k_T$ are within $2R$ of each other, they will be conical except for a boundary between them.

It is a complex procedure to determine the precise relationship between the response of the calorimetry system and the original energy of the hadrons that constitute the jet. The summed energy in the calorimetry towers may not accurately represent the true hadron energy. Therefore, after the jets have been reconstructed, corrections are applied that attempt to compensate for the many factors that can influence the absolute jet energy scale. In data, a major source

of systematic uncertainty is the uncertainty in jet energy.

The CMS default is the combination of corrections that are referred to as L2 and L3 [33]. The goal of the L2 corrections is to flatten the jet response with respect to $\eta$. A jet at an arbitrary $\eta$ value is assigned a correction relative to jets from the central region, $|\eta| < 1.3$. The L3 corrections are absolute corrections aimed at the overall jet energy scale. Their goal is to flatten the jet response with respect to $p_T$. Both sets of corrections can be obtained either from Monte Carlo studies or using data-driven methods. After they have been applied, the uncertainty in jet energy scale for jets measured in data is estimated to be 10% [34].

In Monte Carlo simulations, the jet energy resolution can be studied by comparing the reconstructed jet transverse energy, $E_T^{rec}$, to the simulated energy of the original parton, $E_T^{MC}$. The width of the distribution of $E_T^{rec}/E_T^{MC}$ can be parametrized by

$$\sigma\left(\frac{E_T^{rec}}{E_T^{MC}}\right) = \left(\frac{a}{E_T^{MC}} \oplus \frac{b}{\sqrt{E_T^{MC}}} \oplus c\right)\left\langle\frac{E_T^{rec}}{E_T^{MC}}\right\rangle, \tag{2.12}$$

where $a$ is attributed to energy fluctuations due to noise, pile-up, and the underlying event energy; $b$ is attributed to the stochastic response of calorimeter measurements; and $c$ is attributed to any other non-uniformities and non-linearities. In an early Monte Carlo simulation, the values of the parameters were found to be $a = 5.6$, $b = 1.25$, $c = 0.033$ [35]. These values will be used as estimates of the uncertainty in jet transverse energy in the Monte Carlo study performed in Chapter 4.

### 2.5.7 Missing Transverse Energy Reconstruction

The missing transverse energy [36] in an event is calculated by taking the negative of the sum of the transverse energy contributions from all individual calorimeter towers. The calorimetry coverage is as complete as possible to facilitate the measurement of missing energy.

There are many issues that affect missing energy measurements. As discussed above, there is an uncertainty associated with the measured jet energies, which is propagated to the measured $\not\!\!E_T$ value. The ECAL is calibrated using photons, and therefore its response to charged pions might not be optimized. Particles that are emitted sufficiently close to the beamline are invariably going to be missed. One way to parametrize the impact of these factors is to measure the $\not\!\!E_T$ on a collection of events that in principle should have no missing energy. A distribution of $\not\!\!E_T$ values will be observed. The width of this distribution represents the resolution of the $\not\!\!E_T$ measurement.

There are two sources of corrections that apply to the $\not\!\!E_T$ value. First, the energy corrections that are applied to jets must also be applied to the $\not\!\!E_T$ calculation. These are seen to improve the missing energy resolution in some cases. Second, the energy of a non-isolated muon may not be accurately reconstructed in the detector, so a correction to its energy is applied based on a median value obtained from Monte Carlo simulations. The muon corrections are calculated as a function of muon $p_T$ and $\eta$.

In the same set of Monte Carlo simulations that yielded Equation 2.12, a parameterization of the $\not\!\!E_T$ resolution after corrections was found to be

$$\sigma^2 = (3.8\ \text{GeV})^2 + \left(0.97\ \text{GeV}^{1/2}\right)^2 \not\!\!E_T + (0.012\not\!\!E_T)^2 \,. \tag{2.13}$$

This expression will be used in Chapter 4 to estimate the uncertainty on $\not\!\!E_T$ measurements.

Evidence from previous experiments suggests that the $\not\!\!E_T$ resolution will be worse in data than in simulations. This effect is twofold. Centrally, the $\not\!\!E_T$ distribution is expected to follow a Gaussian distribution, whose width in data will be greater than simulations predict. Also, the distribution is observed to have a long non-Gaussian tail, which contains events in which there were large errors in the missing energy measurement. This tail will be thicker in data; that is, large errors will occur more frequently than predicted by simulations. Any $\not\!\!E_T$ distribution measured from Monte Carlo simulations will have systematic uncertainties due to these effects when it is compared to data.

CHAPTER 3

# PHYSICS BEYOND THE STANDARD MODEL

The CMS detector was constructed for the purpose of observing new physics processes at energies on the order of 1 TeV. There are theoretical and experimental reasons to expect physics beyond the Standard Model to manifest at this energy scale.

This chapter presents a review of the structure of the Standard Model, and some of the evidence for believing that it is not a complete model of particle physics. Two models are described that could extend the Standard Model and resolve its inconsistencies: Supersymmetry, and the Littlest Higgs model with T-Parity. The experimental signatures of these models are shown to share many features in common, in spite of being based on very different theoretical foundations.

## 3.1 Review of the Standard Model

The Glashow-Weinberg-Salam (GWS) theory provides a unified description of the weak and electromagnetic forces. It employs the Higgs mechanism to generate mass terms for the W and Z gauge bosons while leaving the photon massless. The vacuum expectation value (VEV) of the Higgs boson is used to generate mass terms for fermions. In this section, the structure of the GWS theory is reviewed, with emphasis on the role of the Higgs boson. The discussion follows that in Chapter 20 of *An Introduction to Quantum Field Theory* by Peskin and Schroder [37].

Electroweak interactions are modeled by a theory that has an SU(2) $\times$ U(1)

symmetry. To incorporate the Higgs mechanism, a scalar field $\phi$ is introduced in the spinor representation of SU(2) with a charge of +1/2 under U(1). Then the overall gauge transformation of $\phi$ is

$$\phi \rightarrow e^{i\alpha^a \sigma^a/2} e^{i\beta/2} \phi, \tag{3.1}$$

where $\sigma^a$ are the Pauli matrices, $a = 1, 2, 3$.

Assume that $\phi$ obtains a vacuum expectation value, $\langle\phi\rangle$. Apply an SU(2) rotation so that the VEV takes the form

$$\langle\phi\rangle = \frac{1}{\sqrt{2}} \begin{pmatrix} 0 \\ v \end{pmatrix}. \tag{3.2}$$

Using this form of $\langle\phi\rangle$, the combination of generators given by $\alpha^1 = \alpha^2 = 0$ and $\alpha^3 = \beta$ leaves $\langle\phi\rangle$ invariant. Since there is one unbroken combination of generators, the corresponding combination of gauge bosons remains massless, while the other three acquire masses.

The kinetic term for $\phi$ is $\left|D_\mu \phi\right|^2$, where $D_\mu$ is the covariant derivative associated with the SU(2) × U(1) symmetry group. $D_\mu$ acts on $\phi$ by

$$D_\mu \phi = \left(\partial_\mu - igA_\mu^a \sigma^a/2 - \frac{i}{2} g' B_\mu\right) \phi. \tag{3.3}$$

In this expression, the gauge bosons associated with the SU(2) group are denoted $A_\mu^a$, and the coupling constant is $g$. The gauge boson associated with the U(1) group is $B_\mu$, and the coupling constant is $g'$.

After spontaneous electroweak symmetry breaking (EWSB) occurs, the scalar field $\phi$ can be redefined to take the form $\langle\phi\rangle + \phi$. Mass terms for $A_\mu^a$ and $B_\mu$ arise upon expanding the kinetic term with this new definition. These mass terms are

$$\frac{1}{2}\frac{v^2}{4}\left[g^2\left(A_\mu^1\right)^2 + g^2\left(A_\mu^2\right)^2 + \left(-gA_\mu^3 + g' B_\mu\right)^2\right]. \tag{3.4}$$

Define the usual electroweak gauge bosons by

$$W_\mu^\pm = \frac{1}{\sqrt{2}}\left(A_\mu^1 \mp iA_\mu^2\right), \tag{3.5}$$

$$Z_\mu^0 = \frac{1}{\sqrt{g^2+g'^2}}\left(gA_\mu^3 - g'B_\mu\right). \tag{3.6}$$

When Equation 3.4 is rewritten with these substitutions, expressions for the gauge boson masses can be found:

$$m_W = \frac{gv}{2}, \tag{3.7}$$

$$m_Z = \sqrt{g^2+g'^2}\frac{v}{2}. \tag{3.8}$$

The orthogonal combination

$$A_\mu = \frac{1}{\sqrt{g^2+g'^2}}\left(g'A_\mu^3 + gB_\mu\right) \tag{3.9}$$

is massless.

For any arbitrary state in a general SU(2) representation with generators $T^a$ and with U(1) charge $Y$, the covariant derivative can be written in terms of the W and Z bosons as

$$D_\mu = \partial_\mu - i\frac{g}{\sqrt{2}}\left(W_\mu^+T^+ + W_\mu^-T^-\right) - i\frac{1}{\sqrt{g^2+g'^2}}Z_\mu\left(g^2T^3 - g'^2Y\right) - i\frac{gg'}{\sqrt{g^2+g'^2}}A_\mu\left(T^3+Y\right), \tag{3.10}$$

where $T^\pm = \left(T^1 \pm iT^2\right)$. In the final term, the coefficient of the electromagnetic interaction is identified with the electron charge, $e$:

$$e = \frac{gg'}{\sqrt{g^2+g'^2}}. \tag{3.11}$$

The quantum number for electric charge, $Q$, is given by the combination of generators in this term: $Q = T^3 + Y$.

The change of basis from $\left(A^3, B\right)$ to $\left(Z^0, A\right)$ can be described by the weak mixing angle, $\theta_W$, which is defined such that

$$\begin{pmatrix} Z^0 \\ A \end{pmatrix} = \begin{pmatrix} \cos\theta_W & -\sin\theta_W \\ \sin\theta_W & \cos\theta_W \end{pmatrix} \begin{pmatrix} A^3 \\ B \end{pmatrix}, \tag{3.12}$$

This implies the relations

$$\cos\theta_W = \frac{g}{\sqrt{g^2 + g'^2}}, \tag{3.13}$$

$$\sin\theta_W = \frac{g'}{\sqrt{g^2 + g'^2}}, \tag{3.14}$$

$$g = \frac{e}{\sin\theta_W}. \tag{3.15}$$

In terms of $\theta_W$ and $g$, the covariant derivative becomes

$$D_\mu = \partial_\mu - i\frac{g}{\sqrt{2}}\left(W_\mu^+ T^+ + W_\mu^- T^-\right) - i\frac{g}{\cos\theta_W} Z_\mu \left(T^3 - \sin^2\theta_W Q\right) - ieA_\mu Q, \tag{3.16}$$

In addition, the W and Z masses are related by

$$m_W = m_Z \cos\theta_W. \tag{3.17}$$

This reduces the model of electroweak interactions to three independent parameters: $e$, $\theta_W$ and $m_W$.

In the fermion sector, the $W$ boson only couples to left-handed helicity states of quarks and leptons. If $\psi_L$ and $\psi_R$ are left-handed and right-handed Weyl spinors, then they are assigned to different representations: $\psi_L$ is an SU(2) doublet and $\psi_R$ is an SU(2) singlet. The forms of the generators $T^3$ and $Y$ determine the charge $Q$.

For right-handed particles, since the state is an SU(2) singlet, $T^3 = 0$ and therefore the charge is simply $Q = Y$. The assigned values for the Standard Model fermions are $Y = +2/3$ for up quarks, $u_R$; $Y = -1$ for electrons, $e_R$; and $Y = -1/3$ for down quarks, $d_R$.

The left-handed particles of the Standard Model are contained within SU(2) doublets:

$$E_L = \begin{pmatrix} \nu_{eL} \\ e_L^- \end{pmatrix}, \quad Q_L = \begin{pmatrix} u_L \\ d_L \end{pmatrix}. \tag{3.18}$$

Using $T^3 = \frac{1}{2}\sigma^3$, the correct charge assignments arise upon setting $Y = -1/2$ for $E_L$ and $Y = +1/6$ for $Q_L$.

Note that mass terms of the form $m(\bar{e}_L e_R + \bar{e}_R e_L)$ are forbidden because $e_L$ and $e_R$ are objects from different representations. Instead, fermion masses arise from interaction terms between fermions and the Higgs field, $\phi$. For example, the Higgs field couples left-handed and right-handed electrons through the Lagrangian term

$$\Delta\mathcal{L}_e = -\lambda_e \bar{E}_L \cdot \phi e_R + \text{h.c.} \tag{3.19}$$

This term is allowed because the SU(2) indices of $E_L$ and $\phi$ are contracted, and the overall U(1) charge $Y$ is zero. Now, replace $\phi$ by its VEV to obtain

$$\Delta\mathcal{L}_e = \frac{1}{\sqrt{2}}\lambda_e v \bar{e}_L e_R + \text{h.c.} + \ldots \tag{3.20}$$

Thus, the mass of the electron is

$$m_e = \frac{1}{\sqrt{2}}\lambda_e v, \tag{3.21}$$

which depends on the vacuum expectation value of $\phi$, and on a new parameter $\lambda_e$. A neutrino mass term could be introduced a similar way, but experimental evidence suggests that a neutrino mass, if it exists at all, is extremely small. A convenient way to forbid a neutrino mass term is to assume that right-handed neutrinos, $\nu_{eR}$, do not exist.

The allowed Lagrangian terms that couple $\phi$ to the quark singlets and doublets are

$$\Delta\mathcal{L}_q = -\lambda_d \bar{Q}_L \cdot \phi d_R - \lambda_u \epsilon^{ab} \bar{Q}_{La} \phi_b^\dagger u_R + \text{h.c.} \tag{3.22}$$

Here, $\epsilon^{ab}$ is a completely antisymmetric tensor with $\epsilon^{12} = 1$. By the same process as before, replacing $\phi$ with $\langle\phi\rangle$ leads to quark masses,

$$m_d = \frac{1}{\sqrt{2}}\lambda_d v, \tag{3.23}$$

$$m_u = \frac{1}{\sqrt{2}}\lambda_u v. \tag{3.24}$$

All of the fermion masses obtained in this manner depend on $v$. The observed differences in masses observed between electrons, down quarks and up quarks are parameterized by the coefficients $\lambda_e$, $\lambda_d$ and $\lambda_u$.

With multiple generations of quarks, it is always possible to transform into a basis that diagonalizes the Higgs couplings. The consequence is to introduce weak interactions that couple the different generations. Multiple lepton generations do not observe such mixing due to the absence of the $\nu_R$ states. Individual lepton generation numbers are conserved.

Suppose the Lagrangian terms for $\phi$ take the form

$$\Delta\mathcal{L} = \left|D_\mu\phi\right|^2 + \mu^2\phi^\dagger\phi - \lambda\left(\phi^\dagger\phi\right)^2, \tag{3.25}$$

which is the most general expression that is also renormalizable. Then the potential energy minimum is

$$v = \frac{\mu}{\sqrt{\lambda}}. \tag{3.26}$$

As an explicit implementation of the Higgs field, suppose $\phi$ takes the form

$$\phi(x) = U(x)\frac{1}{\sqrt{2}}\begin{pmatrix} 0 \\ v + h(x) \end{pmatrix}, \tag{3.27}$$

where $h(x)$ is a real-valued field and $U(x)$ is a general SU(2) transformation. Since the SU(2) symmetry is local, a gauge transformation can be applied to

eliminate $U(x)$, which reduces $\phi$ to the form

$$\phi(x) = \frac{1}{\sqrt{2}} \begin{pmatrix} 0 \\ v + h(x) \end{pmatrix}. \tag{3.28}$$

This choice is called the unitary gauge.

Upon substitution, the potential energy Lagrangian terms become

$$\Delta\mathcal{L} = -\mu^2 h^2 - \lambda v h^3 - \frac{1}{4}\lambda h^4. \tag{3.29}$$

Thus, the physical particle is $h$, which is called the Higgs boson. Its mass is

$$m_h = \sqrt{2}\mu = \sqrt{2\lambda}v. \tag{3.30}$$

As with the other masses in the theory, the size of $m_h$ depends on the vacuum expectation value $v$, and on a new parameter $\lambda$.

## 3.2 Motivation for Physics Beyond the Standard Model

The complete Standard Model consists of the symmetry group SU(3) × SU(2) × U(1), where the SU(3) term describes the strong interactions amongst quarks. In analogy with the spontaneous symmetry breaking of the electroweak theory, theories have been put forth in which the Standard Model is embedded within a larger symmetry group that is spontaneously broken. Such a model is referred to as a Grand Unified Theory (GUT).

Associated with the symmetry group of a GUT is a single gauge coupling. To determine the approximate energy at which symmetry breaking must occur, the energy dependences of the SU(3), SU(2) and U(1) Standard Model coupling constants can be extrapolated until they become approximately equal. This extrap-

olation procedure suggests that grand unification becomes feasible at energies above roughly $10^{15}$ GeV [38, 39, 40].

Another feature of very high energy theories is the significance of the gravitational force. The characteristic energy scale of gravitational interactions can be parameterized by the Planck mass,

$$M_{Pl} = \frac{1}{\sqrt{G_N}} \approx 1.2 \times 10^{19} \text{ GeV}, \tag{3.31}$$

where $G_N$ is the Newtonian gravitational constant. Thus, the grand unification scale is also approaching the energy regime at which a model of particle interactions must include the force of gravity.

These very large energy scales have an impact on the sector of the Standard Model pertaining to the Higgs boson. When evaluating one-loop quantum corrections to the Higgs boson mass parameter $\mu$, one obtains terms that are quadratically divergent [41, 42]. An example of such a diagram involving a fermion loop is shown in Figure 3.1. If divergences are avoided by imposing an ultraviolet cutoff value $\Lambda$, then the one-loop corrections to $\mu^2$ are on the order of $\Lambda^2$.

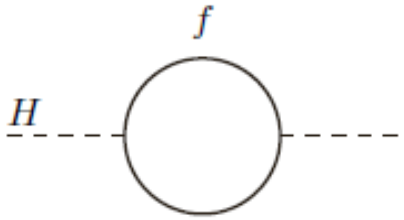


Figure 3.1: Quadratically divergent one-loop correction to the Higgs mass parameter arising from the coupling between the Higgs and a fermion, $f$.

The vacuum expectation value of the Higgs scalar must be of an appropriate size to generate the observed W and Z boson masses. Recalling that $m_h = \sqrt{2}\mu =$

$\sqrt{2\lambda}v$, and assuming that the dimensionless parameter $\lambda$ is of order unity, this implies that $\mu^2 \sim (100\,\mathrm{GeV})^2$. By contrast, if the ultraviolet cutoff is taken to be the grand unification scale, then the one-loop corrections to this value are $\delta\mu^2 \sim \left(10^{15}\,\mathrm{GeV}\right)^2$. The observable value of $\mu^2$ could only arise if the bare mass parameter $\mu_0^2$ cancels the one-loop corrections with exceptional precision. This phenomenon is called fine-tuning, and should be avoided in a viable theory.

Thus, either the Higgs mass is protected from one-loop corrections through some additional mechanism or symmetry, or the ultraviolet cutoff scale must be no more than $\Lambda \sim 1$ TeV. In any case, manifestations of physics processes beyond the Standard Model should be visible at the energy scales accessible by the LHC.

Another piece of evidence for new physics comes from astronomical observations. The rotation curves of galaxies suggest that they are composed of more mass than can be accounted for by their luminous objects [43]. Measurements of the cosmic microwave background such as those performed by the Wilkinson Microwave Anisotropy Probe (WMAP) can be fit very well by a model that includes a non-hadronic matter density [44]. This source of mass is termed Dark Matter. It must be stable, charge neutral, and weakly interacting, and it does not belong to the set of particles described by the Standard Model. Many candidate theories for physics beyond the Standard Model contain a Dark Matter candidate.

The following sections describe two candidate theories for physics beyond the Standard Model: Supersymmetry, and the Littlest Higgs model with T-Parity. Using different theoretical approaches, both of these theories address the issue of quadratically divergent Higgs mass corrections, and they both con-

tain a weakly interacting neutral particle that could account for Dark Matter.

## 3.3 Supersymmetry

One of the motivations for the development of the theory of supersymmetry comes from the quadratic divergences in one-loop corrections to the Higgs mass. To avoid fine-tuning, naturalness dictates that the ultraviolet cutoff scale for these quadratic divergences must be on the order of 1 TeV.

Supersymmetry posits that quadratic divergences due to fermions can be counterbalanced by additional loop corrections due to new scalars. Likewise, quadratic divergences due to vector bosons are counterbalanced by terms due to new fermions. The new particles are introduced in such a way that the Higgs is exactly massless to all orders if the theory is exactly supersymmetric; that is, if masses and couplings are equal and there are no symmetry breaking terms.

Supersymmetry cannot be an exact symmetry in nature. The means by which supersymmetry is broken controls the final mass of the Higgs, and of the supersymmetric partner particles. The Minimal Supersymmetric Standard Model (MSSM) is an extension of the Standard Model in which supersymmetry is broken explicitly. The MSSM introduces 105 new parameters beyond those in the Standard Model, affording a wide range of possible phenomenological behaviors. A particular set of assumptions that constitute the theory of minimal Supergravity (mSUGRA) reduces the number of new parameters to five. The MSSM and mSUGRA implementations of supersymmetry are outlined in the following sections. The discussion is based primarily on the treatment of supersymmetry in *Theory and Phenomenology of Sparticles* by M. Drees, R. Godbole and

P. Roy [45].

### 3.3.1 Grassmann Variables

Supersymmetric theories are constructed within a space that includes the usual four spacetime coordinates, plus a pair of conjugate Grassmann spinor coordinates [46]. The basic property of Grassmann variables is that they anticommute.

First, postulate the existence of a finite number $n$ of Grassmann elements: $\epsilon_1, \ldots, \epsilon_n$. These objects satisfy the anticommutation relation

$$\epsilon_i \epsilon_j = -\epsilon_j \epsilon_i, \tag{3.32}$$

which implies that $\epsilon_i^2 = 0$. Grassmann elements are assumed to commute with ordinary complex numbers. A Grassmann variable can then range over these Grassmann elements. Define conjugate Grassmann variables $\theta$ and $\bar{\theta}$ by asserting that they satisfy the following properties:

$$\theta\bar{\theta} + \bar{\theta}\theta = 0, \tag{3.33}$$

$$\theta^2 = \bar{\theta}^2 = 0, \tag{3.34}$$

$$\bar{\bar{\theta}} = \theta. \tag{3.35}$$

These variables generate the Grassmann algebra.

A function of $\theta$ takes the general form

$$f(\theta) = f_0 + f_1\theta, \tag{3.36}$$

where $f_0$ and $f_1$ are complex numbers. These functions form a two-dimensional space. The conjugate functions

$$\bar{f}(\bar{\theta}) = \bar{f}_0 + \bar{f}_1\bar{\theta} \tag{3.37}$$

form a second two-dimensional space. A function of both variables takes the form

$$f(\theta, \bar{\theta}) = f_0 + f_1\theta + \bar{f}_2\bar{\theta} + f_3\theta\bar{\theta}, \tag{3.38}$$

and is an element of the Grassmann algebra.

### 3.3.2 A Supersymmetry Algebra

The Standard Model is constructed in four-dimensional Minkowski spacetime with the metric

$$g_{\mu\nu} = g^{\mu\nu} = \text{diag}\,(1, -1, -1, -1)\,. \tag{3.39}$$

The Poincaré group is a continuous spacetime symmetry that consists of translations, rotations and Lorentz boosts. The latter two by themselves constitute the Lorentz group, which encompasses those transformations that keep the origin constant and that preserve the lengths of four-vectors. An infinitesimal inhomogeneous Lorentz transformation has the form

$$x'^{\mu} = (\delta^{\mu}_{\nu} + \omega^{\mu}_{\nu})\, x^{\nu} + a^{\mu}, \tag{3.40}$$

where $\omega_{\mu\nu}$ is a second rank antisymmetric constant tensor and $a^{\mu}$ is a constant four vector. The associated unitary operators are

$$U(a) = e^{ia^{\mu}P_{\mu}} \tag{3.41}$$

for translations and

$$U(\Lambda) = e^{-i\omega^{\mu\nu}M_{\mu\nu}/2} \tag{3.42}$$

for homogeneous Lorentz transformations. The Hermitian generators $P_{\mu}$ and $M_{\mu\nu}$ satisfy the commutation relations

$$\left[P_{\mu}, P_{\nu}\right] = 0, \tag{3.43}$$

$$\left[M_{\mu\nu}, P_\rho\right] = i\left(g_{\nu\sigma}P_\mu - g_{\mu\rho}P_\nu\right), \tag{3.44}$$

$$\left[M_{\mu\nu}, M_{\rho\sigma}\right] = -i\left(g_{\mu\rho}M_{\nu\sigma} - g_{\mu\sigma}M_{\nu\rho} - g_{\nu\rho}M_{\mu\sigma} + g_{\nu\sigma}M_{\mu\rho}\right). \tag{3.45}$$

These relations constitute the Poincaré algebra [47], while the last line alone constitutes the Lorentz algebra.

A representation of the Poincaré group can be constructed from the $4 \times 4$ $\gamma^\mu$ matrices. In the Weyl representation, these matrices can be written

$$\gamma^0 = \begin{pmatrix} 0 & 1 \\ 1 & 0 \end{pmatrix}, \tag{3.46}$$

$$\gamma^i = \begin{pmatrix} 0 & \sigma^i \\ -\sigma^i & 0 \end{pmatrix}. \tag{3.47}$$

Then one can verify that the definitions

$$\Sigma_{\mu\nu} = \frac{i}{4}\left[\gamma_\mu, \gamma_\nu\right], \tag{3.48}$$

$$M_{\mu\nu} = -x_\mu P_\nu + x_\nu P_\mu + \Sigma_{\mu\nu} \tag{3.49}$$

satisfy the Poincaré algebra. This allows the identification of $P_\mu$ as the momentum operator. If $i$ and $j$ are taken to range over spatial indices only, then $M_{ij}$ is the total angular momentum tensor, and $\Sigma_{ij}$ represents the contribution due to spin. The generators $M_{0k}$ generate Lorentz boosts.

The goal is to expand the Poincaré algebra to include a new generator that represents supersymmetry. However, a result called the Coleman-Mandula theorem [48] presents an obstacle to doing so. This theorem considers a nontrivial Lie algebra associated with all of the continuous symmetries of a physical system under certain basic assumptions. It states that if such a Lie algebra contains both the Poincaré algebra and another Lie algebra as subalgebras, where the

second algebra is defined by a set of generators $\{T^a\}$ and structure constants $t_c^{ab}$, i.e.

$$\left[T^a, T^b\right] = it_c^{ab}T^c, \tag{3.50}$$

then the relationship between the two sets of generators must be

$$\left[T^a, P_\mu\right] = \left[T^a, M_{\mu\nu}\right] = 0. \tag{3.51}$$

In other words, the Lie algebra associated with any other symmetry group can only interact with the Poincaré algebra in a trivial way.

In order to introduce supersymmetry as a nontrivial spacetime symmetry, a graded Lie algebra structure is required [49]. Specifically, supersymmetry is implemented using a $Z_2$-graded structure that includes bosonic generators, which are identified as even, and fermionic generators, which are identified as odd. These types of generators satisfy the commutation and anticommutation relations

$$\begin{aligned} [\text{even}, \text{even}] &= \text{even}, \\ [\text{even}, \text{odd}] &= \text{odd}, \\ \{\text{odd}, \text{odd}\} &= \text{even}. \end{aligned} \tag{3.52}$$

In addition to $P_\mu$ and $M_{\mu\nu}$, the supercharge $Q_a$ can now be introduced. $Q_a$ is the spinorial fermionic generator of supersymmetry transformations. Henceforth, $a$ will represent a spinor index.

Using the definitions

$$J_i = \frac{1}{2}\epsilon_{ijk}M_{jk}, \tag{3.53}$$

$$K_i = -M_{0i}, \tag{3.54}$$

$$\mathcal{J}_i^{\pm} = \frac{1}{2}\left(J_i \pm iK_i\right), \tag{3.55}$$

where $J_i$ is the angular momentum operator, one can show that the homogeneous Lorentz group is homomorphic to the group $\mathrm{SU}(2)_+ \otimes \mathrm{SU}(2)_-$. Specifically,

this result holds because $\mathcal{J}_j^{\pm}$ satisfy

$$\left[\mathcal{J}_i^+, \mathcal{J}_j^+\right] = i\epsilon_{ijk}\mathcal{J}_k^+, \tag{3.56}$$

$$\left[\mathcal{J}_i^-, \mathcal{J}_j^-\right] = i\epsilon_{ijk}\mathcal{J}_k^-, \tag{3.57}$$

$$\left[\mathcal{J}_i^+, \mathcal{J}_j^-\right] = 0. \tag{3.58}$$

Thus, the representations of the Lorentz group can be parametrized by pairs of integers or half-integers, $(j_1, j_2)$, which correspond to the two factors of SU(2). The most important examples of representations are:

- $(0, 0)$ is a scalar;
- $\left(\frac{1}{2}, 0\right)$ and $\left(0, \frac{1}{2}\right)$ are the left and right chiral parts of a Dirac spinor;
- $\left(\frac{1}{2}, 0\right) \oplus \left(0, \frac{1}{2}\right)$ is a Dirac spinor;
- $\left(\frac{1}{2}, \frac{1}{2}\right)$ are four-vectors such as $P_\mu$;
- $(1, 0)$ and $(0, 1)$ are the components of a second rank tensor.

The simplest choice for $Q_a$ is a Majorana spinor in the representation $\left(\frac{1}{2}, 0\right) \oplus \left(0, \frac{1}{2}\right)$. A Majorana spinor is one that is equal to its charge conjugate; that is, if $C$ is the charge conjugation matrix, then $Q_a = C_{ab}\bar{Q}_b$.

Based on the general forms of the odd and even commutation relations in Equation 3.52, one can derive the commutation and anticommutation relationships satisfied by $Q_a$ and the Poincaré group generators:

$$\left[M_{\mu\nu}, Q_a\right] = -\left(\Sigma_{\mu\nu}\right)_{ab} Q_b, \tag{3.59}$$

$$\left[Q_a, P_\mu\right] = 0. \tag{3.60}$$

Further, one can show in terms of the charge conjugation matrix that

$$\{Q_a, Q_b\} = -2\left(\gamma^\mu C\right)_{ab} P_\mu, \tag{3.61}$$

$$\left\{Q_a, \bar{Q}_b\right\} = 2\left(\gamma^\mu\right)_{ab} P_\mu, \tag{3.62}$$

$$\left\{\bar{Q}_a, \bar{Q}_b\right\} = 2\left(C^{-1}\gamma^\mu\right)_{ab} P_\mu. \tag{3.63}$$

The charge conjugation, commutation and anticommuntation relations are all invariant under a chiral rotation that acts on $Q$ by

$$Q_a \to \left(e^{-i\phi\gamma_5}\right)_{ab} Q_b, \tag{3.64}$$

$$\bar{Q}_a \to \bar{Q}_b \left(e^{-i\phi\gamma_5}\right)_{ba}, \tag{3.65}$$

$\phi$ being a real constant. This invariance can be implemented using a unitary operator $e^{i\phi R}$, where $R$ is a U(1) generator:

$$e^{i\phi R} Q_a e^{-i\phi R} = \left(e^{-i\phi\gamma_5}\right)_{ab} Q_b, \tag{3.66}$$

$$e^{i\phi R} \bar{Q}_a e^{-i\phi R} = \bar{Q}_b \left(e^{-i\phi\gamma_5}\right)_{ba}. \tag{3.67}$$

This implies the commutation relation

$$[Q_a, R] = (\gamma_5)_{ab} Q_b. \tag{3.68}$$

which is added to the rest of the superymmetry algebra, along with the additional expressions

$$\left[R, P_\mu\right] = \left[R, M_{\mu\nu}\right] = 0. \tag{3.69}$$

The U(1) symmetry is called R-invariance. The entire collection of commutation relations is the super-Poincaré algebra.

It is also useful to break $Q_a$ down into two Weyl spinors, and rewrite the commutation relations in terms of these components. Consider a two-component Weyl spinor $\xi_A$ in the representation $\left(\frac{1}{2}, 0\right)$, and another such spinor $\bar{\chi}_{\dot{A}}$ in the conjugate representation $\left(0, \frac{1}{2}\right)$. These objects are fermionic fields, where $\xi$ is a two-component column vector and $\bar{\chi}$ is a two-component row vector. Their conjugates in the opposite representations are $\bar{\xi} = \xi^\dagger$ and $\chi = \bar{\chi}^\dagger$. The components

of all of these Weyl spinors are postulated to anticommute amongst themselves. The two Weyl spinors can be used to construct a Dirac spinor by

$$\psi = \begin{pmatrix} \xi_A \\ \bar{\chi}^T \end{pmatrix} \tag{3.70}$$

Its conjugate is

$$\bar{\psi} = \psi^\dagger \gamma^0 = \begin{pmatrix} \chi & \bar{\xi} \end{pmatrix}. \tag{3.71}$$

At the same time, introduce $\theta$ and $\bar{\theta}$ as conjugate two-component Grassmann variables whose components anticommute with themselves and with the fermion fields. Then

$$\theta\theta = -2\theta_1\theta_2, \tag{3.72}$$

$$\bar{\theta}\bar{\theta} = 2\bar{\theta}^1\bar{\theta}^2, \tag{3.73}$$

and any combination of three or more factors of $\theta$ or $\bar{\theta}$ vanishes.

A general Majorana four spinor can be written in Weyl notation as

$$\lambda_a = \begin{pmatrix} \lambda_A \\ \bar{\lambda}^{\dot{A}} \end{pmatrix}. \tag{3.74}$$

Since the supercharge operator is assumed to be such an object, it can be written

$$Q_a = \begin{pmatrix} Q_A \\ \bar{Q}^{\dot{A}} \end{pmatrix}. \tag{3.75}$$

Using this and the charge conjugation matrix, which in the Weyl representation is

$$C = \begin{pmatrix} -i\sigma^2 & 0 \\ 0 & i\sigma^2 \end{pmatrix}, \tag{3.76}$$

all of the commutation and anticommutation relations can be rewritten as

$$\left\{Q_A, \bar{Q}_{\dot{B}}\right\} = 2\sigma^{\mu}_{A\dot{B}} P_\mu, \quad \left\{\bar{Q}^{\dot{A}}, Q^B\right\} = 2\bar{\sigma}^{\mu\dot{A}B} P_\mu, \tag{3.77}$$

$$\{Q_A, Q_B\} = \left\{\bar{Q}^{\dot{A}}, \bar{Q}^{\dot{B}}\right\} = 0, \tag{3.78}$$

$$\left[Q_A, P_\mu\right] = \left[\bar{Q}^{\dot{A}}, P_\mu\right] = 0, \tag{3.79}$$

$$\left[M_{\mu\nu}, Q_A\right] = -\left(\sigma_{\mu\nu}\right)^B_A Q_B, \tag{3.80}$$

$$\left[M_{\mu\nu}, \bar{Q}^{\dot{A}}\right] = -\left(\bar{\sigma}_{\mu\nu}\right)^{\dot{A}}_{\dot{B}} \bar{Q}^{\dot{B}}, \tag{3.81}$$

$$[Q_A, R] = Q_A, \tag{3.82}$$

$$\left[\bar{Q}^{\dot{A}}, R\right] = -\bar{Q}^{\dot{A}}. \tag{3.83}$$

One particularly important consequence is that $P^2$ commutes with $Q$. These relationships will be used extensively in the following section.

### 3.3.3 Supermultiplets

A supermultiplet consists of all particles that are related by the generator $Q$. Since $Q$ commutes with $P^2$, the masses of all particles within a supermulitplet are the same. $Q$ also commutes with internal symmetries and quantum numbers. From the Weyl commutation relations, one can show that

$$\left[J^i, Q_A\right] = -\frac{1}{2}\left(\sigma^i\right)^B_A Q_B \tag{3.84}$$

$$\left[J^i, \bar{Q}^{\dot{A}}\right] = -\frac{1}{2}\left(\bar{\sigma}^i\right)^{\dot{A}}_{\dot{B}} \bar{Q}^{\dot{B}}, \tag{3.85}$$

where $J^i$ is the angular momentum operator. These expression will be used to derive the relationships between the spins of the particles in a supermultiplet. The massless and massive cases will be considered separately.

**Massless case**

Given a massless particle, one can always perform a Lorentz transformation into the frame where the four-momentum has the form $P^\mu = \omega(1,0,0,1)$. Then the $J^3$ operator measures the helicity of the particle. The supersymmetry algebra in this reference frame simplifies to

$$\left\{Q_1, \bar{Q}_{\dot{1}}\right\} = 0, \tag{3.86}$$

$$\left\{Q_2, \bar{Q}_{\dot{2}}\right\} = 4\omega, \tag{3.87}$$

$$\left\{Q_1, \bar{Q}_{\dot{2}}\right\} = \left\{Q_2, \bar{Q}_{\dot{1}}\right\} = 0. \tag{3.88}$$

The first line implies that $Q_1 = \bar{Q}_{\dot{1}} = 0$. This leaves only $Q_2$ and $\bar{Q}_{\dot{2}}$, which are rescaled as follows:

$$Q = \frac{\bar{Q}_{\dot{2}}}{2\sqrt{\omega}}, \tag{3.89}$$

$$\bar{Q} = \frac{Q_2}{2\sqrt{\omega}}. \tag{3.90}$$

Then the supersymmetry algebra becomes

$$\left\{Q, \bar{Q}\right\} = 1, \tag{3.91}$$

$$\{Q, Q\} = \left\{\bar{Q}, \bar{Q}\right\} = 0. \tag{3.92}$$

From the commutation relations with $J^i$,

$$\left[J^3, Q_2\right] = \frac{1}{2}Q_2, \tag{3.93}$$

$$\left[J^3, \bar{Q}_{\dot{2}}\right] = -\frac{1}{2}\bar{Q}_{\dot{2}}. \tag{3.94}$$

Rewriting this in terms of the new $Q$ and $\bar{Q}$ yields

$$J^3 Q = Q\left(J^3 - \frac{1}{2}\right), \tag{3.95}$$

$$J^3 \bar{Q} = \bar{Q}\left(J^3 + \frac{1}{2}\right). \tag{3.96}$$

That is, applying $\bar{Q}$ to an eigenstate of $J^3$ increases the eigenvalue by $1/2$, and applying $Q$ decreases it by $1/2$. This implies that $Q$ must destroy the state with the minimum eigenvalue of $J^3$, and $\bar{Q}$ must destroy the state with the maximum eigenvalue.

Suppose $j_0$ is the maximum eigenvalue. Define the result of acting on this state with $Q$ by

$$\left| j_0 - \frac{1}{2} \right\rangle \equiv Q \left| j_0 \right\rangle . \tag{3.97}$$

Then

$$\bar{Q} \left| j_0 - \frac{1}{2} \right\rangle = \left| j_0 \right\rangle , \tag{3.98}$$

$$Q \left| j_0 - \frac{1}{2} \right\rangle = 0. \tag{3.99}$$

Also, using the relationships between $J^3$ and $Q$,

$$J^3 \left| j_0 - \tfrac{1}{2} \right\rangle = \left( j_0 - \tfrac{1}{2} \right) \left| j_0 - \tfrac{1}{2} \right\rangle , \tag{3.100}$$

$$\bar{Q} \left| j_0 \right\rangle = 0, \tag{3.101}$$

$$J^3 \left| j_0 \right\rangle = j_0 \left| j_0 \right\rangle . \tag{3.102}$$

This demonstrates that the physically relevant states are $|j_0\rangle$ and $\left|j_0 - \frac{1}{2}\right\rangle$.

CPT symmetry dictates that, if the state $|j\rangle$ transforms in some representation $R$, then there is a state $|-j\rangle$ that transforms in the conjugate representation $\bar{R}$. For example, if $R$ and $\bar{R}$ are the representations $\left(\frac{1}{2}, 0\right)$ and $\left(0, \frac{1}{2}\right)$, then there is a massless supermultiplet that pairs a chiral fermion (spin $\frac{1}{2}$, helicity $+\frac{1}{2}$) with a complex scalar (spin 0, helicity 0), and another that pairs the other helicity state of the fermion (spin $\frac{1}{2}$, helicity $-\frac{1}{2}$) with a complex scalar (spin 0, helicity 0). Both of these are irreducible representations of the superalgebra.

If the representation $R$ is self-conjugate, then an irreducible representation of

the superalgebra includes particles with helicities $j_0$, $j_0 - \frac{1}{2}$, $-j_0 + \frac{1}{2}$ and $-j_0$. For example, a gauge supermultiplet consists of a gauge boson (spin 1, helicities 1 and $-1$) and a Majorana fermion called a gaugino (spin $\frac{1}{2}$, helicities $\frac{1}{2}$ and $-\frac{1}{2}$). Another example pairs a graviton (spin 2, helicities 2 and $-2$) with a new fermion called a gravitino (spin $\frac{3}{2}$, helicities $\frac{3}{2}$ and $-\frac{3}{2}$).

**Massive Case**

In the case of a massive particle, one can always perform a Lorentz transformation into the rest frame of the particle, where $P^\mu = (m, 0, 0, 0)$. Then the anticommutation rules become

$$\left\{Q_A, \bar{Q}_{\dot{B}}\right\} = 2m\,(I)_{A\dot{B}}\,, \tag{3.103}$$

$$\{Q_A, Q_B\} = \left\{\bar{Q}_{\dot{A}}, \bar{Q}_{\dot{B}}\right\} = 0. \tag{3.104}$$

Given a state $|m, j, \lambda\rangle$, where $\lambda$ is the third component of the spin $j$, define eigenstates of $P^2$ and $J^3$ as follows:

$$P^2\,|m, j, \lambda\rangle = m^2\,|m, j, \lambda\rangle\,, \tag{3.105}$$

$$J^3\,|m, j, \lambda\rangle = \lambda\,|m, j, \lambda\rangle\,, \tag{3.106}$$

$$\langle m, j', \lambda'|\, m, j, \lambda\rangle = \delta_{j'j}\delta_{\lambda'\lambda} \tag{3.107}$$

There always exists a state that is annihilated by $Q_A$. For example, if $|\psi\rangle$ is annihilated by neither $Q_1$ or $Q_2$, then $|\chi\rangle = Q_1 Q_2\,|\psi\rangle$ is annihilated by both. Similarly, if the state $|\psi\rangle$ is annihilated by one of $Q_1$ or $Q_2$ but not the other, multiply it by the other to create a state that is annihilated by both. In any case, let $|\chi\rangle = |m, j_0, \lambda_0\rangle$ be this state.

From the commutation relations between $P$ and $Q$, we have

$$\left[J^3, \bar{Q}^1\right] = \frac{1}{2}\bar{Q}^1 \tag{3.108}$$

$$\implies J^3\bar{Q}^1 = \bar{Q}^1\left(J^3 + \frac{1}{2}\right), \tag{3.109}$$

and similarly,

$$\left[J^3, \bar{Q}^2\right] = -\frac{1}{2}\bar{Q}^2 \tag{3.110}$$

$$\implies J^3\bar{Q}^2 = \bar{Q}\left(J^3 - \frac{1}{2}\right). \tag{3.111}$$

These expressions imply that the state $\bar{Q}^1 |m, j_0, \lambda_0\rangle$ has $\lambda_0 + \frac{1}{2}$ as its eigenvalue of $J^3$, while the state $\bar{Q}^2 |m, j_0, \lambda_0\rangle$ has $\lambda_0 - \frac{1}{2}$ as its eigenvalue of $J^3$. Finally, the state $\bar{Q}^1\bar{Q}^2 |m, j_0, \lambda_0\rangle$ has eigenvalue $\lambda_0$. Any further applications of $\bar{Q}$ annihilate the state.

Thus, given a particular pair of eigenvalues $(m, j_0)$, there is a $4(2j_0 + 1)$-dimensional representation of the super-Poincaré group. The factor of four comes from the original state plus the results after applying $\bar{Q}^1$, $\bar{Q}^2$, and $\bar{Q}^1\bar{Q}^2$. The factor of $2j_0 + 1$ comes from the number of different possible $\lambda_0$ values. This representation is composed of $2j_0+1$ subspaces with four eigenvalues of $J^3$ each, namely $\lambda_0$, $\lambda_0 + \frac{1}{2}$, $\lambda_0 - \frac{1}{2}$ and $\lambda_0$.

For example, suppose $j_0 = 0$; that is, suppose the particle is a massive scalar. The supermultiplet consists of four states with $J^3 = 0, \pm 1/2, 0$, which form a Weyl spinor, a scalar, and a pseudoscalar. This combination is called a Wess-Zumino supermultiplet. With two Wess-Zumino multiplets, a Dirac spinor can be constructed out of the two Weyl spinors, while the four states with $J^3 = 0$ can be interpreted as two complex scalars called sfermions, which are the superpartners of the left and right components of the Dirac spinor.

As another example, suppose $j_0 = 1/2$. Then the case $\lambda_0 = 1/2$ leads to $J^3$ eigenvalues of $1/2, 1, 0, 1/2$, and the case $\lambda_0 = -1/2$ leads to $J^3$ eigenvalues of $-1/2, 0, -1, -1/2$. In either case, these four fields are a pseudoscalar, vector, and two Weyl spinors that make up a Dirac fermion.

### 3.3.4 Superfields

The theory of supersymmetry is constructed using a coordinate system that has been expanded to include the usual space-time coordinates and two conjugate Grassmann spinorial coordinates: $\left(x^\mu, \theta^A, \bar{\theta}_{\dot{A}}\right)$. A general function of these variables has the form [50]

$$f(\theta, \bar{\theta}) = f_0 + f_1^A \theta_A + \bar{f}_{2\dot{A}} \bar{\theta}^{\dot{A}} + f_3 \theta\theta + \bar{f}_4 \bar{\theta}\bar{\theta} + f_5^A \theta_A \bar{\theta}\bar{\theta} + \bar{f}_{6\dot{A}} \bar{\theta}^{\dot{A}} \theta\theta + f_7 \theta\theta\bar{\theta}\bar{\theta}. \tag{3.112}$$

An infinitesimal transformation of this space can be written

$$\left(x^\mu, \theta, \bar{\theta}\right) \rightarrow \left(x^\mu - i\theta\sigma^\mu\bar{\epsilon} + i\epsilon\sigma^\mu\bar{\theta}, \theta + \epsilon, \bar{\theta} + \bar{\epsilon}\right), \tag{3.113}$$

with $\epsilon$ and $\bar{\epsilon}$ being anticommuting spinor parameters. For a global transformation, $\epsilon$ and $\bar{\epsilon}$ are not functions of $x^\mu$. Then the infinitesimal transformation of $f$ is given by

$$\delta f(z) = \delta x^\mu \partial_\mu f + \delta\theta^A \partial_A f + \delta\bar{\theta}_{\dot{A}} \bar{\partial}^{\dot{A}} f. \tag{3.114}$$

For a linear implementation of supersymmetry, any such transformation should be expressable in terms of $Q$ and $\bar{Q}$ as $\delta f(z) = i\left(\epsilon Q + \bar{\epsilon}\bar{Q}\right) f(z)$. This yields explicit definitions for the operators $Q$ and $\bar{Q}$:

$$Q_A = -i\left(\partial_A + i\sigma^\mu_{A\dot{B}} \bar{\theta}^{\dot{B}} \partial_\mu\right), \tag{3.115}$$

$$\bar{Q}^{\dot{A}} = -i\left(\bar{\partial}^{\dot{A}} + i\theta^B \sigma^\mu_{B\dot{B}} \partial_\mu\right). \tag{3.116}$$

The general form of a superfield is based on the above expression, but generalized to include bosonic and fermionic components. The general expression that includes all Lorentz invariant $Z_2$-even combinations of these objects is

$$F(z) = f(x) + \sqrt{2}\theta\xi(x) + \sqrt{2}\bar{\theta}\chi(x) + \theta\theta M(x) + \bar{\theta}\bar{\theta}N(x) \tag{3.117}$$

$$+\theta\sigma^{\mu}\bar{\theta}A_{\mu}(x) + \theta\theta\bar{\theta}\bar{\lambda}(x) + \bar{\theta}\bar{\theta}\theta\zeta(x) + \frac{1}{2}\theta\theta\bar{\theta}\bar{\theta}D(x). \tag{3.118}$$

This incorporates four scalar fields $f(x)$, $M(x)$, $N(x)$, $D(x)$, one vector field $A_{\mu}(x)$, two left-handed Weyl spinors $\xi_A(x)$, $\zeta(x)$ and two right-handed Weyl spinors $\bar{\chi}^{\dot{A}}(x)$, $\bar{\lambda}^{\dot{A}}(x)$. All of the above are complex. In general, a superfield of this nature is reducible, but some examples of irreducible superfields are chiral and vector fields, which will be defined below.

The covariant derivatives in this space are

$$D_A = \partial_A - i\sigma^{\mu}_{A\dot{B}}\bar{\theta}^{\dot{B}}\partial_{\mu}, \tag{3.119}$$

$$\bar{D}^{\dot{A}} = \bar{\partial}^{\dot{A}} - i\bar{\sigma}^{\mu\dot{A}B}\theta_B\partial_{\mu}. \tag{3.120}$$

A superfield $\Phi$ is chiral if it satisfies

$$\bar{D}_{\dot{A}}\Phi = 0, \tag{3.121}$$

$$D_A\Phi^{\dagger} = 0, \tag{3.122}$$

the two conditions being equivalent to each other. The field $\Phi$ is called left chiral, and the field $\Phi^{\dagger}$ is called right chiral. With a change of variables to $y^{\mu} = x^{\mu} - i\theta\sigma^{\mu}\bar{\theta}$ and $\bar{y}^{\mu} = x^{\mu} + i\theta\sigma^{\mu}\bar{\theta}$, these fields can be rewritten as

$$\Phi(y,\theta) = \phi(y) + \sqrt{2}\theta\xi(y) + \theta\theta F(y), \tag{3.123}$$

$$\Phi^{\dagger}(y,\bar{\theta}) = \phi^*(\bar{y}) + \sqrt{2}\bar{\theta}\bar{\xi}(\bar{y}) + \bar{\theta}\bar{\theta}F^*(\bar{y}). \tag{3.124}$$

A superfield $V$ is real if it satisfies $V = V^{\dagger}$. Such objects are also called vector

superfields. These fields, with the choice of a particular gauge called the Wess-Zumino gauge, can be written as

$$V(z) = \theta\sigma^{\mu}\bar{\theta}A_{\mu}(x) + \theta\theta\bar{\theta}\bar{\lambda}(x) + \bar{\theta}\bar{\theta}\theta\lambda(x) + \frac{1}{2}\theta\theta\bar{\theta}\bar{\theta}D(x). \tag{3.125}$$

Of these components, $A_{\mu}(x)$ is a real gauge field, and $\lambda(x)$ is the corresponding gaugino. The field $D(x)$ does not have a kinetic term and can be eliminated from the system using the equations of motion.

Recall that R-symmetry is a global U(1) gauge invariance of the supersymmetry algebra, in which $\theta \to e^{i\phi}\theta$ and $\bar{\theta} \to e^{-i\phi}\bar{\theta}$. The transformation rules for $Q_A$ and $\bar{Q}_{\dot{A}}$ are

$$Q_A \rightarrow e^{i\phi R}Q_A e^{-i\phi R} = e^{-i\phi}Q_A, \tag{3.126}$$

$$\bar{Q}^{\dot{A}} \rightarrow e^{i\phi R}\bar{Q}^{\dot{A}}e^{-i\phi R} = e^{i\phi}\bar{Q}^{\dot{A}}. \tag{3.127}$$

Thus, the R-charges of $\theta$ and $\bar{Q}$ are 1 and the R-charges of $\bar{\theta}$ and $Q$ are -1. For left and right chiral superfields, an R-transformation can be defined by

$$\Phi \rightarrow \Phi'(x, e^{i\phi}\theta, e^{-i\phi}\bar{\theta}) = e^{i\phi R_{\Phi}}\Phi(x, \theta, \bar{\theta}), \tag{3.128}$$

$$\Phi^{\dagger} \rightarrow \Phi'^{\dagger}(x, e^{i\phi}\theta, e^{-i\phi}\bar{\theta}) = e^{-i\phi R_{\Phi}}\Phi^{\dagger}(x, \theta, \bar{\theta}) \tag{3.129}$$

respectively. That is, the R-charges of $\Phi$ and $\Phi^{\dagger}$ are $R_{\Phi}$ and $-R_{\Phi}$. The R-charges of its individual components are $R(\phi) = R_{\Phi}$, $R(\xi) = -R(\bar{\xi}) = R_{\Phi} - 1$, and $R(F) = R_{\Phi} - 2$. For a vector superfield, the condition of reality requires $R(V) = 0$. Further, the components have R-charges $R(A_{\mu}) = 0$, $R(\lambda) = -R(\bar{\lambda}) = 1$, $R(D) = 0$.

This particular U(1) symmetry cannot be an exact symmetry of nature. For example, the gaugino Majorana mass terms violate this symmetry, but gauginos have to be massive particles. However, the $Z_2$ discrete subgroup with $\phi = \pi$ can be retained.

Given any superfield, its matter parity is defined by $M_p = e^{i\pi R} = (-1)^R$. The corresponding value for each component field is called that component's R-parity, $R_p$. $R_p$ is positive for a vector field, and negative for its fermionic partner.

Consider a chiral superfield $\Phi$. By convention, $R_\Phi$ is either $\pm 1$ or 0. Under the transformation $\theta \to -\theta$, the choice of $R_\Phi = \pm 1$ implies that $\Phi \to -\Phi$, and the choice of $R_\Phi = 0$ implies that $\Phi \to \Phi$. Further, in this chiral superfield, the R-parity of the scalar component is either negative or positive, and that of its fermionic partner is either positive or negative. An initial choice of $\pm 1$ results in a matter-like superfield; that is, its fermionic component is identified with a known elementary particle. The corresponding scalar is a sparticle. The choice of 0 leads to a quanta-like superfield in which the scalar component is the Standard Model particle like the Higgs or a gauge boson, and the corresponding fermion is a Higgsino or a gaugino. These identifications are chosen so that Standard Model particles have positive R-parity, and new particles have negative R-parity.

Let $B$ be the baryon number of a Standard Model particle, let $L$ be its lepton number, and let $S$ be the spin of the particle or its superpartner. Then the matter parity of the associated superfield, and the R-parity of either the particle or its superpartner, can be expressed in terms of $B$, $L$ and $S$ by

$$M_p = (-1)^{3(B-L)}, \tag{3.130}$$

$$R_p = (-1)^{3(B-L)+2S}. \tag{3.131}$$

The basic assumption of the Minimal Supersymmetric Standard Model, which is examined in the next section, is that $R_p$ is an exact symmetry of nature.

### 3.3.5 The Minimal Supersymmetric Standard Model

The Minimal Supersymmetric Standard Model (MSSM) constitutes the minimal extension of the Standard Model to incorporate an $N = 1$ global supersymmetry; that is, a theory with one supersymmetry generator $Q_a$ [51]. In the MSSM, every Standard Model particle acquires a superpartner whose spin differs from it by 1/2. Fermions are partnered with sfermions, which have spin zero. Gauge bosons are partnered with bosinos, which with spin 1/2. The Higgs boson is partnered with a higgsino, which has spin 1/2. The gauginos and higgsinos mix to form charginos and neutralinos.

Using Equation 3.131, the formula for the R-parity of a particle, one can show that all Standard Model particles have $R_p = +1$, while the sfermions, gauginos and higgsinos have $R_p = -1$. R-parity is assumed to be an exact symmetry of this model, which implies that all superpartner particles must be pair-produced in particle interactions where the initial states are Standard Model particles. Moreover, the lightest superpartner must be stable.

A general supersymmetric Lagrangian has the form [52]

$$\mathcal{L} = \left[\Phi_i^\dagger \Phi_i\right]_D + \left[\mathcal{W}(\Phi_i) + \text{h.c.}\right]_F , \tag{3.132}$$

where

$$\mathcal{W}(\Phi_i) = h_i \Phi_i + \frac{1}{2} m_{ij} \Phi_i \Phi_j + \frac{1}{3} f_{ijk} \Phi_i \Phi_j \Phi_k . \tag{3.133}$$

The term $\mathcal{W}$ is called the superpotential, and it must be an analytic function of $\Phi$ only (and not $\Phi^\dagger$). Its hermitian conjugate depends only on $\Phi^\dagger$. The $D$ subscript refers to the general expansion of a vector superfield in Equation 3.125. The field that multiplies $\frac{1}{2}\theta\theta\bar{\theta}\bar{\theta}$ was called $D(x)$, so the expression $\left[\Phi_i^\dagger \Phi_i\right]_D$ represents this component of the vector superfield $\Phi_i^\dagger \Phi_i$. Similarly, the general expression

for a chiral superfield was given in Equation 3.123, where $F(y)$ was the field that multiplied $\theta\theta$. The $F$ superscript indicates this component of $\mathcal{W}(\Phi_i)$ + h.c. These components are selected because they have the correct transformation properties for a supersymmetric Lagrangian density.

A chiral superfield is introduced for every chiral fermion of the Standard Model. The new scalars that constitute the other components of these superfields are

$$\tilde{l}_{1L} = \begin{pmatrix} \tilde{\nu} \\ \tilde{e}^- \end{pmatrix}_L, \quad \tilde{e}_{1R} = \tilde{e}_R, \tag{3.134}$$

$$\tilde{q}_{1L} = \begin{pmatrix} \tilde{u} \\ \tilde{d} \end{pmatrix}_L, \quad \tilde{u}_{1R} = \tilde{u}_R, \quad \tilde{d}_{1R} = \tilde{d}_R. \tag{3.135}$$

The superfields that are associated with the leptons are denoted

$$L_1 = \begin{pmatrix} L_{\nu_e} \\ L_e \end{pmatrix}, \quad \bar{E}_1. \tag{3.136}$$

The superfields associated with the quarks are

$$Q_1 = \begin{pmatrix} Q_u \\ Q_d \end{pmatrix}, \quad \bar{U}_1, \quad \bar{D}_1. \tag{3.137}$$

The index 1 refers to the first generation. The second and third generation superfields have the same structure.

In the gauge sector, a vector superfield is introduced for every Standard Model gauge field. The Standard Model particles are $B_\mu$, $\vec{W}_\mu$, and $g^a_\mu$, which are the gauge bosons associated with the $U(1)_Y$, $SU(2)_L$ and $SU(3)_C$ symmetry groups, respectively. The corresponding Majorana gaugino fields are $\tilde{\lambda}_0$, $\vec{\tilde{\lambda}}$, and $\tilde{g}^a$. These are contained in the vector superfields $V^Y$, $\vec{V}^W$, and $V^a_g$. Each gaugino

field transforms in the adjoint representation of the corresponding gauge group, as does its gauge boson partner.

The Standard Model Higgs sector contains an $SU(2)_L$ doublet field $\phi$ with hypercharge $Y = 1$. However, the MSSM requires two Higgs doublets, the other with $Y = -1$. The second one is designed to couple to the chiral fermions having a weak isospin of $T_{3L} = -1/2$. Call these two Higgs doublets $h_1$ and $h_2$, respectively. Their VEVs are

$$\langle h_1 \rangle = \frac{1}{\sqrt{2}} \begin{pmatrix} v_1 \\ 0 \end{pmatrix}, \tag{3.138}$$

$$\langle h_2 \rangle = \frac{1}{\sqrt{2}} \begin{pmatrix} 0 \\ v_2 \end{pmatrix}. \tag{3.139}$$

In terms of these parameters, the Standard Model gauge boson masses $m_W$ and $m_Z$ are given by

$$m_W = \frac{1}{2} g_2 \sqrt{v_1^2 + v_2^2}, \tag{3.140}$$

$$m_Z = \frac{1}{2} \sqrt{g_Y^2 + g_2^2} \sqrt{v_1^2 + v_2^2}. \tag{3.141}$$

The ratio of the VEVs is defined to be

$$\tan\beta = \frac{v_2}{v_1}, \tag{3.142}$$

which is a free parameter of the theory.

The left chiral fermionic partners to the two Higgs fields are

$$\tilde{h}_{1L} = \begin{pmatrix} \tilde{h}_1^0 \\ \tilde{h}_1^- \end{pmatrix}_L, \quad \tilde{h}_{2L} = \begin{pmatrix} \tilde{h}_2^+ \\ \tilde{h}_2^0 \end{pmatrix}_L. \tag{3.143}$$

Each individual entry is a two-component spinor field in the $\left(\frac{1}{2}, 0\right)$ representation. The Higgs fields and their partners are collectively contained within the

superfields

$$H_1 = \begin{pmatrix} H_1^1 \\ H_1^2 \end{pmatrix}, \quad H_2 = \begin{pmatrix} H_2^1 \\ H_2^2 \end{pmatrix} \tag{3.144}$$

Electroweak symmetry breaking (EWSB) and explicit soft supersymmetry breaking terms both serve to mix gauginos and higgsinos. The charged gauginos and charged higgsinos mix to form the charginos, $\tilde{\chi}^{\pm}_{1,2}$, which are numbered in order of increasing mass. The neutral gauginos consist of two four-component Majorana fields, $\tilde{\lambda}_0$ and $\tilde{\lambda}_3$. They mix with the neutral higgsinos $\tilde{h}^0_1$ and $\tilde{h}^0_2$ to form four physical states, the neutralinos $\tilde{\chi}^0_i$ with $i = 1, \ldots, 4$, again ordered by increasing mass. There are large regions of MSSM parameter space in which the lightest neutralino, $\tilde{\chi}^0_i$, is the lightest of all superpartner particles. Since this particle is charge neutral and stable, it is a Dark Matter candidate.

The Lagrangian for the MSSM can be broadly described as

$$\mathcal{L}_{\text{MSSM}} = \mathcal{L}_{\text{SUSY}} + \mathcal{L}_{\text{soft}}; \tag{3.145}$$

that is, it consists of supersymmetric terms and soft supersymmetry-breaking terms. The supersymmetric component can be further divided into

$$\mathcal{L}_{\text{SUSY}} = \mathcal{L}_g + \mathcal{L}_M + \mathcal{L}_H, \tag{3.146}$$

which are the gauge, matter, and Higgs-Yukawa terms, respectively. The pure gauge part contains terms that involve $V^a$, $\vec{V}_W$ and $V^Y$. The matter part contains terms that involve all of the matter superfields. The Higgs-Yukawa part involves the superpotential $\mathcal{W}_{\text{MSSM}}$ that is defined by

$$\mathcal{W}_{\text{MSSM}} = \mu H_1 \cdot H_2 - f^e_{ij} H_1 \cdot L_i \bar{E}_j - f^d_{ij} H_1 \cdot Q_i \bar{D}_j - f^u_{ij} Q_i \cdot H_2 \bar{U}_j. \tag{3.147}$$

In particular, note the term $\mu H_1 \cdot H_2$, which can be thought of as analogous to the term $\mu h^2$ in the Standard Model. In MSSM, this term represents a generalization of a higgsino mass term.

In the soft supersymmetry-breaking sector, a general Lagrangian takes the form [53]

$$\mathcal{L}_{\text{SOFT}} = -\phi_i^* \left(m^2\right)_{ij} \phi_j + \left(\frac{1}{3} A_{ijk} \phi_i \phi_j \phi_k - B_{ij} \phi_i \phi_j + C_i \phi_i + \text{h.c.}\right) - \frac{1}{2} \left(M \lambda^a \lambda^a + \text{h.c.}\right) \tag{3.148}$$

where $\phi_i$ is the scalar component from some superfield $\Phi_i$, and $\lambda^a$ and $\bar{\lambda}^a$ are two-component gaugino fields. In the MSSM, there is no scalar field $\phi_i$ such that a term of the form $C_i \phi_i$ would be invariant under the Standard Model $\text{SU}(3)_C \times \text{SU}(2)_L \times \text{U}(1)_Y$ symmetry. Therefore this term is not included in the MSSM, but all others are allowed. Explicitly writing out the MSSM superfields, the form of the soft supersymmetry breaking Lagrangian is

$$\begin{aligned} -\mathcal{L}_{\text{SOFT}} \;=\; & \tilde{q}_{iL}^* \left(\mathcal{M}_{\tilde{q}}^2\right)_{ij} \tilde{q}_{jL} + \tilde{u}_{iR}^* \left(\mathcal{M}_{\tilde{u}}^2\right)_{ij} \tilde{u}_{jR} + \tilde{d}_{iR}^* \left(\mathcal{M}_{\tilde{d}}^2\right)_{ij} \tilde{d}_{jR} + \tilde{l}_{iL}^* \left(\mathcal{M}_{\tilde{l}}^2\right)_{ij} \tilde{l}_{jL} \\ & + \tilde{e}_{iR}^* \left(\mathcal{M}_{\tilde{e}}^2\right)_{ij} \tilde{e}_{jR} + \left[h_1 \cdot \tilde{l}_{iL} A_{ij}^e \tilde{e}_{jR}^* + h_1 \cdot \tilde{q}_{iL} A_{ij}^d \tilde{d}_{jR}^* \right. \\ & \left. + \tilde{q}_{iL} \cdot h_2 A_{ij}^u \tilde{u}_{jR}^* + \text{h.c.}\right] + m_1^2 |h_1|^2 + m_2^2 |h_2|^2 + (B\mu h_1 \cdot h_2 + \text{h.c.}) \\ & + \tfrac{1}{2} \left(M_1 \bar{\tilde{\lambda}}_0 P_L \tilde{\lambda}_0 + M_1^* \bar{\tilde{\lambda}}_0 P_R \tilde{\lambda}_0\right) + \tfrac{1}{2} \left(M_2 \bar{\vec{\tilde{\lambda}}} P_L \vec{\tilde{\lambda}} + M_2^* \bar{\vec{\tilde{\lambda}}} P_R \vec{\tilde{\lambda}}\right) \\ & + \tfrac{1}{2} \left(M_3 \bar{\tilde{g}}^a P_L \tilde{g}^a + M_3^* \bar{\tilde{g}}^a P_R \tilde{g}^a\right). \end{aligned} \tag{3.149}$$

One can split this into gaugino mass terms and soft potential terms. The parameters so introduced are:

- $M_{1,2,3}$, the complex gaugino Majorana mass parameters for $\tilde{\lambda}_0$, $\vec{\tilde{\lambda}}$ and $\tilde{g}$ respectively;
- $m_{1,2}$, the real Higgs mass parameters;
- the sfermion mass matrices $\mathcal{M}_{\tilde{q}}^2$, $\mathcal{M}_{\tilde{u}}^2$, $\mathcal{M}_{\tilde{d}}^2$, $\mathcal{M}_{\tilde{l}}^2$ and $\mathcal{M}_{\tilde{e}}^2$, which are all $3 \times 3$ Hermitian matrices;
- the coefficients $A^e$, $A^d$ and $A^u$ of the trilinear supersymmetry-breaking terms, which are general $3 \times 3$ complex matrices;

- the coefficient $B$ of the bilinear breaking term, which is also complex;
- the higgsino coefficient $\mu$.

In total, this theory involves 105 new parameters that are not present in the Standard Model.

### 3.3.6 Minimal Supergravity

Supergravity refers to spontaneous breaking of a local supersymmetry, where the breaking is mediated by gravitational-strength interactions [54]. The breaking occurs in a new sector of the theory, which involves only Standard Model gauge singlet superfields. Then the effects must be transmitted back to the observable sector via a weak coupling. A particular implementation of this is Minimal Supergravity (mSUGRA), which incorporates certain simplifying assumptions that allow the number of free parameters in the model to be reduced from 105 to 5.

Recall the anticommutation relation

$$\left\{Q_a, \bar{Q}_b\right\} = 2\,(\gamma^\mu)_{ab}\,P_\mu. \tag{3.150}$$

When supersymmetry is promoted to a local symmetry, invariance under supersymmetry implies invariance under local coordinate shifts. This is the basis of general relativity; hence the appellation of supergravity.

When an ordinary symmetry is promoted from global to local, one must introduce corresponding gauge bosons. Since supersymmtry is implemented in a fermionic fashion – that is, its spacetime dependence as a local symmetry is

parametrized by a four-component local spinor function $\epsilon(x)$ – one must instead introduce a new four-component real fermionic field $\Psi_\mu$. Its infinitesimal supersymmetry transformation is

$$\delta\Psi_\mu = 2M_{pl}\partial_\mu\epsilon, \tag{3.151}$$

where $M_{pl}$ is the Planck mass. This field can be interpreted as the gravitino, which is the superpartner of the spin-two graviton.

Now terms are required through which the superfield $\Psi$ can couple to matter and gauge superfields. One component of these interactions is the Kähler potential, which is written

$$\mathcal{G} = M_{pl}^2\left[K\left(\frac{\phi_i}{M_{pl}}, \frac{\bar{\phi}^i}{M_{pl}}\right) - \ln\frac{|W(\phi_i)|^2}{M_{pl}^6}\right]. \tag{3.152}$$

In this expression, $\phi_i$ denotes the scalar component of the left chiral superfield $\Phi_i$, and $\bar{\phi}^i$ is the scalar component of the right chiral superfield $\Phi_i$. The superpotential is $W(\phi_i)$, which is shorthand for $W(\Phi_i)$ when it has been evaluated at $\theta = 0$ and $\bar{\theta} = 0$. $W$ is an analytic function of $\Phi_i$ only. Define

$$\mathcal{G}^i_{\ j} \equiv \frac{\partial^2\mathcal{G}}{\partial\phi_i\partial\bar{\phi}^j}, \tag{3.153}$$

which is the Kähler metric and is independent of $W$.

After spontaneous supersymmetry breaking, the gravitino acquires a mass, denoted $m_{3/2}$. The value of this mass can be evaluated by replacing the Kähler potential with its VEV:

$$m_{3/2} = M_{Pl}e^{-\langle G\rangle/(2M_{Pl}^2)}. \tag{3.154}$$

Consider chiral superfields $Z_i$, $\bar{Z}_i$ with scalar components $z_i$, $\bar{z}_i$. Suppose these are in the observable sector, and suppose the hidden sector contains the chiral

superfield $\Sigma$ with a scalar component $\sigma$. Further, for demonstration purposes, assume a particularly simple form for the Kähler potential:

$$\mathcal{G} = -\sum_i z_i \bar{z}^i - H(\sigma, \bar{\sigma}) - M_{Pl}^2 \frac{\ln |W(z_i, \sigma)|^2}{M_{Pl}^6}, \tag{3.155}$$

where

$$W(\Phi_i) = W_0(z_i) + W_h(\Sigma); \tag{3.156}$$

that is, $W$ is a sum of terms from the observable sector and the hidden sector. Using these assumptions, one can show that all scalar massess are given the same value, $m_{3/2}$. Further, in the limit where $M_{Pl} \to \infty$ and $m_{3/2}$ is held fixed, all the $A_{ijk}$ coefficients to the trilinear explicit soft supersymmetry-breaking terms are equal to the same value, $A_0$. Also, the $B_{ij}$ coefficients to the bilinear symmetry-breaking terms are equal the same value, $B_0$. It should be noted that these are boundary conditions, which do not take into account the evolution of the renormalization group with energy scale.

Suppose the assumptions about the function $K$ are relaxed slightly, so that $K$ might not take the particular form given, but so that it depends only on $\sum_i |z_i|^2$. Then the universality of $A_0$ and $B_0$ are preserved, as is the universality of the scalar masses. However, the universal scalar mass is no longer equal to $m_{3/2}$. This constant value is denoted $m_0$. This choice of assumptions essentially imposes a global U($n$) symmetry on the Kähler potential.

Finally, to obtain expressions for the gaugino masses, an additional boundary condition is imposed: namely, that at the grand unification scale, all three gauginos have the same mass, $M_{1/2}$. One can evolve back down to accessible scales and express masses numerically in terms of $M_{1/2}$.

The above formulation is referred to as mSUGRA. So far, the theory has been

written in terms of the parameters $m_0$, $M_{1/2}$, $A_0$ and $B_0$. These are sufficient to determine the sfermion masses at lower energy scales, which depend on $m_0$, $M_{1/2}$ and Standard Model parameters. To this collection, one must add the parameter $\mu$ from the Higgs sector term $B\mu h_1 \cdot h_2$. However, $|\mu|$ can be determined by requiring that the Standard Model mass $m_Z$ take on its experimentally observed value, so the only degree of freedom is in the sign of $\mu$. $B_0$ and $\tan\beta$ are also related by expressions that involve Standard Model masses, so one may trade $B_0$ for $\tan\beta$. Thus, the five parameters of mSUGRA are

$$\left\{m_0, M_{1/2}, A_0, \tan\beta, \text{sign}\,(\mu)\right\}. \tag{3.157}$$

To summarize, every Standard Model particle acquires a partner particle whose spin differs from the original by 1/2. The masses of the new scalar sfermions are determined by the parameter $m_0$, and the masses of the gauginos are determined by the parameter $M_{1/2}$. The explicit soft supersymmetry breaking terms have the coefficient $A_0$, while the Higgs sector is parameterized by $\tan\beta$ and sign $(\mu)$. In large regions of the mSUGRA parameter space, the lightest supersymmetric partner particle is $\tilde{\chi}_1^0$, which is a candidate for Dark Matter.

## 3.4 The Littlest Higgs Model With T-Parity

The class of Little Higgs models take an alternative approach to addressing the hierarchy problem discussed in Section 3.2. Suppose that the Higgs is a composite particle. Then an appropriate value for the cutoff scale $\Lambda$ is the scale at which the new strong interaction between its components become relevant.

There are some phenomenological issues to this approach that must be ad-

dressed. In particular, precision measurements of electroweak observables disfavor the existence of a new interaction below approximately 10 TeV [55], while the cutoff scale needed for naturalness is on the scale of 1 TeV. This discrepant factor of ten is the so-called "little" hierarchy problem. Therefore, additional mechanisms are required to protect the Higgs mass from quadratically divergent corrections above 1 TeV.

One way to preserve the relative lightness of the Higgs boson is to interpret it as a Goldstone boson arising from the spontaneous symmetry breaking of a larger symmetry. This new symmetry cannot be exact, or else the Higgs would be identically massless. In the Little Higgs models, which were proposed by Arkani-Hamed, Cohen and Georgi [56], gauge couplings and Yukawa couplings explicitly break the global symmetry, but they do so in such a way as to prevent quadratically divergent one-loop corrections. The approach is to embed the Standard Model within a larger symmetry group so that multiple symmetries must be broken collectively before quantum corrections to the Higgs mass are generated. One-loop diagrams, which involve only one coupling, do not meet the requirements, and therefore the problematic contributions cancel.

The Standard Model particles acquire partner particles from the larger symmetry group. T-parity, which is posited in analogy to the R-parity of the MSSM [57], assigns even parity to Standard Model particles and odd parity to the majority of the new particles. This restricts the processes by which the new particles can be created, thereby relaxing electroweak precision constraints on the model.

Comprehensive overviews of the Littlest Higgs model and the Littlest Higgs with T-Parity have been compiled [58, 59, 60]. The present discussion summa-

rizes results presented therein.

### 3.4.1 The Littlest Higgs Model

Consider a global SU(5) symmetry that is broken to SO(5) by the vacuum expectation value of a field $\Sigma$ in the symmetric tensor representation. The VEV is assumed to take the form

$$\Sigma_0 = \begin{pmatrix} 0 & 0 & 0 & 1 & 0 \\ 0 & 0 & 0 & 0 & 1 \\ 0 & 0 & 1 & 0 & 0 \\ 1 & 0 & 0 & 0 & 0 \\ 0 & 1 & 0 & 0 & 0 \end{pmatrix}, \tag{3.158}$$

and the symmetry breaking is assumed to occur at a scale $f \sim 1$ TeV. The Littlest Higgs theory embeds the Standard Model in a non-linear sigma model describing the SU(5)/SO(5) symmetry breaking.

Since there are $24 - 10 = 14$ broken generators, this model gives rise to 14 Goldstone boson fields, denoted $\pi^a(x)$ with $a = 1, \ldots, 14$. Define the $\Pi$ field by

$$\Pi(x) = \sum \pi^a X^a, \tag{3.159}$$

where the $X^a$ are the broken generators. Further define the $\Sigma$ field by

$$\Sigma(x) = e^{i\Pi/f}\Sigma_0 e^{i\Pi^T/f}. \tag{3.160}$$

Noting that $X^a\Sigma_0 = \Sigma_0 X^{aT}$, this field can be rewritten as

$$\Sigma(x) = e^{2i\Pi/f}\Sigma_0. \tag{3.161}$$

Next, a subgroup of SU(5) is promoted to a local symmetry. The subgroup in question is $[\mathrm{SU}(2) \times \mathrm{U}(1)]^2$, and its generators are

$$Q_1^a = \begin{pmatrix} \sigma^a/2 & 0 & 0 \\ 0 & 0 & 0 \\ 0 & 0 & 0 \end{pmatrix}, \tag{3.162}$$

$$Y_1 = \mathrm{diag}\,(3, 3, -2, -2, -2)\,/10, \tag{3.163}$$

$$Q_2^a = \begin{pmatrix} 0 & 0 & 0 \\ 0 & 0 & 0 \\ 0 & 0 & -\sigma^{a*}/2 \end{pmatrix}, \tag{3.164}$$

$$Y_2 = \mathrm{diag}\,(2, 2, 2, -3, -3)\,/10. \tag{3.165}$$

In these expressions, $\sigma^a$ represent the Pauli matrices, and the subscripts $1, 2$ indicate the two factors of $\mathrm{SU}(2) \times \mathrm{U}(1)$. Let the gauge fields corresponding to $\mathrm{U}(1)_j$ and $\mathrm{SU}(2)_j$ be $B_j$ and $W_j^a$, and let the corresponding coupling constants be $g'_j$ and $g_j$. Then the derivative $\partial_\mu$ must be replaced by a covariant derivative $D_\mu$, which acts on the sigma field by

$$D_\mu \Sigma = \partial_\mu - i \sum_{j=1}^{2} \left[ g_j W_{j\mu}^a \left( Q_j^a \Sigma + \Sigma Q_j^{aT} \right) + g'_j B_{j\mu} \left( Y_j \Sigma + \Sigma Y_j \right) \right]. \tag{3.166}$$

There are linear combinations of gauge boson fields that acquire masses due to the VEV $\Sigma_0$, while the orthogonal combinations remain massless. Define the following new gauge boson fields:

$$W_L^a = \frac{g_2}{\sqrt{g_1^2 + g_2^2}} W_1^a + \frac{g_1}{\sqrt{g_1^2 + g_2^2}} W_2^a, \tag{3.167}$$

$$W_H^a = -\frac{g_1}{\sqrt{g_1^2 + g_2^2}} W_a^1 + \frac{g_2}{\sqrt{g_1^2 + g_2^2}} W_2^a, \tag{3.168}$$

$$B_L = \frac{g'_2}{\sqrt{g'^2_1 + g'^2_2}} B_1 + \frac{g'_1}{\sqrt{g'^2_1 + g'^2_2}} B_2, \tag{3.169}$$

$$B_H = -\frac{g'_1}{\sqrt{{g'_1}^2 + {g'_2}^2}} B_1 + \frac{g'_2}{\sqrt{{g'_1}^2 + {g'_2}^2}} B_2. \tag{3.170}$$

Mass terms, if they are nonzero, arise from evaluating the kinetic term,

$$\frac{f^2}{8} \mathrm{Tr}\left(D_\mu \Sigma\right) \left(D^\mu \Sigma\right)^\dagger, \tag{3.171}$$

using $\Sigma_0$ in place of $\Sigma$. Substitution yields

$$\begin{aligned} iD_\mu \Sigma \rightarrow & \sum_{j=1}^{2} \left[ g_j W_{j\mu}^a \left( Q_j^a \Sigma_0 + \Sigma_0 Q_j^{aT} \right) + g'_j B_{j\mu} \left( Y_j \Sigma_0 + \Sigma_0 Y_j \right) \right] \\ = & \frac{g_1 g_2}{\sqrt{g_1^2 + g_2^2}} W_L^a \left[ \left( Q_1^a + Q_2^a \right) \Sigma_0 + \Sigma_0 \left( Q_1^{aT} + Q_2^{aT} \right) \right] \\ & + \frac{g'_1 g'_2}{\sqrt{{g'_1}^2 + {g'_2}^2}} B_L \left[ \left( Y_1 + Y_2 \right) \Sigma_0 + \Sigma_0 \left( Y_1 + Y_2 \right) \right] \\ & + \frac{1}{\sqrt{g_1^2 + g_2^2}} W_H^a \left[ \left( g_2^2 Q_2^a - g_1^2 Q_1^a \right) \Sigma_0 + \Sigma_0 \left( g_2^2 Q_2^{aT} - g_1^2 Q_a^{aT} \right) \right] \\ & + \frac{1}{\sqrt{{g'_1}^2 + {g'_2}^2}} B_H \left[ \left( {g'_2}^2 Y_2 - {g'_1}^2 Y_1 \right) \Sigma_0 + \Sigma_0 \left( {g'_2}^2 Y_2 - {g'_1}^2 Y_a \right) \right] \end{aligned} \tag{3.172}$$

The terms associated with $W_L^a$ and $B_L$ vanish, indicating that the associated combinations of generators are not broken by $\Sigma_0$. Thus, the VEV $\Sigma_0$ breaks the $[\mathrm{SU}(2) \times \mathrm{U}(1)]^2$ group down to a diagonal subgroup, denoted $\mathrm{SU}(2)_L \times \mathrm{U}(1)_L$. This will be identified with the electroweak group of the Standard Model. The gauge bosons $W_L$ and $B_L$ remain massless at this stage, but they will acquire masses through the Higgs mechanism of electroweak symmetry breaking. Define the coupling constants corresponding to these gauge bosons by

$$g = \frac{g_1 g_2}{\sqrt{g_1^2 + g_2^2}}, \tag{3.173}$$

$$g' = \frac{g'_1 g'_2}{\sqrt{{g'_1}^2 + {g'_2}^2}}. \tag{3.174}$$

Meanwhile, $W_H$ and $B_H$ obtain nonzero mass terms by absorbing some of the

Goldstone bosons. If the mixing angles $\psi$ and $\psi'$ are defined by

$$\tan\psi = \frac{g_2}{g_1}, \tag{3.175}$$

$$\tan\psi' = \frac{g_2'}{g_1'}, \tag{3.176}$$

then the masses of these heavy bosons can be written

$$m(W_H) = \frac{gf}{\sin 2\psi}, \tag{3.177}$$

$$m(B_H) = \frac{g'f}{\sqrt{5}\sin 2\psi'}. \tag{3.178}$$

Recall the pion field $\Pi(x) = \sum \pi^a X^a$. The 14 Goldstone bosons can be decomposed into representations of the $\mathrm{SU}(2)_L \times \mathrm{U}(1)_L$ group that remains unbroken. The representations they form are

$$1_0 \oplus 3_0 \oplus 2_{1/2} \oplus 3_1, \tag{3.179}$$

where the number indicates the dimension of the representation and the subscript is the hypercharge. Let these four sets of fields be $\eta$, $\omega$, $H$ and $\Phi$, respectively. The $\eta$ and $\omega$ fields are absorbed by the $B_H$ and $W_H^a$ fields to give them their mass. The $H$ field is identified with the Higgs boson. The vector triplet $\Phi$ contains new physical states. The pion field $\Pi$ can be written explicitly in terms of these fields as

$$\Pi = \begin{pmatrix} -\frac{1}{2}\omega^0 - \frac{1}{\sqrt{20}}\eta & -\frac{1}{\sqrt{2}}\omega^+ & \frac{1}{\sqrt{2}}H^+ & -i\Phi^{++} & -\frac{i}{\sqrt{2}}\Phi^+ \\ -\frac{1}{\sqrt{2}}\omega^- & \frac{1}{2}\omega^0 - \frac{1}{\sqrt{20}}\eta & \frac{1}{\sqrt{2}}H^0 & -\frac{i}{\sqrt{2}}\Phi^+ & \frac{1}{\sqrt{2}}\left(-i\Phi^0 + \Phi_P^0\right) \\ \frac{1}{\sqrt{2}}H^- & \frac{1}{\sqrt{2}}H^{0*} & \sqrt{\frac{4}{5}}\eta & \frac{1}{\sqrt{2}}H^+ & \frac{1}{\sqrt{2}}H^0 \\ i\Phi^{--} & \frac{i}{\sqrt{2}}\Phi^- & \frac{1}{\sqrt{2}}H^- & -\frac{1}{2}\omega^0 - \frac{1}{\sqrt{20}}\eta & -\frac{1}{\sqrt{2}}\omega^- \\ \frac{i}{\sqrt{2}}\Phi^- & \frac{1}{\sqrt{2}}\left(i\Phi^0 + \Phi_P^0\right) & \frac{1}{\sqrt{2}}H^{0^*} & -\frac{1}{\sqrt{2}}\omega^+ & \frac{1}{2}\omega^0 - \frac{1}{\sqrt{20}}\eta \end{pmatrix}. \tag{3.180}$$

Consider two different ways in which an SU(3) subgroup can be embedded in the overall SU(5) global symmetry group: in the upper left corner of

the $5 \times 5$ matrices, or in the lower right corner. The gauge generators of the $[\mathrm{SU}(2) \times \mathrm{U}(1)]^2$ group are defined such that $Q_1^a$ and $Y_1$ commute with the SU(3) group in the lower right, while $Q_2^a$ and $Y_2$ commute with the SU(3) group in the upper left. If one of $(g_1, g_1')$ or $(g_2, g_2')$ is set to zero, then the Higgs is the Goldstone boson that corresponds to a breaking of one of the aforementioned global SU(3) symmetries to a global SU(2) symmetry. Therefore, under these conditions, the Higgs must remain exactly massless at all orders of corrections.

Thus, we have succeeded in protecting the Higgs from quadratically divergent one-loop corrections. A one-loop diagram depends on only one of the gauge couplings. Therefore, it is part of the Higgs mass calculation in the special case of the other set of gauge couplings being equal to zero, and thus, its contribution is guaranteed to cancel.

### 3.4.2 The Fermion Sector

Because the top quark is so massive, its coupling to the Higgs boson must be numerically large. The largest loop correction to the Higgs mass comes from the top quark one-loop diagram. Therefore, the Yukawa coupling for the top quark has to be modified to include the collective symmetry breaking pattern.

Introduce two Weyl fermions, $U_L$ and $U_R$. They are weak singlets, and have $Q = +2/3$. Let the Standard Model third-generation quark doublet be $q_{3L} = \begin{pmatrix} u_L \\ b_L \end{pmatrix}$, and let the singlet be $u_{3R}$. Then the new third-generation quark sector takes the form

$$\mathcal{L}_{top} = -\frac{\lambda_1}{2} f \chi_{Li}^\dagger \epsilon_{ijk} \epsilon_{mn} \Sigma_{jm} \Sigma_{kn} u_{3R} - \lambda_2 f U_L^\dagger U_R + \text{h.c.}, \tag{3.181}$$

where $\chi_L = \begin{pmatrix} \sigma_2 q_{3L} \\ U_L \end{pmatrix}$ is an SU(3) triplet, and where $\Sigma_{jm}$ and $\Sigma_{kn}$ range over the upper right $3 \times 2$ block of $\Sigma$; that is, $i, j, k = 1, 2, 3$ and $m, n = 4, 5$.

The mass eigenstates, before electroweak symmetry breaking, are

$$\begin{aligned} t_L &= u_L, \quad t_R = \frac{\lambda_2 u_{3R} - \lambda_1 R_R}{\sqrt{\lambda_1^2 + \lambda_2^2}} \\ T_L &= U_L \quad T_R = \frac{\lambda_1 u_{3R} + \lambda_2 U_R}{\sqrt{\lambda_1^2 + \lambda_2^2}} \end{aligned} \tag{3.182}$$

The mass of the new, heavy top quark is $m(T) = \sqrt{\lambda_1^2 + \lambda_2^2} f$. The Standard Model top quark $t$ is massless at this stage.

This form for $\mathcal{L}_{top}$ has the required collective symmetry breaking pattern. If $\lambda_1 = 0$, then the top and the Higgs are not coupled at all, so the one-loop top diagram cannot contribute to the Higgs mass. If $\lambda_2 = 0$, then the remaining term involves $\chi_L$ and $\Sigma_{jm}$. This preserves the upper-left global SU(3) because $\chi_L$ transforms in its fundamental representation. Thus, the Higgs can be interpreted as the Goldstone boson associated with the spontaneous breaking of a global symmetry, and as per the previous argument, it is identically massless. Any contribution to the Higgs mass must therefore involve both $\lambda_1$ and $\lambda_2$, and so the quadratically divergent terms are forbidden.

### 3.4.3 T-Parity

T-parity is a discrete symmetry that is analogous to the R-parity of the MSSM. It is implemented so that the new particles in the model (with one exception) are T-odd and the Standard Model particles are T-even. There are many phe-

nomenological benefits to assuming this symmetry. For example, T-parity forbids any of the heavy gauge bosons to contribute to electroweak observables at tree-level. This reduces the precision electroweak constraints on the Littlest Higgs model. Also, the lightest T-odd particle is the heavy photon, $B_H$. It is neutral and stable, and therefore it serves as a viable Dark Matter candidate.

In the gauge sector of the model, T-parity acts to exchange the $[\mathrm{SU}(2) \times \mathrm{U}(1)]_1$ and $[\mathrm{SU}(2) \times \mathrm{U}(1)]_2$ factors. The kinetic term

$$\mathcal{L}_{kin} = \frac{f^2}{8} \mathrm{Tr}\left(D_\mu \Sigma\right) \left(D^\mu \Sigma\right)^\dagger \tag{3.183}$$

is invariant under this symmetry provided that

$$g_1 = g_2 \equiv \sqrt{2} g, \tag{3.184}$$

$$g_1' = g_2' \equiv \sqrt{2} g'. \tag{3.185}$$

Under these assumptions, many of the general expressions derived in the previous section are reduced to simpler forms. The heavy gauge bosons that acquire mass are

$$W_H^a = \frac{1}{\sqrt{2}} \left(W_1^a - W_2^a\right), \tag{3.186}$$

$$B_H = \frac{1}{\sqrt{2}} \left(B_1 - B_2\right), \tag{3.187}$$

and their masses are

$$m(W_H) = gf, \tag{3.188}$$

$$m(B_H) = \frac{g' f}{\sqrt{5}}. \tag{3.189}$$

The other combinations are

$$W_L^a = \frac{1}{\sqrt{2}} \left(W_1^a + W_2^a\right), \tag{3.190}$$

$$B_L = \frac{1}{\sqrt{2}} \left(B_1 + B_2\right), \tag{3.191}$$

which are massless before EWSB and are identified with the Standard Model gauge bosons. Based on the action of T-parity, the $H$ bosons are odd and the $L$ bosons are even.

After electroweak symmetry breaking, these masses are somewhat shifted. The mixing angle in the heavy sector is

$$\sin\theta_H \approx \frac{5gg'}{4\left(5g^2 - g'^2\right)}\frac{v^2}{f^2}, \tag{3.192}$$

which is defined in such a way that

$$Z_H = \sin\theta_H B_H + \cos\theta_H W_H^3, \tag{3.193}$$

$$A_H = \cos\theta_H B_H - \sin\theta_H W_H^3. \tag{3.194}$$

The shifted masses are given by

$$m^2(Z_H) = g^2 f^2 - \frac{g^2 v^2}{4} \tag{3.195}$$

$$m^2(A_H) = \frac{g^2 f^2}{5} - \frac{g^2 v^2}{4}. \tag{3.196}$$

T-parity is defined to act on the $\Pi$ field by $\Pi \rightarrow -\Omega\Pi\Omega$, where $\Omega = \mathrm{diag}\,(1, 1, -1, 1, 1)$. The result is that the complex $\Phi$ triplet is T-odd, while the $H$ doublet is even. This means that the coupling $H^\dagger \Phi H$ is forbidden, which closes off another channel whereby the Higgs mass could acquire large correction terms.

### 3.4.4 Fermion Sector with T-Parity

The assumption of T-parity requires that the entire fermion sector be doubled. Introduce two doublets, $\psi_1$ and $\psi_2$, where $\psi_1$ is a doublet under $\mathrm{SU}(2)_1$ and $\psi_2$ is

a doublet under $SU(2)_2$. T-parity acts to interchange these fields. T-odd and T-even combinations of these objects will be defined in such a way that an $f$-scale mass is only acquired by the T-odd combination.

Let $\Psi_1$ and $\Psi_2$ be in the vector representation of the overall SU(5) group, and embed $\psi_1$ and $\psi_2$ within them such that

$$\Psi_1 = \begin{pmatrix} \psi_1 \\ 0 \\ 0 \end{pmatrix}, \quad \Psi_2 = \begin{pmatrix} 0 \\ 0 \\ \psi_2 \end{pmatrix}. \tag{3.197}$$

Now define

$$\Psi^c = \begin{pmatrix} \psi^c \\ \chi^c \\ \tilde{\psi}^c \end{pmatrix}, \tag{3.198}$$

where $\chi^c$ is a singlet and $\psi^c$ is a doublet under $SU(2)_2$. This latter object is introduced so that the T-odd states acquire masses. The transformation laws for these vectors are

$$\Psi_1 \to V^* \Psi_1, \quad \Psi_2 \to V \Psi_2, \tag{3.199}$$

where $V$ is an SU(5) rotation. The action of T-parity is

$$\Psi_1 \to -\Sigma_0 \Psi_2, \quad \Psi^c \to -\Psi^c. \tag{3.200}$$

Then an allowed interaction term is

$$\kappa f \left( \bar{\Psi}_2 \xi \Psi^c + \bar{\Psi}_1 \Sigma_0 \Omega \xi^\dagger \Sigma \Psi^c \right), \tag{3.201}$$

where $\xi = e^{i\Pi/f}$. This is invariant under both SU(5) and T-parity. The doublet $\psi_H = \frac{1}{\sqrt{2}} (\psi_1 + \psi_2)$ acquires a mass $\kappa f$, while $\psi_{SM} = \frac{1}{\sqrt{2}} (\psi_1 - \psi_2)$ remains massless, and is identified with a Standard Model doublet.

The kinetic terms for $\Psi_1$ and $\Psi_2$ are

$$\bar{\Psi}_1 \bar{\sigma}^\mu D^1_\mu \Psi_1 + \bar{\Psi}_2 \bar{\sigma}^\mu D^2_\mu \Psi_2, \tag{3.202}$$

where

$$D^1_\mu = \partial_\mu - i\sqrt{2} g Q^a_1 W^a_{1\mu} - i\sqrt{2} g' Y_1 B_{1\mu} - i\sqrt{2} g' Y_2 B_{2\mu}, \tag{3.203}$$

$$D^2_\mu = \partial_\mu + i\sqrt{2} g \left(Q^a_2\right)^T W^a_{1\mu} - i\sqrt{2} g' Y_1 B_{1\mu} - i\sqrt{2} g' Y_2 B_{2\mu}. \tag{3.204}$$

The values $Y_1$ and $Y_2$ are charges under U(1), and are defined in such a way as to yield the expected values of the electric charge $Q$ for the Standard Model fermions.

After rewriting these in terms of the mass eigenstates, the kinematic terms that arise are

$$\bar{\psi}_{SM} \bar{\sigma}^\mu D^L_\mu \psi_{SM} + \bar{\psi}_H \bar{\sigma}^\mu D^L_\mu \psi_H, \tag{3.205}$$

which is the expected form from the Standard Model and involves the Standard Model covariant derivative, $D^L_\mu$.

The top quark sector proceeds as described in Section 3.4.2. Define two SU(3) multiplets,

$$Q_1 = \begin{pmatrix} q_1 \\ t'_1 \\ 0 \end{pmatrix}, \quad Q_2 = \begin{pmatrix} 0 \\ t'_2 \\ q_2 \end{pmatrix}, \tag{3.206}$$

which transform under SU(5) and T-parity in the same way as $\Psi_1$ and $\Psi_2$. The quark doublets are embedded in these vectors using the definition

$$q_i = -i\sigma_2 \begin{pmatrix} t_{Li} \\ b_{Li} \end{pmatrix}. \tag{3.207}$$

Two additional singlets are required, $t'_{1R}$ and $t'_{2R}$, which transform under T-parity by $t'_{1R} \leftrightarrow -t'_{2R}$. Then the top sector contains the terms

$$\begin{aligned}\mathcal{L}_{top} &= \tfrac{1}{2\sqrt{2}}\lambda_1 f \epsilon_{ijk}\epsilon_{xy}\left[\left(\bar{Q}_1\right)_i\left(\Sigma_{jx}\right)\left(\Sigma_{ky}\right) - \left(\bar{Q}_2\Sigma_0\right)_i\left(\bar{\Sigma}_{jx}\right)\left(\bar{\Sigma}_{ky}\right)\right]u_{3R} \\ &\quad +\lambda_2 f\left(\bar{t}'_1 t'_{1R} + \bar{t}'_2 t'_{2R}\right) + \text{h.c.}.\end{aligned} \tag{3.208}$$

This expression is T-invariant. The extra condition due to T-parity is that the couplings of $t'_1$ and $t'_2$ are equal.

There are three particles in the top sector: the Standard Model top, and the T-even and T-odd partner particles. Define the latter two particles by

$$t'_{\pm} = \frac{1}{\sqrt{2}}\left(t'_1 \mp t'_2\right). \tag{3.209}$$

When the Lagrangian terms are expanded out, the masses of these particles found to be

$$m(t) = \frac{\lambda_1\lambda_2 v}{\sqrt{\lambda_1^2+\lambda_2^2}}, \tag{3.210}$$

$$m(t'_+) = \sqrt{\lambda_1^2+\lambda_2^2}f, \tag{3.211}$$

$$m(t'_-) = \lambda_2 f. \tag{3.212}$$

The T-even quark, which does not have to be pair-produced, is heavier than the T-odd quark. This has the potential to open up decay channels that have no direct analogues in the MSSM. However, this is the exception rather than the rule, and the phenomenologies of the MSSM and the LHT share many common features. The next chapter demonstrates a technique that can be used to distinguish between their experimental signatures.

CHAPTER 4

# A TECHNIQUE FOR MODEL DISCRIMINATION

## 4.1 Overview

As discussed in the previous chapter, the structures of the Minimally Supersymmetric Standard Model (MSSM) and the Littlest Higgs with T-Parity (LHT) theories were both influenced by the same basic theoretical and experimental considerations. Both theories postulate that the Standard Model particles acquire partners whose masses are at the 1 TeV scale. A new conserved quantum number, either R-parity or T-parity, dictates that the new particles must be pair produced (with the exception of the T-even top partner). Finally, the lightest new particle is charge neutral, making it a candidate for Dark Matter.

The primary difference between the two theories is the relationship between the spins of a given Standard Model particle and its partner. In the MSSM, fermions are partnered with scalar bosons, while scalar and vector bosons are partnered with fermions. By contrast, in the LHT, the new particles have the same spins as their Standard Model partners. The following analysis investigates whether this fact can be exploited to distinguish between events that were generated by the two models.

If new particles are observed at CMS, the ultimate goal will be to measure their spins directly. However, this is expected to be a difficult procedure that will require large amounts of data [61]. A more realistic goal is one of model discrimination. Given a set of observations, one can ask which of two candidate models provides the better fit. Such a study would not be sufficiently general

to rule out an entire class of models, such as the class of Little Higgs models; however, it can be used to exclude regions of the parameter space for a specific choice of model, such as the LHT.

This chapter presents the results of a Monte Carlo simulation that compares the LHT to computer-generated data from a particular point in the parameter space of the MSSM. The results were previously published in *Physics Review D* by G. Hallenbeck, M. Perelstein, C. Spethmann, J. Thom, and J. Vaughan [62].

For simplicity, this study will only consider a single process in each model. In the MSSM, the process in question is the pair production of first and second generation squarks, which are the scalar superpartners of the u, d, s and c quarks. In the LHT, the analogous process is chosen: namely, the pair production of first and second generation tquarks, which are the fermion partner particles to the same set of Standard Model quarks. Further, all partner particles will be assumed to decay exclusively to a Standard Model quark and the lightest new particle; that is, $\tilde{q} \to q\tilde{\chi}_1^0$ in the MSSM and $q_H \to qB_H$ in the LHT. We hypothesize that the particles produced in subsequent cascade decays still carry information about the spins of the initial state.

The procedure is as follows. The MSSM is treated as the correct underlying model. After fixing specific parameter values, this model is used to generate a set of events that corresponds to 2 $\text{fb}^{-1}$ of integrated luminosity. These will be treated as though they were data from CMS. Next, a parameter space scan of the LHT is performed in order to determine the point of best fit to the data. This is the point that must be excluded. Ten observable kinematic quantities are defined, and a $\chi^2$ test is performed to compare the MSSM values to the LHT values.

## 4.2 Simulation of MSSM and LHT Datasets

The following MSSM parameters are used to create the simulated data:

$$\begin{aligned}
m(\tilde{Q}_L^{1,2}) &= m(\tilde{u}_R^{1,2}) = m(\tilde{d}_R^{1,2}) = 500\ \text{GeV} \\
m(\tilde{Q}_L^{3}) &= m(\tilde{u}_R^{3}) = m(\tilde{d}_R^{3}) = 1\ \text{TeV}, \\
m(\tilde{L}^{1,2,3}) &= m(\tilde{e}_R^{1,2,3}) = 1\ \text{TeV}, \\
A_{Q,L}^{1,2,3} &= 0, \\
M_1 = 100\ \text{GeV},&\quad M_2 = 1\ \text{TeV},\quad M_3 = 3\ \text{TeV}, \\
m_{1,2} = 1\ \text{TeV},&\quad \mu = 1\ \text{TeV},\quad \tan\beta = 10.
\end{aligned} \tag{4.1}$$

The first and second generation squark masses are set to 500 GeV, while the third generation squark masses are set to 1 TeV so that their production is suppressed. The slepton masses are likewise set to 1 TeV. All of the trilinear coefficients $A_{ijk}$ are set to zero. The masses of the bino, wino and gluino are $M_1 = 100$ GeV, $M_2 = 1$ TeV and $M_3 = 3$ TeV, respectively. The Higgs and higgsino mass parameters are all set to 1 TeV, and the ratio of Higgs expectation values is $\tan\beta = 10$.

With these parameters, squark pair production is dominated by the first two generations, and the only available decay channel is to $q\tilde{\chi}_1^0$, as desired. Gluino production is kinematically suppressed because of its high mass. The $\tilde{\chi}_1^0$ is essentially a bino, and is the lightest R-odd particle.

In the LHT, the first and second generation tquarks are assumed to be degenerate with mass $M_Q$. They are only permitted to decay to $qB_H$, where $B_H$ is the heavy photon with mass $M_B$. These two masses are the only parameters, so a parameter space scan is computationally feasible. 125 evenly spaced points are chosen within the region defined by $M_Q \in [500\,\text{GeV}, 950\,\text{GeV}]$ and $M_B \in [100\,\text{GeV}, M_Q]$. At each point, a dataset with 2 fb$^{-1}$of integrated luminos-

ity is generated.

The event generation proceeds in two steps. The first step, which is performed by MadGraph/MadEvent [22], includes the processes $pp \to \tilde{q}\tilde{q}$ and $\tilde{q} \to q\tilde{\chi}_1^0$ for the MSSM events, and the processes $pp \to q_H q_H$ and $q_H \to qB_H$ for the LHT events. In all cases, the initial proton-proton collisions are simulated to have a 10 TeV center-of-mass energy. The output is then read in by Pythia [23], which performs the showering and hadronization of the quarks.

The output of the event generation must be sent through a simulation of the CMS detector. Due to limitations of computer resources, it is not possible to use the full CMSSW simulation for all points. Instead, the Pretty Good Simulation (PGS) [63] code is used, after its jet output has been tuned to sample outputs from CMSSW_1_6_7. The jet and $\not{E}_T$ spectra from the PGS, after including jet corrections, are a good match for outputs from the full simulation, as shown in Figure 4.1

## 4.3 Signal and Backgrounds

The following event selection criteria are applied for this analysis:

- There are two or more jets, where the lead jet has $p_T > 150$ GeV and the second lead jet has $p_T > 100$ GeV, and where both jets have $|\eta| < 1.7$.
- There are no identified leptons, be they e, $\mu$ or $\tau$.
- The missing transverse energy satisfies $\not{E}_T \geq 300$ GeV.

The Standard Model background events of relevance to this signal are:

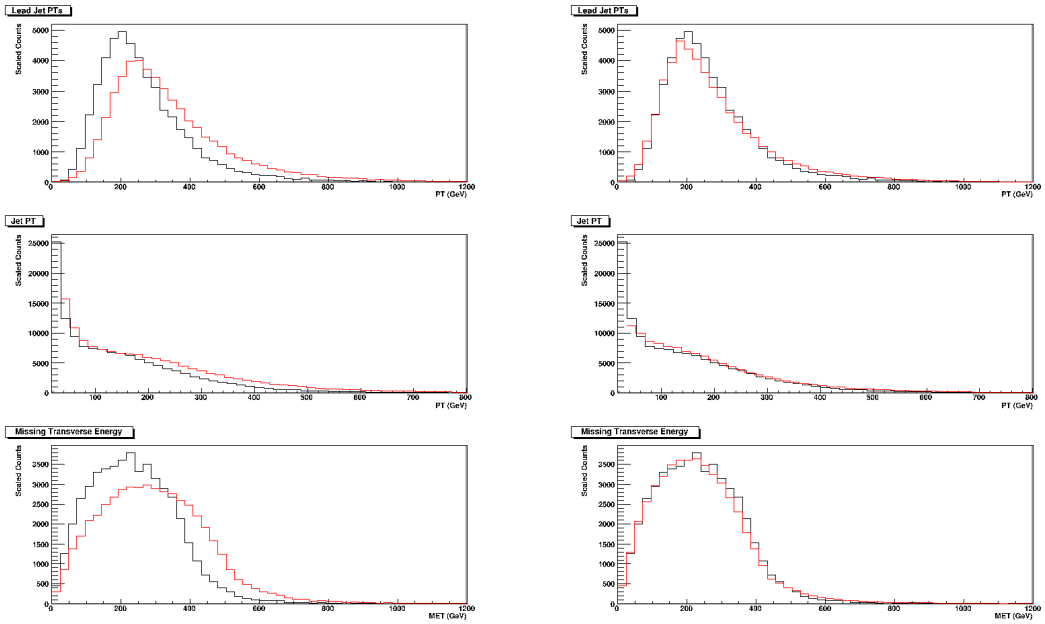


Figure 4.1: Comparison of jet and $\not{E}_T$ distributions from the PGS (red) to those from CMSSW (black). The plots on the left show the original outputs, and those on the right show the outputs after corrections from CMSSW have been applied to the PGS jets.

- Z + 2 jets events in which the Z decays invisibly.
- W + 2 jets events in which the W decays leptonically but the lepton is not identified.
- W + 1 jet events in which the W decays to a $\tau$, and the $\tau$ decays hadronically and is identified as a jet.
- $t\bar{t}$ leptonic or semileptonic events in which the leptons are not identified.

For each background process, two sets of events are simulated. One set is added to the MSSM dataset, and the other is added to the LHT dataset at each parameter space point. In this way, the effect of these backgrounds is included in the results. After the event selection has been applied, the signal and background

counts in the MSSM plus backgrounds sample are found to satisfy $S/B = 1.0$ and $S/\sqrt{B} = 36$ in a dataset corresponding to 2 fb$^{-1}$.

Background events in this channel can also come from dijet QCD processes where the amount of missing energy is incorrectly measured. As discussed in Section 2.5.7, this effect is difficult to accurately simulate. Therefore, for the purposes of this preliminary study, the QCD background is not included. Subsequent studies should include a data-driven assessment of the effect of this process.

## 4.4 Observables

This analysis uses ten different observables to compare the MSSM simulated data to each point in LHT parameter space. The observables are either averages or counts that have been calculated over all events that pass the event selection criteria. They are summarized below.

- $\sigma_{\text{eff}}$ is the cross section in pb of the selected events. It is found by dividing the number of selected events by the total cross section of 2000 pb$^{-1}$; that is, $\sigma_{\text{eff}} = N_{obs}/\mathcal{L}_{tot}$.
- $\langle p_T \rangle$ is the average transverse momentum of all jets with $p_T > 100$ GeV in all selected events. In the LHT models, this is seen to be tightly correlated with $M_Q - M_B$.
- $\langle |\sum \eta| \rangle$ is the average over all selected events of $|\eta_1 + \eta_2|$, where $\eta_1$ and $\eta_2$ are the pseudorapidities of the two leading jets.

- $\langle H_T \rangle$ is the average over all selected events of $H_T = \sum_{\text{jets}} p_T + \not{E}_T$, where the sum is a scalar sum over all jets in the event.
- $\langle \not{E}_T \rangle$ is the average over all selected events of the missing transverse energy.
- The beamline asymmetry is BLA $= (N_+ - N_-) / (N_+ + N_-)$, where $N_+$ is the number of events with $\eta_1 \eta_2 > 0$ and $N_-$ is the number of events with $\eta_1 \eta_2 < 0$. The pseudorapidities are those of the two leading jets.
- The directional asymmetry is DA $= (N_+ - N_-) / (N_+ + N_-)$, where $N_+$ is now the number of events with $\vec{p}_1 \cdot \vec{p}_2 > 0$ and $N_-$ is the number of events with $\vec{p}_1 \cdot \vec{p}_2 < 0$. The momenta are those of the two leading jets.
- The transverse momentum asymmetry is PTA $= N^+/N^-$, where $N^+$ is the number of jets with $p_T > \langle p_T \rangle$ and $N^-$ is the number of jets with $p_T < \langle p_T \rangle$.
- Let $N_1$ be the number of jets with $100 < p_T < 300$ GeV, let $N_2$ be the number of jets with $300 < p_T < 500$ GeV, and let $N_3$ be the number of jets with $p_T > 500$ GeV. Then the jet bin ratios are defined by $R_1 = N_2/N_1$ and $R_2 = N_3/N_1$.

The values of these observables that are calculated from the MSSM plus background dataset are said to be the measured values. Each point in LHT parameter space represents a hypothesis for the underlying model that led to these observed values. When the observables are measured on a particular LHT plus background dataset, the results are the expected values predicted by that hypothesis. The goal is to reject the LHT hypotheses by comparing the measured and expected values. The quality of fit is estimated using a standard $\chi^2$ technique.

## 4.5 Statistical methods and systematic uncertainties

The systematic uncertainty of an individual jet $p_T$ measurement is calculated by

$$\sigma_{pT} = \left( \frac{5.6}{p_T^{pgs}} + \frac{1.25}{\sqrt{p_T^{pgs}}} + 0.035 \right) p_T^{meas}, \tag{4.2}$$

where $p_T^{pgs}$ is the original PGS output and $p_T^{meas}$ is the corrected value. This expression was shown in Section 2.5.6, and reflects the remaining uncertainty in jet momentum resolution after jet corrections have been applied.

The jet corrections also affect the $\not{E}_T$ value in an event. The value generated by the PGS is corrected to the final measured value using the expression

$$\not{E}_T^{meas} = \not{E}_T^{pgs} + \sum_{\text{jets}} \left( p_T^{pgs} - p_T^{meas} \right), \tag{4.3}$$

where the sum is a vector sum in the transverse plane. Then the uncertainty in an individual $\not{E}_T$ measurement is given by

$$\sigma^2_{\not{E}_T} = (3.8 \text{ GeV})^2 + (0.97)^2 \text{ GeV}\not{E}_T + (0.012\not{E}_T)^2 , \tag{4.4}$$

as described in Section 2.5.7.

Recall that $H_T$ is the scalar sum of the $\not{E}_T$ and jet $p_T$ values in each event. Therefore, the total uncertainty in an individual $H_T$ measurement is the sum in quadrature of the uncertainties of the summands.

The observables used in this study fall into one of two categories: average values, or quantities that are calculated from counts. Different approaches are taken to calculate their statistical and systematic uncertainties.

First, consider an average value. The following remarks apply to any of $\langle p_T \rangle$, $\langle \not{E}_T \rangle$, or $\langle H_T \rangle$. Suppose the quantity in question has been tabulated for all events

that pass the event selection criteria. The observable is the mean value of this distribution of observed values. The statistical uncertainty on the mean value is given by

$$\sigma^2_{stat} = \frac{V}{N}, \tag{4.5}$$

where $V$ is the variance of the distribution and $N$ is the number of observations. The systematic uncertainty is estimated by

$$\sigma^2_{sys} = \frac{\nu^2}{N}, \tag{4.6}$$

where $\nu$ is the mean value of the distribution.

For $\langle|\sum \eta|\rangle$, the mean of the sum of the jet $\eta$ values, the statistical uncertainty is calculated as described above, while the systematic uncertainty is given by

$$\sigma^2_{sys} = \frac{w_C^2}{2N}, \tag{4.7}$$

where $w_c = 0.087$ is the width, in angular units, of a calorimeter cell. Recall from Section 2.4.5 that a single scintillating tile in the HCAL covers a solid angle of $\Delta\eta \times \Delta\phi = 0.087 \times 0.087$.

Now consider observables that are composed of counts. Any count $N$ is assumed to have a Poisson statistical uncertainty: that is, $\sigma_N = \sqrt{N}$. For variables of the form $A = (N^+ - N^-)/(N^+ + N^-)$, this leads to a variance of

$$\sigma^2_A \approx \left(\frac{\partial A}{\partial N^+}\right)^2 \sigma^2_{N^+} + \left(\frac{\partial A}{\partial N^-}\right)^2 \sigma^2_{N^-} = \frac{4N^+N^-}{(N^+ + N^-)^3}. \tag{4.8}$$

Variables of the form $R = N^+/N^-$ have a variance of

$$\sigma^2_R = \frac{N^+N^- + (N^+)^2}{(N^-)^3}. \tag{4.9}$$

The effective cross section, which is defined by $\sigma_{\text{eff}} = N_{obs}/\mathcal{L}$, is treated as a special case. The statistical uncertainty is

$$\sigma_{stat} = \frac{\sigma_{\text{eff}}}{\sqrt{N_{obs}}} \tag{4.10}$$

and the systematic uncertainty is assumed to be

$$\sigma_{sys} \approx 0.3\sigma_{\text{eff}}. \tag{4.11}$$

This is a conservative value that was chosen before studies of the CMS luminosity measurement had been performed.

A procedure is required for estimating the covariances between the observables. This information is expected to significantly affect the overall $\chi^2$ value. Ideally, at a given point in LHT parameter space, one would simulate some number $N$ of independent samples and use them to calculate the covariance

$$V_{ab} = \Big\langle (O_a - \langle O_a \rangle)\ \ (O_b - \langle O_b \rangle) \Big\rangle \tag{4.12}$$

for all pairs of observables $O_a$ and $O_b$. However, this is computationally prohibitive, given that 2 fb$^{-1}$ of data would be required for each of the $N$ samples. Instead, a bootstrap method is employed to estimate the covariances from a single sample.

Fix a particular sample of LHT plus background events, and divide it into $N_{sub}$ disjoint subsamples. Then the values of the observables can be calculated within each subsample. These $N_{sub}$ different values of the observables $O_a$ and $O_b$ can be used to calculate standard deviations $\sigma_a$ and $\sigma_b$, and covariances $V_{ab}$. This procedure is repeated $N_R$ times, choosing a different set of $N_{sub}$ subsamples at each iteration. Define

$$C_{ab} = \frac{1}{N_R} \sum_{i=1}^{N_R} \frac{V_{ab}^{(i)}}{\sigma_a^{(i)} \sigma_b^{(i)}}, \tag{4.13}$$

where $V_{ab}^{(i)}$ and $\sigma_{a,b}^{(i)}$ are calculated in iteration $i$. Now let $\sigma_a^{tot}$ be the total uncertainty associated with $O_a$ as described above, including statistical and systematic sources. The average correlation matrix elements in Equation 4.13 are

extrapolated to the full sample by

$$V_{ab}^{tot} = C_{ab}\sigma_a^{tot}\sigma_b^{tot}. \tag{4.14}$$

These covariance values are used in the $\chi^2$ statistical analysis.

This procedure does not yield any information concerning the effective cross section, because the number of events that pass the selection cuts is randomized within each subsample. Therefore, $\sigma_{\text{eff}}$ is assumed to be uncorrelated with the rest of the observables.

Given a $k$-dimensional Gaussian vector $Y$ with mean vector $\mu$ and covariance matrix $V$, the value

$$X = (Y - \mu)^T V^{-1} (Y - \mu) \tag{4.15}$$

is $\chi^2$ distributed with $k$ degrees of freedom [64]. For this study, $Y$ is the vector of observables that are measured on the MSSM plus backgrounds dataset, these being the observed values. The vector $\mu$ contains the observables that are measured on a given LHT plus backgrounds dataset, and $V$ is the matrix of covariances that is calculated using the bootstrap method. The quality of fit of this LHT point to the simulated data is assessed by comparing the resulting value $X$ to a standard $\chi^2$ table with ten degrees of freedom. Values far from 0 indicate a poor fit, and serve to exclude that LHT point. The following section shows the exclusion plots that are generated by these numbers.

## 4.6 Results and Conclusions

Figure 4.2 shows exclusion plots of the LHT parameter space for four different luminosities: 200 pb$^{-1}$, 500 pb$^{-1}$, 1 fb$^{-1}$ and 2 fb$^{-1}$. The exclusions were calcu-

lated using a fit to all ten observables. With 2 fb$^{-1}$, all of the points chosen for this study can be excluded to at least $3\sigma$.

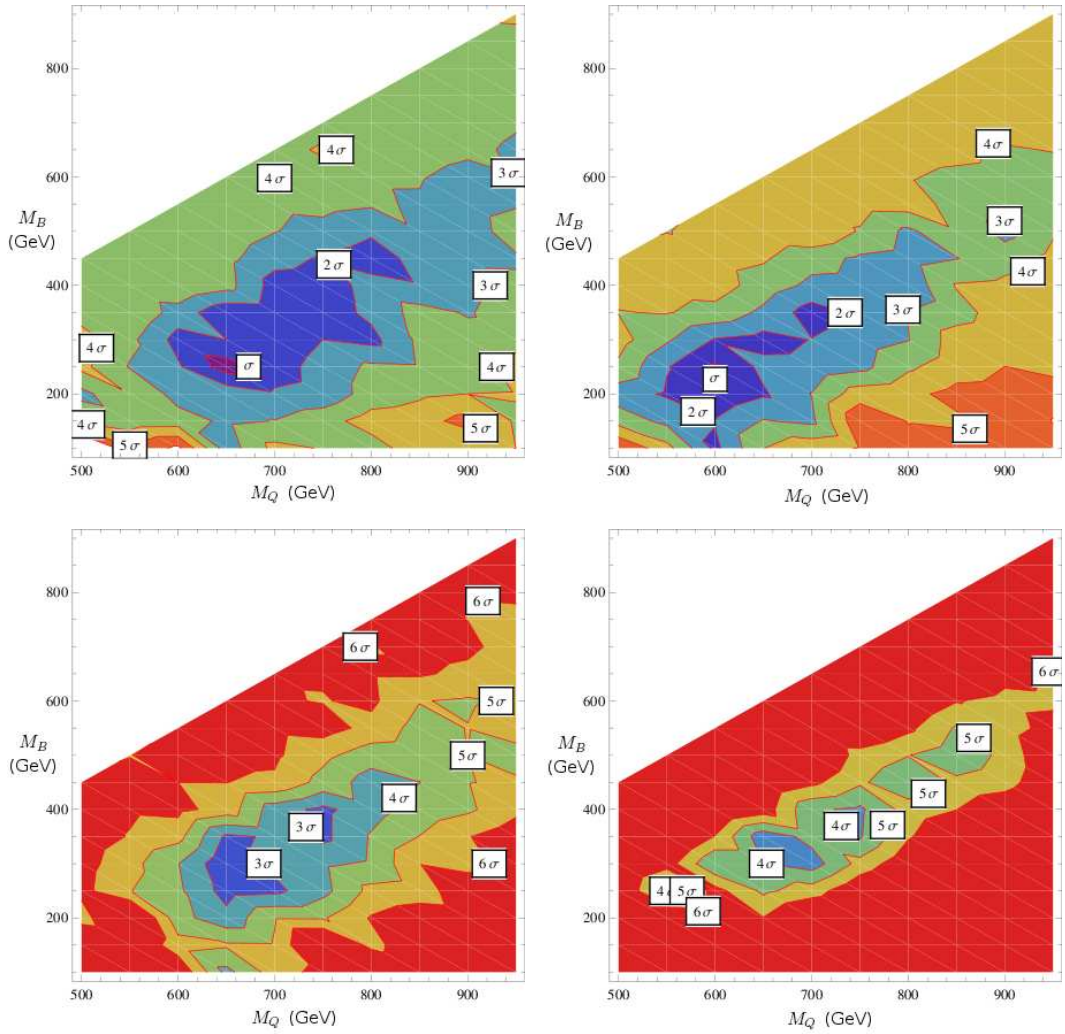


Figure 4.2: Exclusion plots in LHT parameter space using all ten observables. The top row shows the results from luminosities of 200 pb$^{-1}$ and 500 pb$^{-1}$, while the bottom row shows the results from luminosities of 1 fb$^{-1}$ and 2 fb$^{-1}$. When 2 fb$^{-1}$ of integrated luminosity are analyzed, all points in the LHT parameter space that were considered in the study can be excluded to at least $3\sigma$.

As stated in the previous section, the total production cross section is assumed to have a 30% systematic uncertainty. Some of the issues that could affect the cross section are features specific to the LHT model, such as the number of

generations of quarks, or unforeseen decay channels. These would not impact any of the other observables. Thus, it is instructive to redo the analysis without including the effective cross section. Figure 4.3 repeats the exclusion plot for 2 $\text{fb}^{-1}$ without including the cross section. Omitting this observable has only a small impact on the discrimination power of the method.

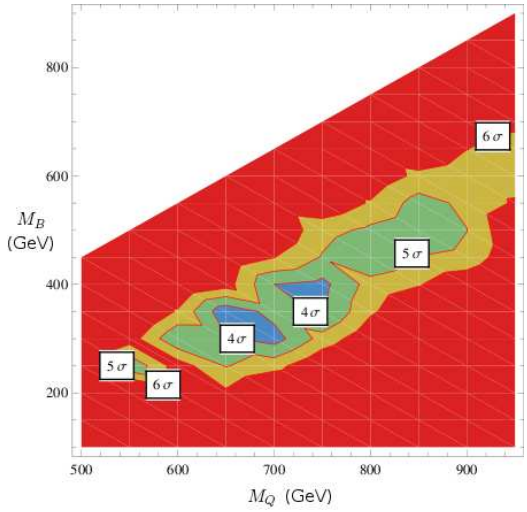


Figure 4.3: Exclusion plot in LHT parameter space using all observables except the effective cross section. The results are not markedly different from the previous figure.

The $\not{E}_T$ resolution is subject to systematic uncertainties that are difficult to model in simulation, as discussed in Section 2.5.7. Both $\langle \not{E}_T \rangle$ and $\langle H_T \rangle$ depend on missing transverse energy measurements. To determine the dependence of the analysis on the $\not{E}_T$ measurement, the 2 $\text{fb}^{-1}$ exclusion plot is recreated once more, this time omitting $\langle \not{E}_T \rangle$ and $\langle H_T \rangle$ from the list of observables. The result is shown in Figure 4.4. In this scenario, the exclusions placed on the parameter space are noticeably weaker. Avoiding reliance on $\langle \not{E}_T \rangle$ and $\langle H_T \rangle$ might make the analysis less prone to systematic uncertainties, but it comes at the cost of requiring more data to make a $3\sigma$ exclusion.

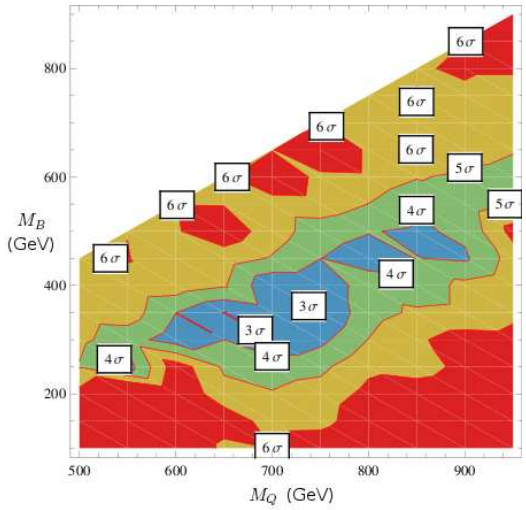


Figure 4.4: Exclusion plot in LHT parameter space using all observables except $\langle \not{E}_T \rangle$ and $\langle H_T \rangle$. The exclusion curves are noticeably weaker when these variables are not included.

Although this study is preliminary and contains simplifying assumptions, it demonstrates the potential for large regions of parameter space in a new physics model to be excluded with only 2 fb$^{-1}$of data. This amount of integrated luminosity is attainable within the next few years of CMS running.

The remainder of this document is devoted to a more detailed study of the data collected at CMS as of November 2010.

CHAPTER 5

# A SEARCH FOR SUSY IN A MULTI-LEPTONIC CHANNEL

## 5.1 Overview

There are many competing theories to describe physics beyond the Standard Model. Moreover, within a given theory such as MSSM, there may be a multi-dimensional continuous parameter space, different points of which can lead to different phenomenologies. Using Monte Carlo simulations, one can generate predictions due to a specific model and a specific choice of parameters, and one can perform model discrimination studies such as that of the previous chapter. However, for the detection of a new physics signal, an analysis is preferred that does not depend so heavily on a particular hypothesis for new physics.

The channel in which we will search for a new physics signal is that with exactly two electrons and at least two jets. A Monte Carlo study to assess the feasibility of detecting new physics in this channel has been performed previously [65]. This channel is considered to be a promising one because the expected Standard Model backgrounds are small, and can either be estimated from Monte Carlo simulations or measured by data-driven methods.

One feature that is common to most new physics models is the presence of a Dark Matter candidate. Since this particle, by construction, cannot be directly observed, new physics events are characterized in the CMS detector by large missing energy. Therefore, the search will occur in the high-$\not\!\!E_T$ region, which we define to be $\not\!\!E_T > 150$ GeV.

This analysis is performed on CMS observations that were recorded between

March and November 2010. Specifically, we use the electron-triggered primary dataset, and select those events that fall within the chosen decay channel criteria. The number of such events in the signal region constitutes the observation from data.

In order to test the hypothesis that this sample contains new physics events as well as Standard Model events, estimates are required for the numbers of events due to each of the Standard Model processes that contribute to this channel. In cases where computer simulations are expected to be reliable, such as electroweak processes, the estimates are taken from Monte Carlo simulations. For events due to QCD, which are difficult to model accurately, a data-driven method for estimating the signal region contribution is developed. These estimates, taken in total, represent the background. The signal is then defined to be the difference between data and background.

In the following sections, we list the CMS and Monte Carlo datasets used in this analysis, and the precise event selection criteria and analysis object definitions. Preliminary background estimates are given for those processes that are taken from Monte Carlo simulations. The data-driven method for estimating the QCD background in this channel is described in Chapter 6. Finally, the overall data and background results are given in Chapter 7, including a discussion of statistical and systematic uncertainties. A statistical model is shown for propagating the uncertainties, extracting the signal, and assessing its significance.

## 5.2 Datasets and Analysis Objects

### 5.2.1 Datasets and Software

After events have been recorded, a JavaScript Object Notation (JSON) file is compiled that lists the luminosity sections from different run numbers that have been certified for physics processing. The CMS events used in this analysis were obtained using the JSON file certified on 15 November 2010 [66], which covers the run number range 132440 – 149442. The electron-triggered primary datasets and their total luminosities are shown in Table 5.1. All luminosities were obtained using the official luminosity calculation tool [67].

Table 5.1: Total luminosities for electron primary datasets.

| Electron-Triggered Dataset | Luminosity ($pb^{-1}$) |
|---|---|
| `/EG/Run2010A-Nov4ReReco_v1/AOD` | 3.06 |
| `/Electron/Run2010B-PromptReco-v2/AOD` | 30.78 |
| Total | 33.84 |

The samples are analyzed using `CMSSW_3_8_6` and privately created ntuples that are based on PAT objects. Beam scraping events are removed by requiring that at least 25% of the tracks in the event be of high purity. Each event is required to contain a good vertex; that is, one that has a number of degrees of freedom > 4, a longitudinal impact parameter $|z| < 24$ cm, and a transverse impact parameter $d_0 < 2$ cm. These are the official recommendations for early data analysis [68].

The Monte Carlo datasets that are used to obtain Standard Model background estimates are listed in Table 5.2. Additional Monte Carlo files that are

used in studies of systematic uncertainties and other effects are listed in Table 5.3. Each dataset is weighted in such a way as to represent 33.84 $pb^{-1}$of data. The weights are calculated using the number of simulated events and the cross sections [69] associated with each process. Next-to-leading order (NLO) or next-to-next-to-leading order (NNLO) values are used where available [70]. These numbers are listed in Table 5.4.

Table 5.2: Monte Carlo datasets used to obtain Standard Model background estimates.

| Name | Dataset |
|---|---|
| Zjets | /DYToEE_M-20_TuneZ2_7TeV-pythia6/Fall10-START38_V12-v1/AODSIM |
| TTjets | /TTJets_TuneZ2_7TeV-madgraph-tauola/Fall10-START38_V12-v3/AODSIM |
| WW | /WWtoAnything_TuneZ2_7TeV-pythia6-tauola/Fall10-START38_V12-v1/AODSIM |
| WZ | /WZtoAnything_TuneZ2_7TeV-pythia6-tauola/Fall10-START38_V12-v1/AODSIM |
| ZZ | /ZZtoAnything_TuneZ2_7TeV-pythia6-tauola/Fall10-START38_V12-v1/AODSIM |

Table 5.3: Monte Carlo datasets used in systematic uncertainty studies.

| Name | Dataset |
|---|---|
| Wjets | /WToENu_TuneZ2_7TeV-pythia6/Fall10-START38_V12-v1/AODSIM |
| QCD01 | /QCD_Pt_30to50_TuneZ2_7TeV_pythia6/Fall10-START38_V12-v1/AODSIM |
| QCD02 | /QCD_Pt_50to80_TuneZ2_7TeV_pythia6/Fall10-START38_V12-v1/AODSIM |
| QCD03 | /QCD_Pt_80to120_TuneZ2_7TeV_pythia6/Fall10-START38_V12-v1/AODSIM |
| QCD04 | /QCD_Pt_120to170_TuneZ2_7TeV_pythia6/Fall10-START38_V12-v1/AODSIM |
| QCD05 | /QCD_Pt_170to300_TuneZ2_7TeV_pythia6/Fall10-START38_V12-v1/AODSIM |
| QCD06 | /QCD_Pt_300to470_TuneZ2_7TeV_pythia6/Fall10-START38_V12-v1/AODSIM |
| QCD07 | /QCD_Pt_470to600_TuneZ2_7TeV_pythia6/Fall10-START38_V12-v1/AODSIM |
| QCD08 | /QCD_Pt_600to800_TuneZ2_7TeV_pythia6/Fall10-START38_V12-v2/AODSIM |
| QCD09 | /QCD_Pt_800to1000_TuneZ2_7TeV_pythia6/Fall10-START38_V12-v1/AODSIM |
| QCD10 | /QCD_Pt_1000to1400_TuneZ2_7TeV_pythia6/Fall10-START38_V12-v1/AODSIM |
| QCD11 | /QCD_Pt_1400to1800_TuneZ2_7TeV_pythia6/Fall10-START38_V12-v1/AODSIM |
| QCD12 | /QCD_Pt_1800_TuneZ2_7TeV_pythia6/Fall10-START38_V12-v1/AODSIM |

### 5.2.2 Electron Definition

We require electrons to satisfy the official vector boson task force (VBTF) recommendations [71] that correspond to 80% efficiency. Electron $p_T$ and $\eta$ restrictions

Table 5.4: Cross sections and weights for each dataset such that the end product represents a luminosity of 33.84 $pb^{-1}$. Cross sections are leading order unless otherwise noted.

| Name | Cross Section (pb) | # Events | Weight |
|---|---|---|---|
| Zjets | 1666 ± 157 (NNLO) | 2127607 | $2.650 \times 10^{-2}$ |
| TTjets | 165 ± 10 (NNLO) | 1165716 | $4.790 \times 10^{-3}$ |
| WW | 43 ± 1.5 (NLO) | 2061760 | $7.058 \times 10^{-4}$ |
| WZ | 18.2 ± 0.7 (NLO) | 2194752 | $2.806 \times 10^{-4}$ |
| ZZ | 5.9 ± 0.15 (NLO) | 2113368 | $9.447 \times 10^{-5}$ |
| Wjets | 10438 ± 900 (NNLO) | 5104514 | $6.920 \times 10^{-2}$ |
| QCD01 | $5.312 \times 10^{7}$ | 3264660 | 550.6 |
| QCD02 | $6.359 \times 10^{6}$ | 3191546 | 67.42 |
| QCD03 | $7.843 \times 10^{5}$ | 3208299 | 8.273 |
| QCD04 | $1.151 \times 10^{5}$ | 3045200 | 1.279 |
| QCD05 | 24260 | 3220080 | 0.2549 |
| QCD06 | 1168 | 3171240 | $1.246 \times 10^{-2}$ |
| QCD07 | 70.22 | 2019732 | $1.177 \times 10^{-3}$ |
| QCD08 | 15.55 | 1979055 | $2.659 \times 10^{-4}$ |
| QCD09 | 1.844 | 2084404 | $2.994 \times 10^{-5}$ |
| QCD10 | 0.3321 | 1086966 | $1.034 \times 10^{-5}$ |
| QCD11 | 0.01087 | 1021510 | $3.601 \times 10^{-7}$ |
| QCD12 | $3.575 \times 10^{-4}$ | 529360 | $2.285 \times 10^{-8}$ |

are also imposed. The criteria are summarized below.

- Electron $E_T > 20$ GeV.
- Electron $|\eta| < 1.442$ or $1.560 < |\eta| < 2.5$.
- Spikes in the ECAL are removed by applying the "swiss cross" cleaning. Let the energy of the central ECAL energy deposit be $e_1$, and let the sum of the energies in the four ECAL reconstructed hits above, below, to the left and to the right be $s_4$. Then the quantity $1 - s_4/e_1$ is required to be below 0.95.
- An electron is identified as being a conversion from a photon if a track within $\Delta R < 0.3$ of the electron can be found such that the two objects

are close together and have parallel trajectories. Photon conversions are rejected by applying the following criteria:

  - The distance between the points at which the electron and the second track would be parallel must be |Dist| > 0.02.
  - The difference between $\cot\theta_{track}$ and $\cot\theta_{ele}$ must be $|\Delta\cot\theta| > 0.02$.
  - The electron cannot have any missing expected hits in the tracker.

- For electrons in the barrel, define the combined relative isolation by

$$\text{RelIso} = \frac{(\text{Trk isolation} + \max(0, \text{ECAL isolation} - 1) + \text{HCAL isolation})}{\text{electron } p_T}, \tag{5.1}$$

  and for electrons in the endcap, define this quantity by

$$\text{RelIso} = \frac{(\text{Trk isolation} + \text{ECAL isolation} + \text{HCAL isolation})}{\text{electron } p_T}. \tag{5.2}$$

  Each individual isolation refers to the total energy deposited in the associated detector subsystem within $\Delta R < 0.3$ of the electron, other than the energy due to the electron itself. We require RelIso < 0.07 for the barrel and RelIso < 0.06 for the endcap

- Electron ID criteria are applied for the shape and track-cluster matching variables $\sigma_{i\eta i\eta}$, $\Delta\phi_{in}$, $\Delta\eta_{in}$ and hadronic fraction $H/E$ (recall definitions in Section 5.2.2). The upper limits imposed on barrel electrons and endcap electrons are listed in Table 5.5.

Any electron that satisfies all of the above criteria is called a good electron.

Table 5.5: Summary of Electron ID requirements. All values are upper limits.

| Variable | Barrel | Endcap |
|---|---|---|
| $\sigma_{i\eta i\eta}$ | 0.01 | 0.03 |
| $\Delta\phi_{in}$ | 0.06 | 0.03 |
| $\Delta\eta_{in}$ | 0.004 | 0.007 |
| $H/E$ | 0.04 | 0.025 |

### 5.2.3 Jet and $\not{E}_T$ Definitions

We use jets that are reconstructed from calorimeter towers using the anti-$k_T$ algorithm with $R = 0.5$ (AK5). The L2L3 corrections described in Section 2.5.6 are applied. The following kinematic requirements are imposed on the jets:

- Jet $p_T > 40$ GeV
- Jet $|\eta| < 3.0$
- The jet is not within $\Delta R < 0.3$ of any good electron

We use $\not{E}_T$ that has been calculated from the sum of the energy contributions from calorimeter towers, with jet and muon corrections applied.

### 5.2.4 Trigger and Event Selection

In data, we consider all those events that pass the following combination of triggers:

`HLT_Ele15_LW_L1R`

or `HLT_Ele15_SW_L1R`

or `HLT_Ele15_SW_CaloEleId_L1R`

or `HLT_Ele17_SW_CaloEleId_L1R`

or `HLT_Ele17_SW_TightEleId_L1R`

or `HLT_Ele17_SW_TighterEleIdIsol_L1R`

At least one of these triggers is not prescaled for every run that was analyzed. Therefore, the results correspond to the full luminosity of the electron-triggered primary datasets, which was given in Table 5.1 as 33.84 $pb^{-1}$.

The following event selection criteria are applied to the events that pass the trigger:

- The event must contain exactly two good electrons, as defined in Section 5.2.2.
- The event must contain at least two jets satisfying the requirements listed in Section 5.2.3.

Any such event is referred to as a selected event. When we search for the presence of a new physics signal, we will further restrict our attention to events with $\not{E}_T > 150$ GeV. Events that satisfy this additional requirement are called signal events.

## 5.3 Monte Carlo Backgrounds

Monte Carlo estimates are used for the background contributions due to Zjets, TTjets, and diboson events (WW, WZ and ZZ). The background due to Wjets events is not considered because no such event can contain two real electrons. Any Wjets event that passes the event selection criteria does so because of the

presence of a fake electron due to a jet. This is the same mechanism by which a QCD event can contribute to this channel. The background due to QCD and Wjets events is estimated using the electron fake rate method that will be described in the following chapter.

The results of applying the event selection criteria to the five Monte Carlo datasets are shown in Table 5.6, including the numbers of selected events and the numbers of signal events. When all selected events are considered, the Standard Model backgrounds are overwhelmingly dominated by Zjets events. In the signal region, TTjets events dominate. The total number of selected events from these backgrounds is 127.78 ± 1.72 (stat), and the total number of signal events is 0.785 ± 0.060 (stat).

Table 5.6 also shows the observations in data, which are 181 ± 13.5 (stat) selected events and 1 ± 1.0 (stat) signal events. The discrepancy between the data and Monte Carlo numbers will be addressed in Chapter 7.

Table 5.6: Monte Carlo estimates for Standard Model backgrounds, separated by process, in 33.84 $pb^{-1}$. The selected events are those with exactly two good electrons and at least two jets. The signal events also have $\not\!\!E_T > 150$ GeV. All uncertainties are statistical. The last line shows the observations from 33.84 $pb^{-1}$ of electron-triggered data.

| Name | Selected Events | Signal Events |
|---|---|---|
| Zjets | 108.46 ± 1.70 | 0. |
| TTjets | 16.76 ± 0.28 | 0.762 ± 0.060 |
| WW | 0.16 ± 0.01 | 0.011 ± 0.003 |
| WZ | 1.41 ± 0.02 | 0.008 ± 0.002 |
| ZZ | 0.99 ± 0.01 | 0.004 ± 0.001 |
| Total MC | 127.78 ± 1.72 | 0.785 ± 0.060 |
| Data | 181 ± 13.5 | 1 ± 1.0 |

The backgrounds due to these five processes must be combined with the

estimated background due to events that contain fake electrons. The latter contribution includes QCD and Wjets events, and is the subject of the next chapter. In Chapter 7, all of the backgrounds will be combined and subtracted from the observation in data to obtain the signal.

CHAPTER 6

# THE FAKE RATE

This chapter presents a method for estimating the background due to fake electrons that were produced by jets, where an electron is considered to be fake when it did not originate from a W, Z or $\tau$ decay. Such a fake electron can be created in a heavy quark decay and thrown clear of the jet so that it appears isolated, or it can be a jet that was erroneously reconstructed as an electron in the detector. The probability that any given jet will fake an electron is small, but the very large cross sections of processes such as QCD that are rich in jets can make the fake electron background a nontrivial contribution to electron-channel analyses.

The method that we employ was developed for use in model-independent SUSY searches in multi-electron channels, such as the one described in the previous chapter. Monte Carlo simulations of this technique have been performed to demonstrate its potential effectiveness [72], and the present study represents its first application to data. The study consists of several steps. First, the rate at which jets yield fake electrons is measured. Next, the measured fake rate is used to make testable predictions for the number of fake electrons in jet-triggered and photon-triggered datasets. Finally, it is applied to an electron-triggered dataset to calculate the expected number of events with two electrons, at least one of which is fake. The datasets, triggers, and analysis object definitions used for each of these steps are listed in Section 6.1.

The electron fake rate has to be measured in an environment that does not contain many real electrons. A jet-triggered dataset satisfies this requirement. However, the choice of jet trigger has an effect on the observed fake rate. A

procedure is demonstrated for suppressing trigger bias, and the fake rates measured on three different jet triggers are shown to yield compatible predictions. The accuracy of the predictions is tested by comparing them to the observed numbers of electrons in the three jet-triggered datasets. This is the topic of Section 6.2.

A photon-triggered dataset can also be used to test the fake rate. As in the jet-triggered case, the predicted number of fake electrons can be compared to the observed number of electrons in the sample. The fake rate prediction is shown to be reliable for several different photon triggers. The procedure and results are given in Section 6.3.

Finally, the fake rate is used to estimate the fake electron background in the multi-electron channel from the previous chapter. Results for 33.84 $pb^{-1}$ of electron-triggered data are shown in Section 6.4.

## 6.1 Datasets and Definitions

### 6.1.1 Datasets and Software

The events used in this analysis were obtained using the same JSON file as cited in Section 5.2.1, and therefore correspond to the same run number range, 132440 - 149442. All of the primary datasets that are used in the various steps of the analysis are listed in Table 6.1. The specific triggers and their effective luminosities are given in Table 6.2. Luminosities were calculated with the official luminosity calculation tool [67].

The data samples were analyzed using `CMSSW_3_8_6` and privately created

Table 6.1: Total luminosities for jet, photon and electron primary datasets.

| Jet-Triggered Dataset | Luminosity ($pb^{-1}$) |
|---|---|
| /JetMETTau/Run2010A-Nov4ReReco_v1/AOD | 0.167 |
| /JetMET/Run2010A-Nov4ReReco_v1/AOD | 2.89 |
| /Jet/Run2010B-PromptReco-v2/RECO | 30.38 |
| Total | 33.44 |
| **Photon-Triggered Dataset** | **Luminosity ($pb^{-1}$)** |
| /EG/Run2010A-Nov4ReReco_v1/AOD | 3.06 |
| /Photon/Run2010B-PromptReco-v2/AOD | 30.62 |
| Total | 33.68 |
| **Electron-Triggered Dataset** | **Luminosity ($pb^{-1}$)** |
| /EG/Run2010A-Nov4ReReco_v1/AOD | 3.06 |
| /Electron/Run2010B-PromptReco-v2/AOD | 30.78 |
| Total | 33.84 |

Table 6.2: Effective luminosities for jet and photon triggers.

| Abbreviation | Trigger | Effective Luminosity ($pb^{-1}$) |
|---|---|---|
| 30U | HLT_Jet30U | 0.308 |
| 50U | HLT_Jet50U | 3.30 |
| 70U | HLT_Jet70U | 6.68 |
| Ph10C | HLT_Photon10_Cleaned_L1R | $34.2 \times 10^{-3}$ |
| Ph15C | HLT_Photon15_Cleaned_L1R | 0.211 |
| Ph20C | HLT_Photon20_Cleaned_L1R | 2.73 |
| Ph30C | HLT_Photon30_Cleaned_L1R | 6.44 |
| Ph50C | HLT_Photon50_Cleaned_L1R | 10.8 |
| Ph70C | HLT_Photon70_Cleaned_L1R | 18.3 |

ntuples that are based on PAT objects. The official recommendations for good vertex and no scraping filters [68] were applied as described in Section 5.2.1.

### 6.1.2 Analysis Object Definitions

The good electron definition is the same as that listed in Section 5.2.2. We continue to use calorimeter $\not\!\!E_T$ with jet and muon corrections, and AK5 calorimeter jets with L2L3 corrections, as described in Section 5.2.3. However, a different set of selection requirements are imposed on the jets. In this context, the jets of interest are those that give rise to fake electrons that pass all of the good electron criteria. Therefore, the following kinematic requirements are imposed on the jets, based on the $p_T$ and $\eta$ requirements for good electrons:

- Jet $p_T > 25$ GeV.
- Jet $|\eta| < 1.442$ or $1.560 < |\eta| < 2.5$.

Any jet satisfying these criteria is referred to as a good jet.

When analyzing photon-triggered datasets, we require the presence of a good photon, which satisfies the following:

- Photon $E_T >$ photon trigger threshold.
- Photon hadronic fraction $< 0.05$.
- ECAL isolation $< 4.2 + 0.006 p_T$ and HCAL isolation $< 2.2 + 0.0025 p_T$, where $p_T$ is the transverse momentum of the photon. Each isolation represents the sum of the electromagnetic or hadron calorimeter reconstructed hits within $\Delta R < 0.4$ of the photon, excluding those due to the photon itself.
- The photon does not have a pixel seed.

The hadronic fraction and isolation requirements are the official recommendations from the Egamma Physics Object Group for identifying "isEM" photons

[73]. The additional requirement that the photon not have a pixel seed was found to be necessary to consistently reject electrons.

## 6.2 Measurement and Application of the Fake Rate

A two-dimensional fake rate is measured in bins of jet $p_T$ and $\eta$. In each bin, the fake rate is defined to be

$$r_i = \frac{\text{number of good jets in bin } i \text{ that were matched to fake electrons}}{\text{number of good jets in bin } i}. \quad (6.1)$$

A jet and an electron are matched when $\Delta R \equiv \sqrt{(\Delta\eta)^2 + (\Delta\phi)^2} < 0.1$. For convenience, the single index $i$ is taken to range over all bins.

To measure the fake rate, a sample of events is required in which the majority of good electrons are fake. A jet-triggered dataset serves this purpose. We compare results from three different jet triggers: `HLT_Jet30U`, `HLT_Jet50U` and `HLT_Jet70U`.

After it has been measured, the fake rate can be used to predict the number of fake electrons expected in a given jet-triggered dataset. This prediction can be compared to the number of good electrons that were observed. This is the first test of the accuracy of the fake rate method. In the following sections, we describe the procedures for measuring the fake rate and constructing the predictions.

### 6.2.1 Suppression of Real Electrons

Before the fake rate can be measured, there are two sources of bias that need to be suppressed. One is contamination from real electrons. To reduce such contamination, the following cleaning cuts are applied.

- Veto any event that contains more than one good electron. This suppresses real electrons from $Z \rightarrow ee$ decays.
- In events with exactly one good electron, calculate the combined transverse mass of the electron and the missing energy:

$$m_T = \sqrt{2 p_{T,ele} \not{E}_T \left[1 - \cos\left(\phi_{ele} - \phi_{\not{E}_T}\right)\right]}. \tag{6.2}$$

  Veto any event in which 50 GeV $< m_T <$ 100 GeV. This suppresses real electrons from $W \rightarrow e\nu$ decays.

- In events with exactly one good electron, search for a second electron that satisfies $E_T > 20$ GeV and $|\eta| < 1.442$ or $1.560 < |\eta| < 2.5$, and calculate the invariant mass of the vector sum of these two electrons:

$$m_{inv} = \sqrt{(E_1 + E_2)^2 - (p_{x1} + p_{x2})^2 - \left(p_{y1} + p_{y2}\right)^2 - (p_{z1} + p_{z2})^2}. \tag{6.3}$$

  Veto any event in which 71 GeV $< m_{inv} <$ 111 GeV. This suppresses real electrons from $Z \rightarrow ee$ decays in which one of the electrons is not fully reconstructed as a good electron.

The effectiveness of these cuts can be studied using the Monte Carlo datasets listed in Tables 5.2 and 5.3. Because the Monte Carlo files contain no trigger information, the `HLT_Jet30U` trigger is simulated by requiring all events to contain at least one jet whose uncorrected $p_T$ is above 30 GeV. The `50U` and `70U`

triggers are simulated in the same manner. The Monte Carlo results are scaled to the effective luminosities for each of these triggers, as listed in Table 6.2

Figure 6.1 shows the transverse mass of the good electron plus missing energy in events from the Wjets dataset. The electron is required to be real, and its mother particle is required to be a W boson. Figure 6.2 shows the invariant mass of one good electron plus a second loosely defined electron from the Zjets dataset, where the good electron is required to be real and its mother particle is required to be a Z boson. Based on these plots, the proposed restrictions should remove the majority of real electrons from $W \to e\nu$ and $Z \to ee$ decays.

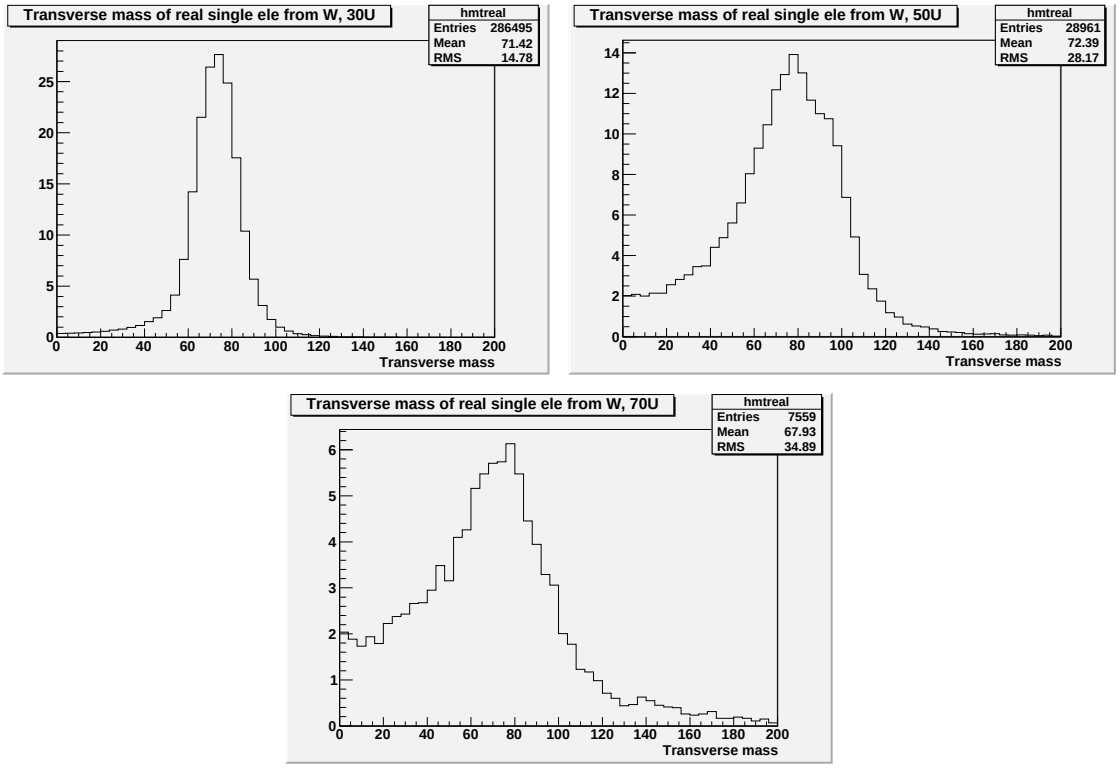


Figure 6.1: Distributions of the transverse mass of the good electron plus missing energy in events from the Wjets dataset, where the electron is required to be real and to have originated from a W boson. The plots are constructed for the `30U` (top left), `50U` (top right) and `70U` (bottom) jet triggers. In all cases, the majority of such events have a transverse mass value within (50 GeV, 100 GeV).

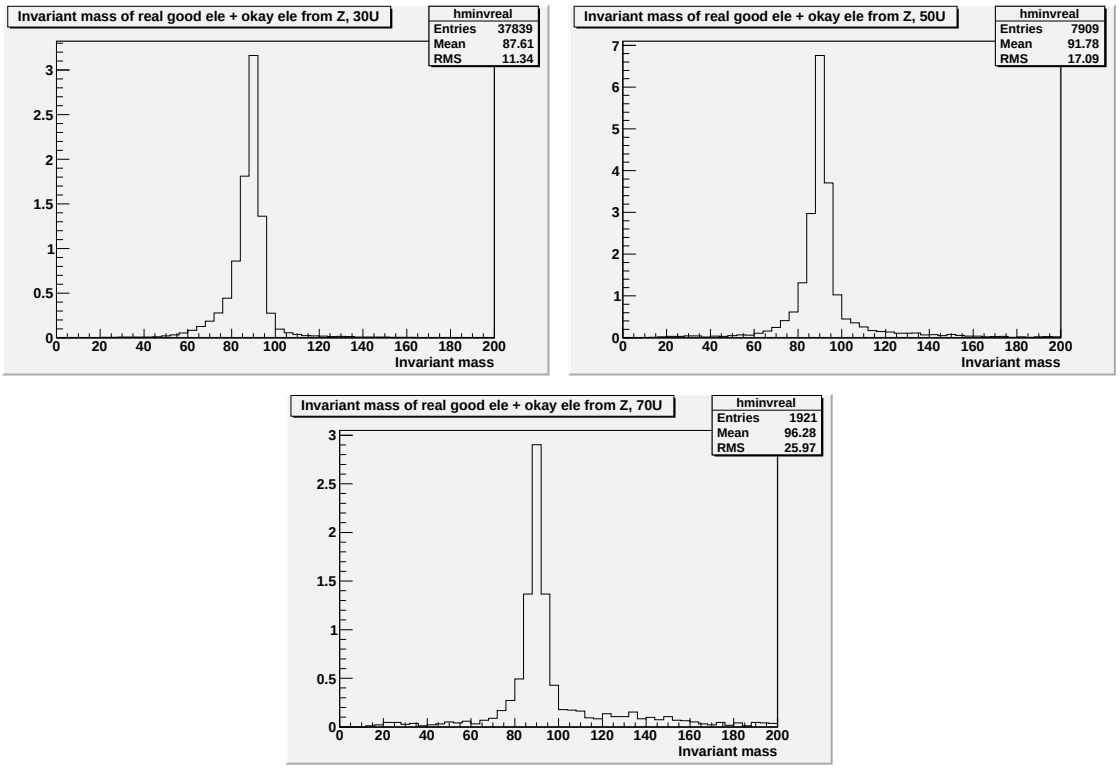


Figure 6.2: Distributions of the invariant mass of the good electron plus second electron in events from the Zjets dataset, where the good electron is required to be real and to have originated from a Z boson. The plots are constructed for the `30U` (top left), `50U` (top right) and `70U` (bottom) jet triggers. In all cases, the majority of such events have an invariant mass value within (71 GeV, 111 GeV).

The fake rate is now measured on all of the Monte Carlo files. The measurement procedure includes the trigger bias veto that will be described in the next section. Table 6.3 shows the contributions to the numerator of the fake rate from the different datasets. These values have been summed over all of the jet $p_T$ and $\eta$ bins. The real electron backgrounds due to diboson events, which are not listed, are negligible compared to the others. Further widening of the W and Z mass windows has almost no impact on the real electron contributions.

The results suggest that real electrons still constitute up to 43% of the electrons that are used to calculate the fake rate. However, when we measure the

fake rate on data in Section 6.2.3, we will find that the total numerators are larger than predicted; that is, the QCD contribution is underestimated by simulation and therefore the real electron contamination is not quite as large as this. Also, comparisons between predicted and observed numbers of fake electrons will suggest that the fake rate is not suffering any deleterious effects from the real electrons that remain.

Table 6.3: Contributions to the numerator of the fake rate from Monte Carlo datasets. The non-QCD values represent real electrons. The final set of values for all Monte Carlo show all real and fake electrons, including the very small numbers of fake electrons from the non-QCD files. All uncertainties are statistical.

| Dataset | Jet trigger | Numerator contribution |
|---|---|---|
| Zjets | 30U | 3.62 ± 0.03 |
| (real electrons) | 50U | 18.9 ± 0.2 |
| | 70U | 7.2 ± 0.2 |
| Wjets | 30U | 3.68 ± 0.05 |
| (real electrons) | 50U | 24.1 ± 0.4 |
| | 70U | 28.3 ± 0.6 |
| TTjets | 30U | 0.967 ± 0.006 |
| (real electrons) | 50U | 7.08 ± 0.06 |
| | 70U | 9.9 ± 0.1 |
| All non-QCD | 30U | 8.34 ± 0.05 |
| (real electrons) | 50U | 50.6 ± 0.4 |
| | 70U | 45.9 ± 0.6 |
| All QCD | 30U | 15.6 ± 5.5 |
| | 50U | 77.7 ± 18.8 |
| | 70U | 80.3 ± 23.8 |
| All MC | 30U | 24.2 ± 5.5 |
| | 50U | 129.6 ± 18.8 |
| | 70U | 127.4 ± 23.8 |

### 6.2.2 Jet Trigger Bias

The fake rate is measured on events that pass a specific jet trigger. All of these events contain at least one jet whose uncorrected $p_T$ is above a certain threshold. This requirement artificially inflates the jet $p_T$ spectrum near the corrected $p_T$ value that corresponds to the trigger threshold, as shown in Figure 6.3. The $p_T$ spectrum for jets that yield fake electrons is also inflated in this region, as shown in Figure 6.4. Because the trigger favors certain jets, the observed fake rate contains an inherent trigger bias.

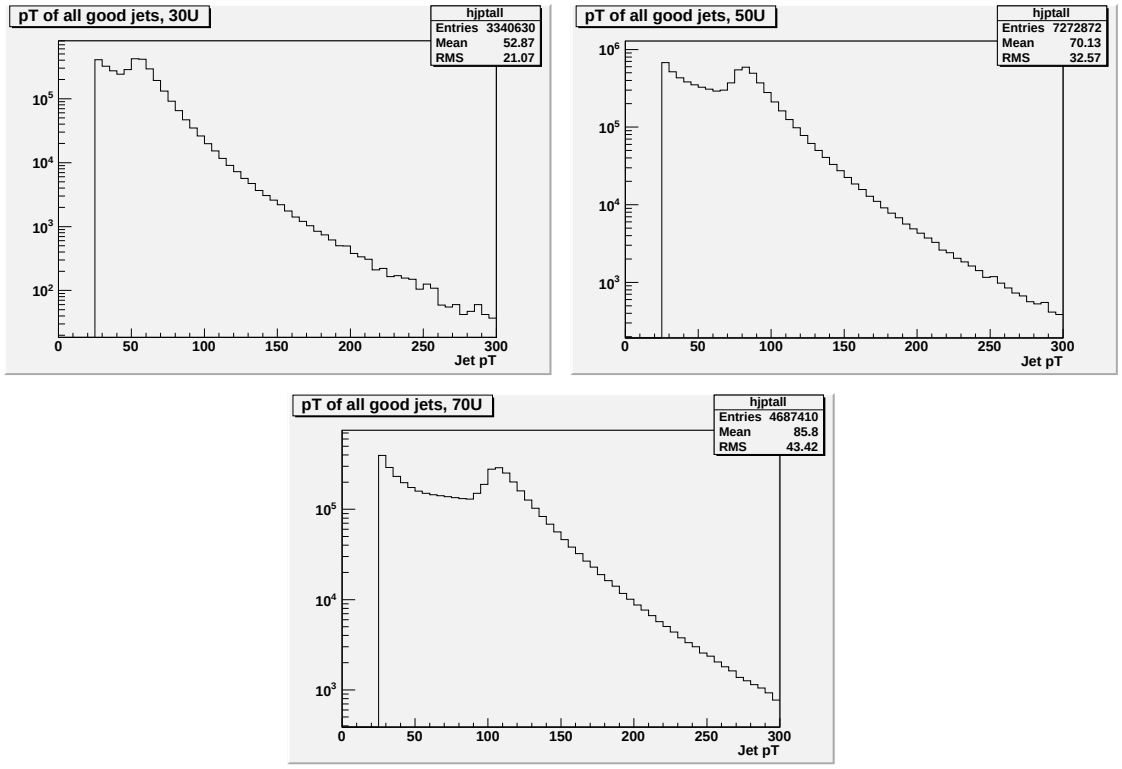


Figure 6.3: Distributions of the $p_T$ values for all good jets. Note the secondary peak that appears at a different position for each trigger.

To eliminate the bias, the jets that occur disproportionately often because of the trigger threshold must be vetoed. When designing the veto, we take into account the fact that most QCD events are dijet events: that is, the leading and

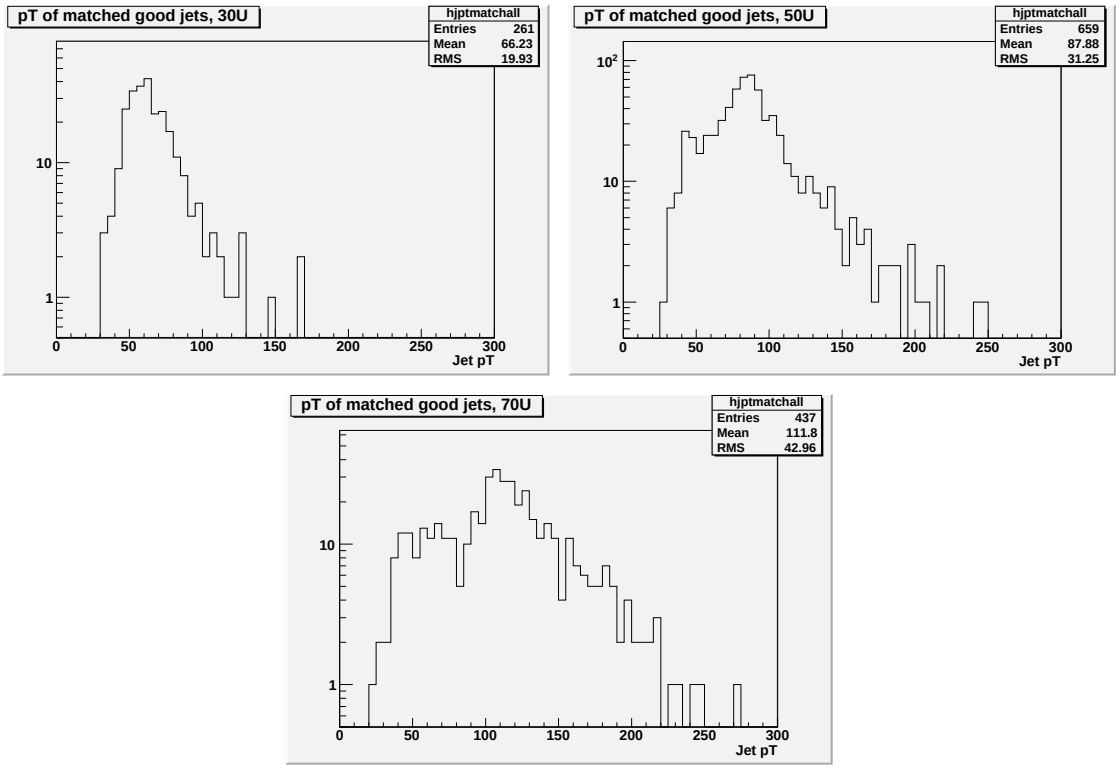


Figure 6.4: Distributions of the $p_T$ values for good jets that are matched to good electrons. The location of the maximum corresponds to the secondary peak from the previous figure.

second leading jets are correlated. Thus, the trigger bias veto is as listed below.

- If the uncorrected $p_T$ of the leading jet is above the trigger threshold but that of the second leading jet is not, veto the leading jet.
- If the uncorrected $p_T$ values of the leading and second leading jets are both above the trigger threshold, but that of the third jet is not, veto the top two jets.

All other jets are retained. The effect of this procedure on the jet $p_T$ spectra is shown in Figures 6.5 and 6.6. In the $p_T$ distributions for all good jets, there is no longer an excess around the trigger threshold. The corresponding peak in the

distributions for the matched jets is also reduced.

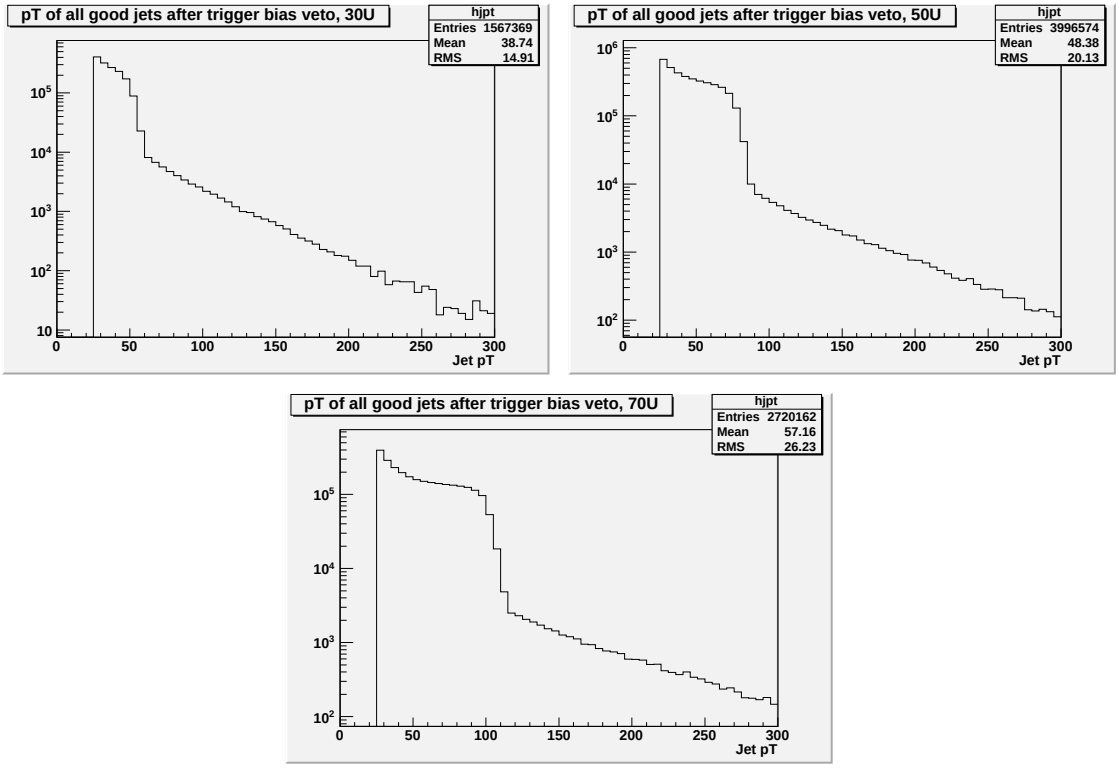


Figure 6.5: Distributions of the $p_T$ values for all good jets, after the trigger bias veto has been applied. The secondary peak that was seen in Figure 6.3 has been removed.

### 6.2.3 Measuring the Fake Rate

After these restrictions have been applied, the remaining good jets and good electrons are used to measure the fake rate in bins of jet $p_T$ and $\eta$. The statistical uncertainty can be calculated at the same time. Write the fake rate in the $i$th bin as

$$r_i = \frac{p_i}{p_i + f_i}, \tag{6.4}$$

where $p_i$ is the number of matched jets in this bin and $f_i$ is the number of unmatched jets. The counts $p_i$ and $f_i$ are assumed to have Poisson uncertainties:

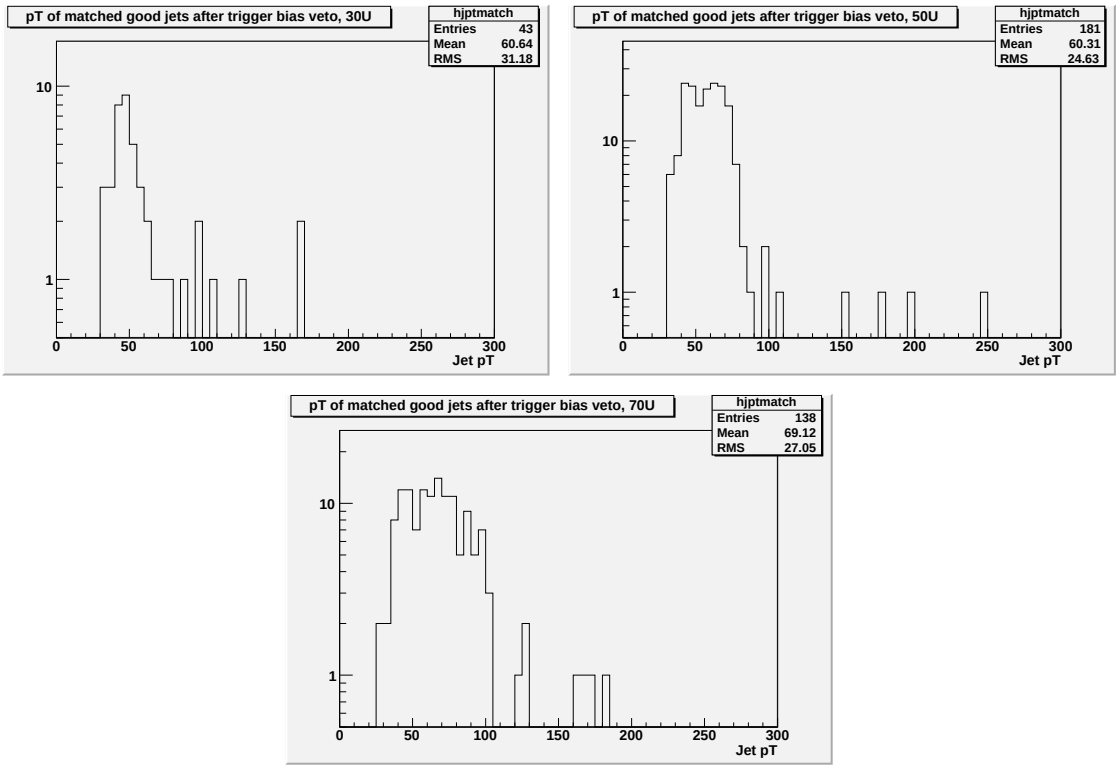


Figure 6.6: Distributions of the $p_T$ values for good jets that are matched to good electrons, after the trigger bias veto has been applied. The peaks associated with the jet trigger thresholds have been suppressed.

that is, $\mathrm{Var}(p_i) = p_i$ and $\mathrm{Var}(f_i) = f_i$. Note that $p_i$ and $f_i$ are independent, since each jet can only contribute to one of them. Then the variance of $r_i$ is given by

$$\mathrm{Var}(r_i) \approx \left(\frac{\partial r_i}{\partial p_i}\right)^2 \mathrm{Var}(p_i) + \left(\frac{\partial r_i}{\partial f_i}\right)^2 \mathrm{Var}(f_i) = \frac{1}{(p_i + f_i)^2}\left[(1 - r_i)^2\, p_i + r_i^2 f_i\right]. \qquad (6.5)$$

This expression is used to construct the error bars shown on plots of the fake rate.

Plots overlaying results from the three jet triggers are shown in Figure 6.7. Because some of the bins are sparsely populated, the fake rates plotted in each $p_T$ bin are summed over all $\eta$ values in order to yield reasonable error bars, and likewise the fake rates plotted in each $\eta$ bin are summed over all $p_T$ values. The summation is for visualization purposes only; all subsequent calculations

are performed using a fully two-dimensional fake rate. Most bins show good agreement between the fake rates.

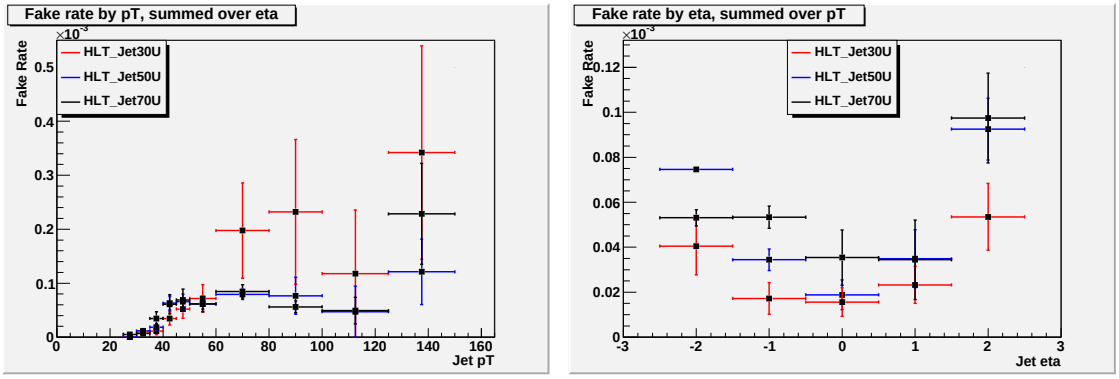


Figure 6.7: Comparisons of the fake rates measured on the three jet-triggered datasets. The majority of the bins agree to within statistical uncertainty.

In Section 6.2.1, we used the Standard Model Monte Carlo datasets to estimate the contamination due to real electrons in the measurement of the fake rate. Table 6.4 compares the numbers of real electrons from the Zjets, Wjets and TTjets datasets to the total number of electrons in data that contributed to the numerator of the fake rate. The simulations predict that up to 34% of the total numerator consists of real electrons. This is lower than the percentage calculated using the Monte Carlo QCD files.

### 6.2.4 Systematic Uncertainty Due to Jet Energy Scale

Even after jet energy corrections have been applied, there can still be a significant uncertainty associated with the absolute energy scale for reconstructed jets. Since the fake rate measurement depends on the observed jet $p_T$ values, we would like to determine its robustness with respect to changes to the jet energy scale.

Table 6.4: Contributions to the numerator of the fake rate from real electrons in the non-QCD Monte Carlo datasets, compared to the total numerators observed in data. The predicted real electron contamination is up to 34% of the total. All uncertainties are statistical.

| Dataset | Jet trigger | Numerator contribution |
|---|---|---|
| Zjets | 30U | 3.62 ± 0.03 |
| (real electrons) | 50U | 18.9 ± 0.2 |
| | 70U | 7.2 ± 0.2 |
| Wjets | 30U | 3.68 ± 0.05 |
| (real electrons) | 50U | 24.1 ± 0.4 |
| | 70U | 28.3 ± 0.6 |
| TTjets | 30U | 0.967 ± 0.006 |
| (real electrons) | 50U | 7.08 ± 0.06 |
| | 70U | 9.9 ± 0.1 |
| All non-QCD | 30U | 8.34 ± 0.05 |
| (real electrons) | 50U | 50.6 ± 0.4 |
| | 70U | 45.9 ± 0.6 |
| Jet-triggered | 30U | 43 ± 6.6 |
| data | 50U | 176 ± 13.3 |
| | 70U | 134 ± 11.6 |

The jet energy scale uncertainty is taken to be 10% [34]. To assess the corresponding systematic uncertainty in the fake rate, the above procedure for calculating the fake rate is repeated twice, once after scaling all jet $p_T$ values by a factor of 0.9, and again after scaling them by a factor of 1.1. If the original fake rate in bin $i$ is $r_i$, and if the values observed after applying the scale are $r_i^{0.9}$ and $r_i^{1.1}$, then the systematic uncertainty assigned to $r_i$ is the larger of $\left|r_i - r_i^{0.9}\right|$ and $\left|r_i - r_i^{1.1}\right|$.

The systematic uncertainties are found to be up to twice the size of the statistical uncertainties. This suggests that the fake rate measurement is dependent on the jet energy scale, though not overwhelmingly so. The overlay plots of the fake rates from the three jet triggers are repeated in Figure 6.8 with the error bars recalculated to include statistical and systematic uncertainties. When

predictions are calculated using the fake rate, both the statistical and systematic uncertainties will be propagated.

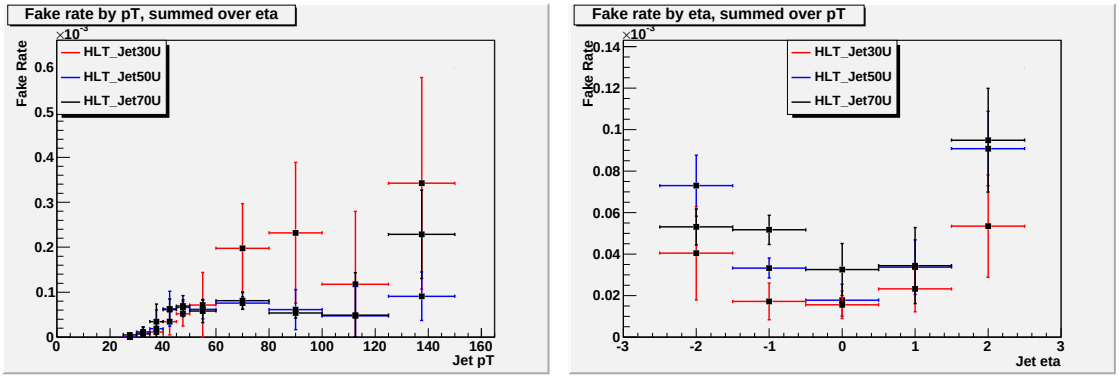


Figure 6.8: Comparisons of the fake rates measured on the three jet-triggered datasets, where the error bars include the statistical uncertainty and the systematic uncertainty due to jet energy scale.

### 6.2.5 Constructing Predictions

The purpose of measuring the fake rate is to predict the number of events within a given sample that contain fake electrons. In a jet-triggered sample, once the cuts to suppress real electrons have been applied, all of the observed good electrons are presumably fake. We therefore use the fake rate to construct the predicted number of events with one fake electron, and compare it to the observed number of electrons in the dataset.

Fix an event, and assign it the label $a$. Suppose this event has $n_a$ jets, and suppose that the $k$th jet falls into the $i_k$th fake rate bin. Then the probability that the $k$th jet produces a fake electron is $r_{i_k}$. The probability that event $a$ contains zero fake electrons is

$$P_a(0) = \prod_{k=1}^{n_a} (1 - r_{i_k}), \tag{6.6}$$

and the probability that it contains exactly one fake electron is

$$P_a(1) = \sum_{j=1}^{n_a} r_{i_j} \prod_{k \neq j} (1 - r_{i_k}) \,. \tag{6.7}$$

Define the weight of event $a$ to be

$$W_a = \frac{P_a(1)}{P_a(0)}. \tag{6.8}$$

Suppose event $a$ is found to contain zero fake electrons. Then it corresponds to the fraction $W_a$ of an event with the same kinematic properties, and one fake electron.

More generally, suppose we assemble a parent sample of events with some fixed number $R$ of real electrons, and no fakes. We can construct a sample with $R$ real electrons and one fake by weighting each parent event by its associated $W_a$. In the case of the jet-triggered datasets, the parent sample consists of events with zero electrons. Weighting these events yields the prediction for events with zero real electrons and one fake. The total number of predicted fake electron events is given by summing $W_a$ over the parent sample.

Notice that we can write

$$W_a = \frac{\sum_{j=1}^{n_a} r_{i_j} \prod_{k \neq j} (1 - r_{i_k})}{\prod_{k=1}^{n_a} (1 - r_{i_k})} = \sum_{j=1}^{n_a} \frac{r_{i_j}}{1 - r_{i_j}}. \tag{6.9}$$

If there are $N_0$ events in the parent sample, then the predicted number of fake electron events, $N_1$, is given by

$$N_1 = \sum_{a=1}^{N_0} W_a = \sum_{a=1}^{N_0} \sum_{j=1}^{n_a} \frac{r_{i_j}}{1 - r_{i_j}}. \tag{6.10}$$

In other words, $N_1$ is the sum of the expression $\dfrac{r_{i_j}}{1 - r_{i_j}}$ over all good jets in all events in the parent sample. The end result will have the form

$$N_1 = \sum_i m_i \frac{r_i}{1 - r_i}, \tag{6.11}$$

where $i$ ranges over all of the fake rate bins, and $m_i$ is the total number of good jets in the parent sample that fall into the $i$th bin. A sum over events has been reduced to a sum over fake rate bins, where each parent sample jet in bin $i$ represents the fraction $\frac{r_i}{1-r_i}$ of a jet that yielded a fake electron.

Writing the prediction in this form allows us to calculate its statistical uncertainty. First, observe that the fake rates $r_i$ from different bins are independent from each other, as are the jet counts $m_i$. To ensure that the jet counts are independent from the fake rates, the jet-triggered dataset is split in half. The fake rate is measured on even-numbered events, and the good jets per bin are counted on the odd-numbered events. The prediction that is constructed from these numbers therefore applies to the odd-numbered sample. Each count $m_i$ is assumed to have a Poisson statistical uncertainty, so $\mathrm{Var}(m_i) = m_i$. The variance of $r_i$ is the sum in quadrature of the statistical uncertainty from Equation 6.5 and the systematic uncertainty due to jet energy scale from Section 6.2.4. In terms of these quantities, the variance of $N_1$ is

$$\mathrm{Var}\,(N_1) = \sum_i \mathrm{Var}\left(m_i \frac{r_i}{1-r_i}\right) = \sum_i \left[\left(\frac{r_i}{1-r_i}\right)^2 m_i + \frac{m_i^2}{(1-r_i)^4}\mathrm{Var}(r_i)\right]. \tag{6.12}$$

This expression is the source of the uncertainties that are listed with all fake rate predictions.

We also need to count the observed number of fake electrons in the odd-numbered sample. Real electrons are suppressed using the same cleaning cuts as described in Section 6.2.3. Any good electron that remains is assumed to be fake. The observed number of fake electrons in the `HLT_Jet30U` dataset can be compared to the predictions from the fake rates that were measured on the `30U`, `50U` and `70U` datasets. The same is true of the observed numbers in the `50U` and `70U` datasets.

The observed and predicted numbers of fake electron events are listed in Table 6.5. The three different fake rates yield predictions on the same dataset that agree with each other to within less than 1.2 standard deviations. However, a number of the predictions underestimate the observed number of fake electrons by up to 1.5 standard deviations. Were it not for the large systematic uncertainty due to jet energy scale, the discrepancy would be as large as 2.1 standard deviations. To explain this phenomenon, recall the discussion of trigger bias from Section 6.2.3. The purpose of applying the trigger bias veto is to combat the dependence of the fake rate on the jet trigger threshold. Therefore, we might expect that the fake rate measured after the veto is not the same as the effective fake rate in the original dataset. This would explain why the fake rate prediction sometimes misrepresents the observed number of fake electrons in a jet-triggered dataset.

Table 6.5: Observed and predicted numbers of fake electrons in jet-triggered datasets. The predictions from the three fake rates agree with each other to within less than 1.2 standard deviations.

| | HLT_Jet30U | HLT_Jet50U |
|---|---|---|
| observed | 223 ± 14.9 (stat) | 577 ± 24.0 (stat) |
| pred. 30U | 284.6 ± 71.8 (stat) ± 95.1 (sys) | 1006 ± 290 (stat) ± 311 (sys) |
| pred. 50U | 169.2 ± 13.8 (stat) ± 21.1 (sys) | 385.9 ± 63.8 (stat) ± 87.7 (sys) |
| pred. 70U | 177.4 ± 17.4 (stat) ± 27.8 (sys) | 447.2 ± 50.8 (stat) ± 67.6 (sys) |
| | HLT_Jet70U | |
| observed | 430 ± 20.7 (stat) | |
| pred. 30U | 674.3 ± 217.0 (stat) ± 336.5 (sys) | |
| pred. 50U | 246.6 ± 65.9 (stat) ± 82.9 (sys) | |
| pred. 70U | 370.4 ± 82.0 (stat) ± 108.4 (sys) | |

To test this hypothesis, we also apply the trigger bias veto procedure when calculating the predictions. While counting $m_i$, the good jets per bin in the parent sample, we veto any jet that fits one of the veto conditions. Similarly, when

counting the observed fake electrons, we veto any electron if it is matched to a jet that fits one of the veto conditions. A comparison between predicted and observed fake electron counts under these new conditions is shown in Table 6.6. The three predictions continue to show good agreement with each other. In addition, the agreement between prediction and observation is much improved. For the remainder of the jet-triggered results, the trigger bias veto will also be applied to the parent sample and the observed electrons.

Table 6.6: Observed and predicted numbers of fake electrons in jet-triggered datasets when the trigger bias veto is also applied to the parent sample and the observed counts. The three predictions still agree with each other to within less than 1.2 standard deviations. In addition, the predictions agree with the observed counts to within less than 1.0 standard deviations.

| | HLT_Jet30U | HLT_Jet50U |
|---|---|---|
| observed | 43 ± 6.6 (stat) | 173 ± 13.2 (stat) |
| pred. 30U | 43.1 ± 6.6 (stat) ± 8.8 (sys) | 285.4 ± 79.4 (stat) ± 76.3 (sys) |
| pred. 50U | 45.7 ± 4.7 (stat) ± 8.3 (sys) | 176.3 ± 13.3 (stat) ± 19.4 (sys) |
| pred. 70U | 52.1 ± 6.9 (stat) ± 11.7 (sys) | 191.7 ± 18.5 (stat) ± 26.7 (sys) |
| | HLT_Jet70U | |
| observed | 159 ± 12.6 (stat) | |
| pred. 30U | 278.9 ± 80.3 (stat) ± 73.1 (sys) | |
| pred. 50U | 124.8 ± 15.4 (stat) ± 20.5 (sys) | |
| pred. 70U | 133.6 ± 11.5 (stat) ± 15.6 (sys) | |

### 6.2.6 Predicting $\not\!\!E_T$ and Fake Electron $p_T$ Distributions

In addition to predicting event counts, the fake rate can be used to predict the distributions for kinematic quantities associated with fake electron events. For example, suppose we want to predict the number of fake electron events whose $\not\!\!E_T$ is within a certain range. This is accomplished by simply restricting the parent sample events to those with a $\not\!\!E_T$ value within the desired range. In this

fashion, a prediction for the $\not\!\!E_T$ distribution due to fake electron events can be constructed one $\not\!\!E_T$ bin at a time. This technique will be used to obtain the prediction for fake electron events in the signal region of the multi-electron channel.

Using the fake rates measured in the previous section, we apply this procedure to events from the `HLT_Jet30U`, `HLT_Jet50U` and `HLT_Jet70U` triggers. For each trigger, the predicted $\not\!\!E_T$ distributions can be compared to the observed $\not\!\!E_T$ distribution from fake electron events. Figure 6.9 shows these comparisons. As with the event counts, the three predictions show good agreement with each other. Though the fake rate tends to underestimate the high-$\not\!\!E_T$ region, many bins are correct to within about two standard deviations.

We can also use the fake rate to predict the $p_T$ distribution of the fake electrons. This is a more complicated procedure because the reconstructed $p_T$ of a fake electron depends on, but is not equal to, the $p_T$ of the jet that produced it. This introduces another systematic uncertainty into the predicted electron $p_T$ distribution, in addition to the statistical and systematic uncertainties already associated with the fake rate.

This systematic uncertainty in fake electron $p_T$ can be measured at the same time as the fake rate. Figure 6.10 shows a scatter plot of the $p_T$ of a fake electron versus the $p_T$ of the jet to which it was matched. Within each jet $p_T$ bin, as defined by the fake rate binning, the observed electron $p_T$ values form a distribution. The mean of this distribution is the estimate for the fake electron $p_T$ due to a jet in this bin, and the standard deviation is the associated systematic uncertainty. The means and standard deviations are shown in Figure 6.10, superimposed on the scatter plot. The horizontal bar represents the width of the fake rate bin, while the position and height of the vertical bar are obtained from

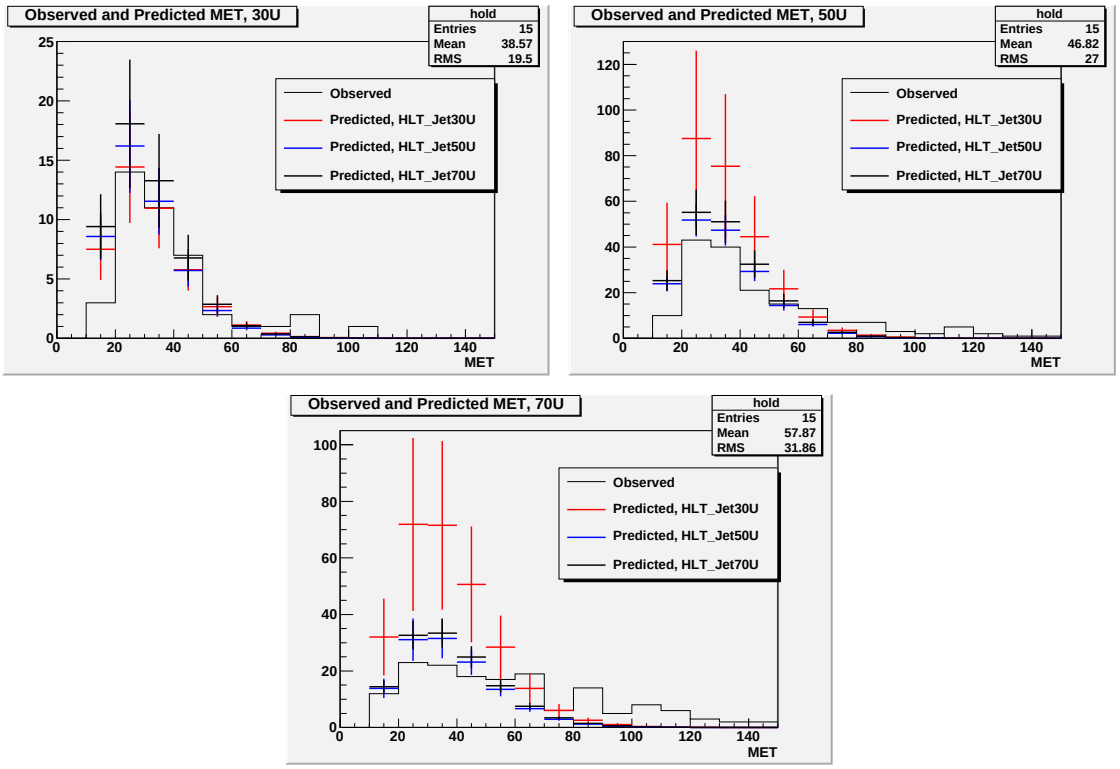


Figure 6.9: Comparison between observed and predicted $\not\!\!E_T$ distributions for fake electron events in jet-triggered datasets. There is reasonable agreement between the shapes of the observed and predicted distributions, and the predictions in many of the bins agree with observation to within one or two standard deviations.

the electron $p_T$ distribution in that bin.

To propagate all of the statistical and systematic uncertainties, we construct a toy Monte Carlo simulation. The following inputs are required for each bin:

- $r_i$, the measured fake rate, and its associated uncertainty, which is the sum in quadrature of the statistical uncertainty as calculated in Section 6.2.3 and the systematic uncertainty due to jet energy scale as calculated in Section 6.2.4.
- $m_i$, the number of jets in the parent sample that fall within bin $i$. These

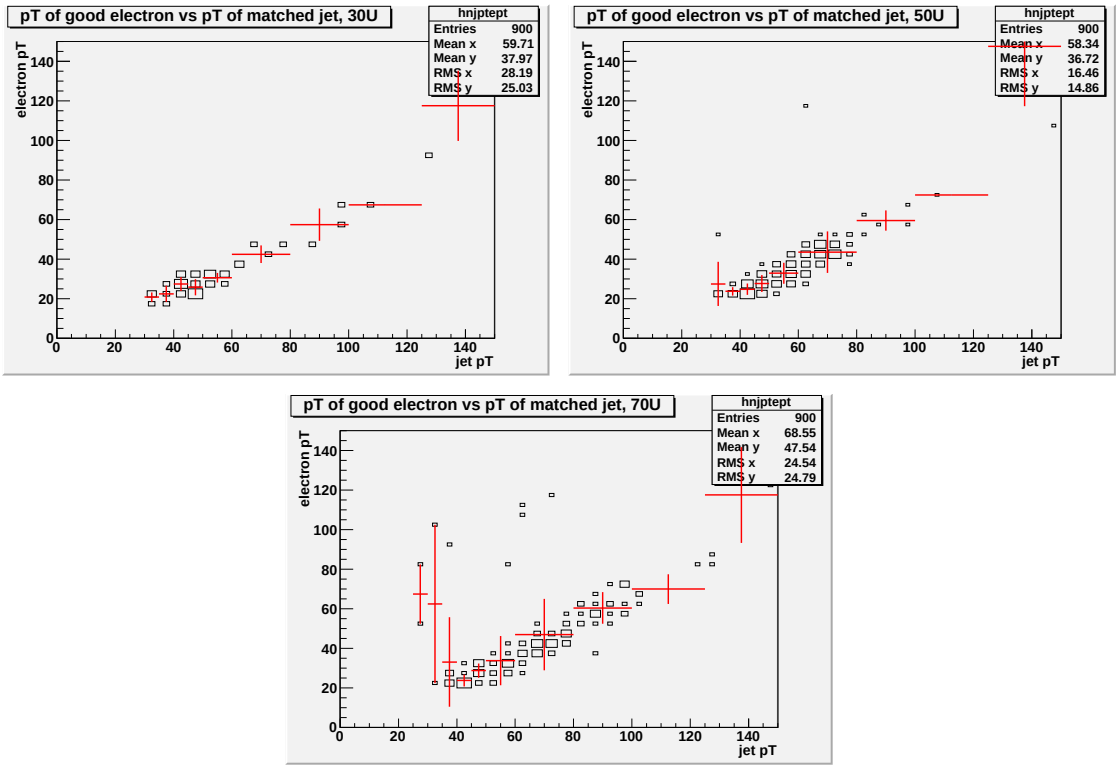


Figure 6.10: Representation of the distribution of electron $p_T$ values associated with each jet $p_T$ bin. The horizontal bar represents the width of the $p_T$ bin, while the position and height of the vertical bar represent the mean and standard deviation of the electron $p_T$ distribution in this bin.

values are assumed to have Poisson statistical uncertainties.

- $e_i$, the average electron $p_T$ value associated with the jet $p_T$ range for bin $i$. Its systematic uncertainty is the observed standard deviation of the electron $p_T$ distribution associated with this bin.

For each input, the observed value and associated uncertainty are used to construct a probability distribution for the expected value of this variable. Then the uncertainties can be propagated by sampling randomly from these distributions and averaging over many trials.

More specifically, we choose to model the inputs using Gamma distributions,

which have the general form

$$P(\lambda) = \frac{\lambda^{\alpha-1} e^{-\lambda/\beta}}{\beta^{\alpha}\Gamma(\alpha)}. \tag{6.13}$$

The mean of this distribution is $\alpha\beta$, and the variance is $\alpha\beta^2$, so the parameters $\alpha$ and $\beta$ can always be chosen such that the mean is the observed value of the input and the standard deviation is its uncertainty. We use Gamma distributions because they are almost indistinguishable from normal distributions when the standard deviation is small relative to the mean, but they are also constrained to be nonnegative. This is appropriate because all of the input variables are nonnegative quantities.

Having constructed the Gamma distributions, we can now perform the Monte Carlo simulation to predict the fake electron $p_T$ distribution. The outcome of each iteration of the simulation is an electron $p_T$ histogram, which we choose to bin in widths of 5 GeV. An iteration proceeds as follows:

- In each fake rate bin, draw random values for $m_i$ and $r_i$ from their associated distributions. These values constitute the fake rate and the jet content of the parent sample for this trial.
- As we argued in Section 6.2.5, each parent sample jet in bin $i$ represents the fraction $\frac{r_i}{1-r_i}$ of a jet that yielded a fake electron. In this iteration, there are $m_i$ such jets. Therefore, we multiply the distribution for $e_i$ by the number of jets $m_i$, then add it to the fake electron $p_T$ histogram with weight $\frac{r_i}{1-r_i}$.

At the end of the simulation, take the mean and standard deviation of the simulated entries within each electron $p_T$ bin. The final output is a histogram whose bins contain these mean values, and whose assigned uncertainties are the standard deviations.

Using this procedure, we compare results from the three measured fake rates. The predictions are superimposed on the observed fake electron $p_T$ distributions in Figure 6.11. There is reasonable agreement among the predictions, and between prediction and observation.

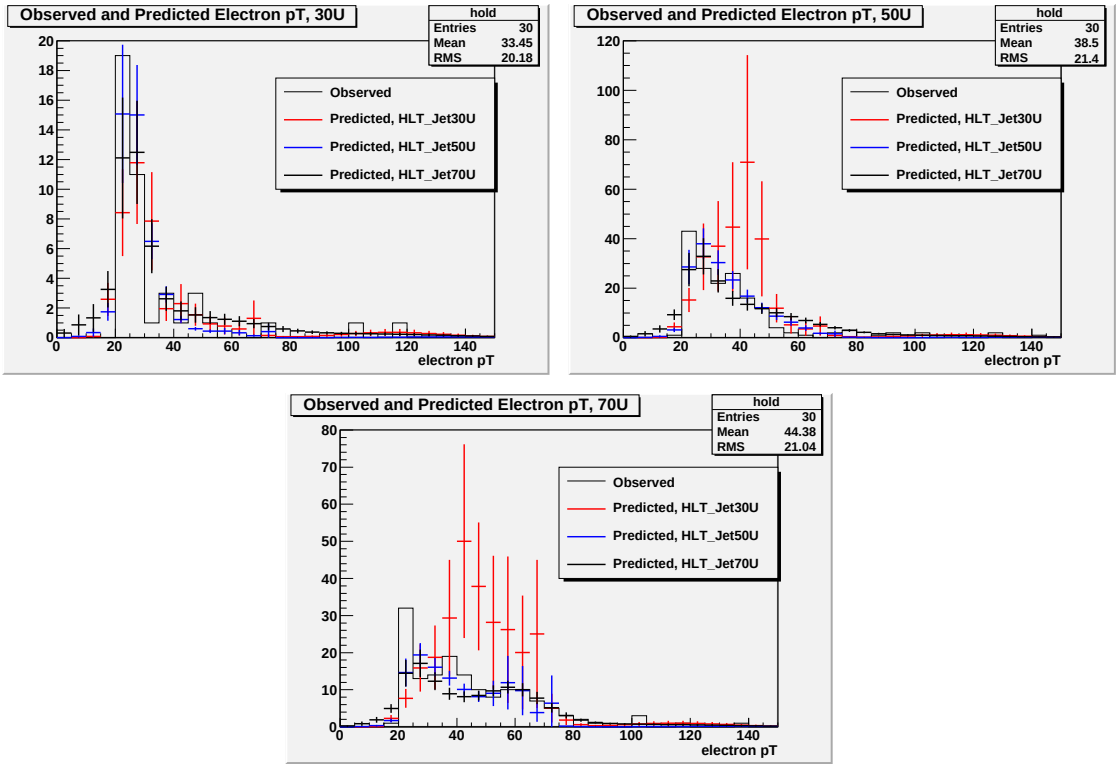


Figure 6.11: Comparison between observed and predicted $p_T$ distributions for fake electrons in jet-triggered datasets. All three predictions are reasonably successful at modeling the features of the observed distributions.

## 6.3 Test Environment: Photon Triggers

The above studies are a good first indication that this procedure yields a fake rate that gives reliable predictions. However, the fake rate should also be tested outside of the jet-triggered environment. To accomplish this, fake electron pre-

dictions are constructed for the six photon-triggered datasets that were listed in Table 6.2. Photon-triggered datasets are not expected to contain many real electrons, so the predictions can be compared to the observed fake electron counts and distributions.

The first step is to assemble a parent sample of events that do not contain any good electrons. Now that there is no jet trigger, there is no need to apply the trigger bias veto procedure. Instead, the parent sample events are required to contain at least one good photon above the threshold of the photon trigger. The fake rate is applied to the parent sample as described in Section 6.2.5. The result is the predicted number of events containing one fake electron.

When counting the observed number of electrons, the cleaning cuts to eliminate real electrons from Z and W decays are applied as described in Section 6.2.3. Fake electron events are also required to contain at least one good photon above the photon trigger threshold. Any electron that is observed under these conditions is assumed to be a fake electron that originated from a jet.

The observed counts are compared to the predictions in Table 6.7. For all six photon datasets, there is agreement to within less than 1.4 standard deviations between prediction and observation.

Using the methods described in Section 6.2.6, we can also construct the predicted $\not\!\!E_T$ distribution for fake electron events, and the predicted fake electron $p_T$ distributions. The $\not\!\!E_T$ distributions are shown in Figure 6.12, and the electron $p_T$ distributions are shown in Figure 6.13. In all cases, the three predictions are quite successful at modeling the features of the observed distributions.

Table 6.7: Observed and predicted numbers of fake electron events in photon-triggered datasets. The accuracy of the predictions is comparable to that observed in the jet-triggered cases.

| | HLT_Photon10 | HLT_Photon15 |
|---|---|---|
| observed | 5 ± 2.2 (stat) | 24 ± 4.9 (stat) |
| pred. 30U | 3.7 ± 0.6 (stat) ± 0.7 (sys) | 21.8 ± 3.7 (stat) ± 4.5 (sys) |
| pred. 50U | 3.6 ± 0.4 (stat) ± 0.7 (sys) | 23.2 ± 2.5 (stat) ± 4.8 (sys) |
| pred. 70U | 4.1 ± 0.6 (stat) ± 0.9 (sys) | 25.4 ± 3.6 (stat) ± 6.9 (sys) |
| | HLT_Photon20 | HLT_Photon30 |
| observed | 167 ± 12.9 (stat) | 123 ± 11.1 (stat) |
| pred. 30U | 184.7 ± 32.7 (stat) ± 41.4 (sys) | 163.3 ± 45.4 (stat) ± 44.7 (sys) |
| pred. 50U | 174.2 ± 16.4 (stat) ± 27.4 (sys) | 92.2 ± 7.7 (stat) ± 11.2 (sys) |
| pred. 70U | 185.2 ± 23.2 (stat) ± 38.2 (sys) | 93.3 ± 9.4 (stat) ± 12.0 (sys) |
| | HLT_Photon50 | HLT_Photon70 |
| observed | 40 ± 6.5 (stat) | 11 ± 3.3 |
| pred. 30U | 60.3 ± 19.3 (stat) ± 17.1 (sys) | 17.0 ± 5.8 (stat) ± 4.7 (sys) |
| pred. 50U | 21.9 ± 4.6 (stat) ± 5.6 (sys) | 6.6 ± 2.0 (stat) ± 1.9 (sys) |
| pred. 70U | 24.3 ± 2.9 (stat) ± 3.7 (sys) | 10.3 ± 2.5 (stat) ± 3.0 (sys) |

## 6.4 Application: Multi-Electron Prediction

The successful tests on jet-triggered and photon-triggered datasets give us confidence in the predictions made by the fake rate. Now we apply the method to estimate the fake rate background in the multi-electron channel described in Chapter 5. Recall the event selection implemented for this channel:

- Exactly two good electrons, as defined in Section 5.2.2.
- At least two jets with $p_T > 40$ GeV, $|\eta| < 3.0$, and not within $\Delta R < 0.3$ of any good electron.
- An electron trigger that has the lowest possible threshold, and that has not been prescaled.

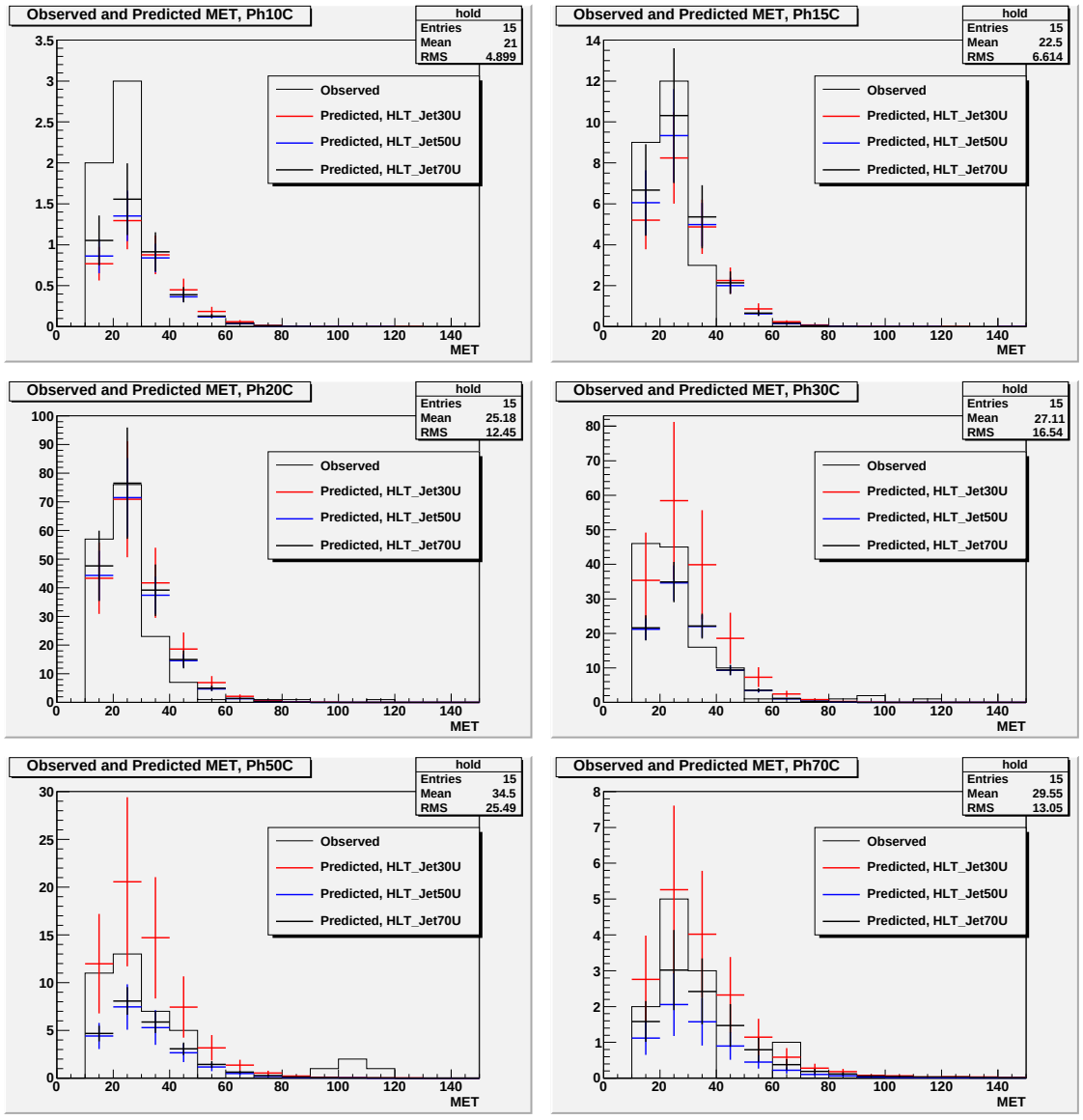


Figure 6.12: Comparison between observed and predicted $\not\!\!E_T$ distributions for fake electrons events in photon-triggered datasets. The plots show very good agreement between prediction and observation.

The fake electron background consists of events that satisfy the jet and trigger requirements, and that contain two good electrons, at least one of which is fake. To estimate this background, the first step is to define a parent sample. Events are selected that pass the jet and trigger criteria, and that contain exactly one good electron. Then the fake rate method can be applied as described in

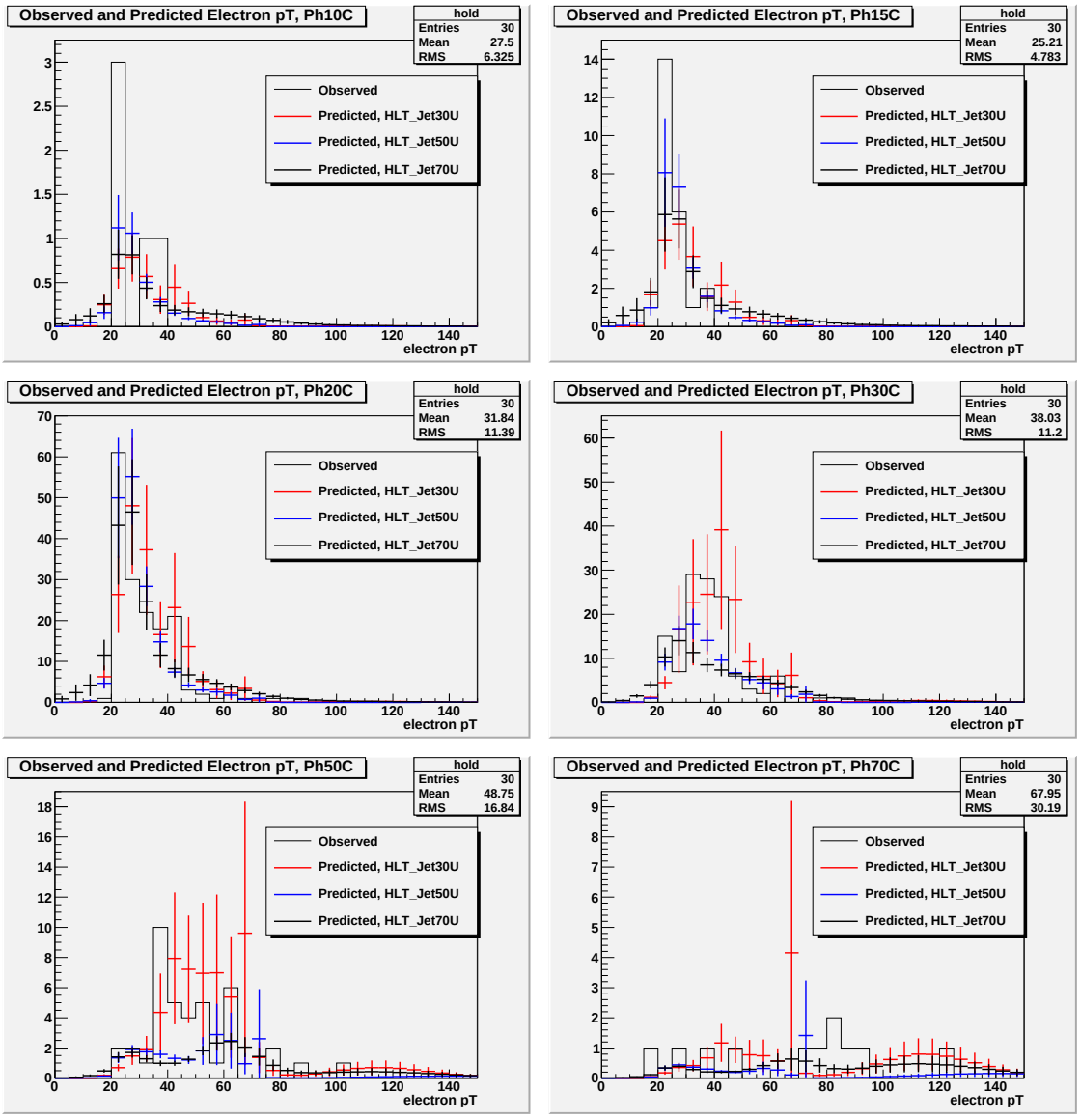


Figure 6.13: Comparison between observed and predicted fake electron $p_T$ distributions in photon-triggered datasets. Like it was with the $\not{E}_T$ distributions, the agreement between prediction and observation is good in all cases.

Section 6.2.5, with one modification. When counting $m_i$, the number of parent sample jets in fake rate bin $i$, the two jets that were required by the analysis channel definition are omitted. These jets may not be within $\Delta R < 0.3$ of any electron, so they cannot be responsible for producing a fake electron. The counts $m_i$ are obtained from the remainder of the parent sample jet content.

The results of applying the fake rate to this sample are shown in Table 6.8. Predictions are also shown for the number of fake electron events in the signal region, which has $\not\!\!E_T > 150$ GeV. This number is generated by restricting the parent sample to events that have $\not\!\!E_T > 150$ GeV, as described in Section 6.2.6.

Table 6.8: Predicted fake electron background for a multi-electron analysis in 33.84 pb$^{-1}$ of data from a low-threshold electron trigger. The first systematic uncertainty in the overall prediction is due to jet energy scale, and the second represents the variation amongst the three different predictions.

| | All events |
|---|---|
| Pred. `30U` | 1.26 ± 0.30 (stat) ± 0.27 (sys) |
| Pred. `50U` | 0.64 ± 0.07 (stat) ± 0.09 (sys) |
| Pred. `70U` | 0.77 ± 0.10 (stat) ± 0.12 (sys) |
| Overall | 0.77 ± 0.10 (stat) ± 0.12 (sys) ± 0.49 (sys) |
| | Events with $\not\!\!E_T > 150$ GeV |
| Pred. `30U` | 0.015 ± 0.004 (stat) ± 0.002 (sys) |
| Pred. `50U` | 0.008 ± 0.001 (stat) ± 0.001 (sys) |
| Pred. `70U` | 0.010 ± 0.001 (stat) ± 0.001 (sys) |
| Overall | 0.010 ± 0.001 (stat) ± 0.001 (sys) ± 0.005 (stat) |

Based on the three fake rate predictions, we take the total number of fake electron events to be $0.77 \pm 0.10$ (stat) $\pm 0.12$ (sys) $\pm 0.49$ (sys). The first systematic uncertainty is the propagation of the uncertainty due to jet energy scale; the second represents the variation between the predictions due to the different jet triggers. For comparison, recall the Monte Carlo studies in the previous chapter, which predict a total background of $127.78 \pm 1.72$ (stat) events from real electron events.

Similarly, the overall prediction for fake electron events in the signal region is $0.010 \pm 0.001$ (stat) $\pm 0.001$ (sys) $\pm 0.005$ (sys), while the Monte Carlo prediction for real electron events in this region is $0.785 \pm 0.060$ (stat) events. Both sets of results indicate that this channel is dominated by real electrons.

# CHAPTER 7

# MULTI-ELECTRON CHANNEL RESULTS

In this chapter, we conclude the new physics search in the multi-electron channel by calculating the observed signal and assessing its statistical significance. First, we compare the Monte Carlo background estimates to the number of events observed in data. The results suggest that a scale factor must be applied to the Zjets simulated numbers. Another correction factor for the Monte Carlo backgrounds is calculated using the electron reconstruction efficiencies that are measured in data and in the Monte Carlo datasets. Several sources of systematic uncertainty are discussed.

The final results for the backgrounds must be subtracted from the observation in data to obtain the signal. We present a statistical model for propagating the statistical and systematic uncertainties associated with each component of this calculation. Both Bayesian and semi-frequentist formulations are considered.

The particular quantities of interest are the numbers of events in the signal region. The notation that will be used to represent these quantities is listed below.

- The number of events observed in the signal region in 33.84 $pb^{-1}$of electron-triggered data is $d$. Observations yield $d = 1 \pm 1.0$ (stat).
- The estimated number of fake electron events in the signal region is $q$. The value calculated in the previous chapter is $q = 0.010 \pm 0.001$ (stat) $\pm$ 0.005 (sys), where the two systematic uncertainties have now been combined.

- A background estimate obtained from Monte Carlo simulations is written in the form $n_x x$, where $n_x$ is an overall normalization and $x$ is an unscaled event count. The variable $x$ ranges over the five backgrounds from Zjets, TTjets, and diboson events. The statistical and systematic uncertainties associated with $n_x$ and $x$ are described in the following sections.

## 7.1 Backgrounds from Monte Carlo Simulations

In data, the number of events that are observed to pass the event selection criteria is 181 ± 13.5 (stat). The estimated backgrounds are compared to this value in Table 7.1. The total real electron background obtained from Monte Carlo simulations is 127.78 ± 1.72 (stat), and the fake electron background is estimated to be 0.77±0.10 (stat)±0.50 (sys). The total estimated background is significantly lower than the observed number of events in data. Before attributing this discrepancy to the presence of a new physics signal, we first consider potential sources of disagreement between observed and simulated Standard Model processes. For the purposes of this section alone, we neglect the fake rate background.

Table 7.1: Summary of the estimated background events in the multi-electron channel, in comparison to the observed number of events in 33.84 $pb^{-1}$ of data. The fake electron events are estimated using the fake rate method, which is a data-driven process. The real electron events are taken from Monte Carlo simulations. This channel is dominated by real electrons, but the estimated background falls significantly short of the observation in data.

| Name | Selected events |
|---|---|
| Fake electron background | 0.77 ± 0.10 (stat) ± 0.50 (sys) |
| Real electron background | 127.78 ± 1.72 (stat) |
| Observation in data | 181 ± 13.5 (stat) |

As shown in Table 5.6, the background due to real electrons is overwhelmingly dominated by Zjets events. Therefore, we restrict our attention to those selected events that are due to a Z→ ee decay. Let $m_{inv}$ be the invariant mass of the vector sum of the two good electrons in a selected event. Figure 7.1 shows a comparison of the distributions of $m_{inv}$ in data and in the Zjets Monte Carlo dataset. The shapes of the distributions agree very well; only the total numbers of events differ.

To calculate an appropriate scale factor, we count the numbers of events whose invariant mass lies within a window about the Z mass. Specifically, we require 81 GeV $< m_{inv} <$ 101 GeV. Let the count in data be $N_{data}$, let the count in the Monte Carlo Zjets dataset be $N_{MC}$, and let the implied correction factor be $\epsilon_Z = N_{data}/N_{MC}$. The measured values are

$$N_{data} = 137 \pm 11,7 \text{ (stat)}, \tag{7.1}$$

$$N_{MC} = 91.6 \pm 1.6 \text{ (stat)}, \tag{7.2}$$

$$\epsilon_Z = 1.50 \pm 0.13 \text{ (stat)}. \tag{7.3}$$

Figure 7.1 also shows the two invariant mass plots after the scale factor $\epsilon_Z$ has been applied to the Monte Carlo dataset. The distributions now agree very well, both in shape and in scale.

Figure 7.2 shows a survey of other kinematic quantities, comparing their distributions in data to those in simulation after the Zjets dataset has been scaled by $\epsilon_Z$. All Monte Carlo datasets are now included. In all cases, whether the quantity in question pertains to jets, electrons or missing energy, the agreement between the two distributions is very good. We conclude that the Monte Carlo simulation is accurately representing the physics processes present in the data with the exception of the overall scale, which is adequately corrected by $\epsilon_Z$. Note

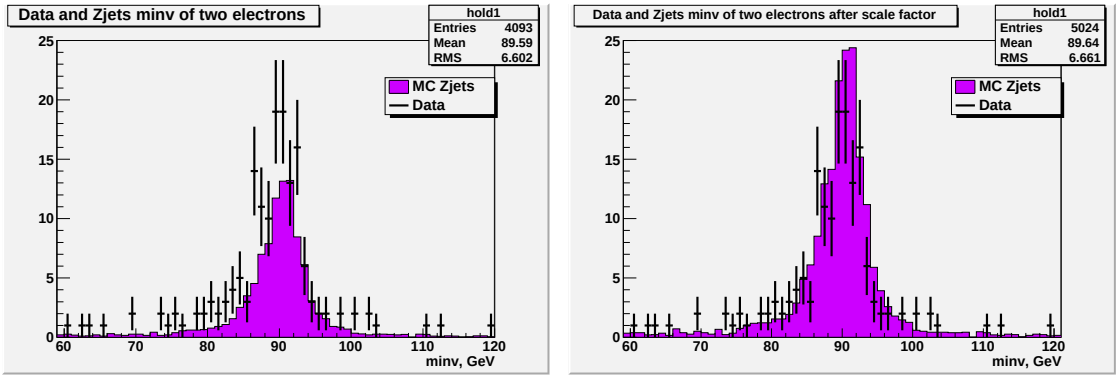


Figure 7.1: Comparison of invariant mass plots for selected events in data and in the Zjets dataset. On the left, the Zjets plot has been scaled to 33.84 $pb^{-1}$ using the weight from Table 5.4. On the right, the Zjets plot has also been scaled by the correction factor in Equation 7.3.

that the Zjets background does not contribute to the signal region at all. Therefore, this scale factor will not impact the results of a search for new physics in the signal region.

The backgrounds, including this correction factor, are summarized in Table 7.2. Once the Zjets dataset has been scaled up by $\epsilon_Z$, the total estimated background, including the fake electron contribution, is 182.36 ± 2.56 (stat) ± 0.50 (sys). This is consistent with number of selected events in data, which is 181 ± 13.5 (stat).

In the signal region, the total background is 0.795 ± 0.060 (stat) ± 0.005 (sys), and the number of signal events in data is 1.0 ± 1.0 (stat). Again, these values are consistent with each other.

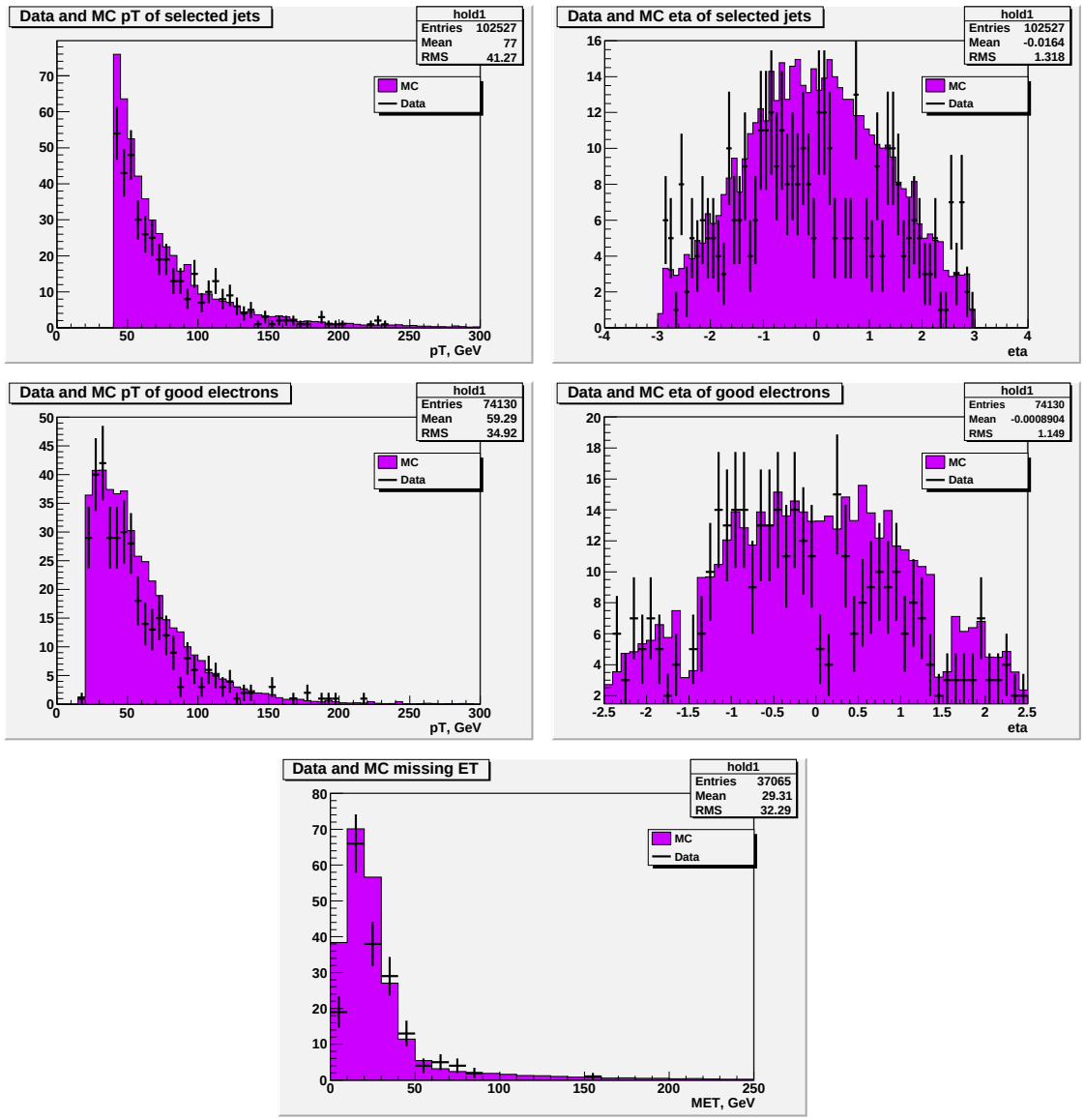


Figure 7.2: Comparison of various kinematic plots between data and all Monte Carlo backgrounds, after the Zjets dataset has been rescaled. Top row: $p_T$ and $\eta$ distributions for all jets that pass the selection criteria. Middle row: $p_T$ and $\eta$ distributions for all good electrons. Bottom row: $\not{E}_T$ distributions. There is good agreement between data and simulation.

Table 7.2: Monte Carlo and data-driven estimates for Standard Model backgrounds in 33.84 $pb^{-1}$, compared to the observed number of events in data. The selected events are those with exactly two good electrons and at least two jets. The signal events also have $\not\!\!E_T > 150$ GeV. Uncertainties are statistical unless otherwise labeled.

| Name | Selected Events | Signal Events |
|---|---|---|
| Zjets | 162.25 ± 2.54 (stat) | 0. |
| TTjets | 16.76 ± 0.28 (stat) | 0.762 ± 0.060 (stat) |
| WW | 0.16 ± 0.01 (stat) | 0.011 ± 0.003 (stat) |
| WZ | 1.41 ± 0.02 (stat) | 0.008 ± 0.002 (stat) |
| ZZ | 0.99 ± 0.01 (stat) | 0.004 ± 0.001 (stat) |
| Total MC | 181.57 ± 2.56 (stat) | 0.785 ± 0.060 (stat) |
| Fake ele | 0.77 ± 0.10 (stat) ± 0.50 (sys) | 0.010 ± 0.001 (stat) ± 0.005 (sys) |
| Total bkgd | 182.36 ± 2.56 (stat) ± 0.50 (sys) | 0.795 ± 0.060 (stat) ± 0.005 (sys) |
| Data | 181 ± 13.5 (stat) | 1 ± 1.0 (stat) |

## 7.2 Systematic Uncertainties on Monte Carlo Backgrounds

### 7.2.1 Luminosity and cross sections

The Standard Model background estimates in the signal region depend heavily on Monte Carlo simulations. In addition to the statistical uncertainties already presented, there are systematic uncertainties associated with these backgrounds.

Let the label $x$ range over the five physics processes that are estimated from simulation: Zjets, TTjets, WW, WZ and ZZ. The contribution due to one of these processes is written in the form $n_x x$, where $x$ is an unscaled event count and $n_x$ is an overall normalization.

One component of $n_x$ is the weight assigned to process $x$. The weight is given by $\frac{\mathcal{L}\sigma_x}{N_x}$, where $\mathcal{L}$ is the luminosity, $\sigma_x$ is the cross section associated with process

$x$, and $N_x$ is the total number of simulated events in the Monte Carlo dataset. For the Zjets normalization, the weight also includes the factor $\epsilon_Z$. However, this background does not contribute to the signal region, so the above expression is the only one required for the new physics search. The CMS convention for the systematic uncertainty on the luminosity measurement is 11% [74]. The uncertainty on the NLO or NNLO cross section $\sigma_x$ is listed in Table 5.4. Since all of the normalizations use the same value of $\mathcal{L}$, there is a correlation between the weights for different backgrounds.

### 7.2.2 Electron Reconstruction Efficiency

The signal region definition includes two good electrons. The number of events observed in this channel therefore depends on the efficiency with which an electron is reconstructed, and with which a good electron fires one of the electron triggers. These efficiencies may take a different value in data than in simulation. This section presents a data-driven method for measuring the electron reconstruction efficiency and the HLT efficiency. The results from the electron-triggered dataset are compared to those from the complete set of Monte Carlo files listed in Tables 5.2 and 5.3.

The efficiencies associated with the HLT and the electron identification process are measured using a procedure known as the tag and probe method. A Monte Carlo study of our implementation of this procedure has been previously performed [75]. For the purposes of this method, the initial objects are superclusters with $E_T > 20$ GeV and $|\eta| < 1.442$ or $1.560 < |\eta| < 2.5$. The electron identification process is then divided into stages as follows:

- Stage 1: the supercluster is matched to an electron that also satisfies $E_T >$ 20 GeV and $|\eta| < 1.442$ or $1.560 < |\eta| < 2.5$.
- Stage 2: the electron satisfies the combined ECAL, HCAL and track isolation requirement from the good electron definition.
- Stage 3: the isolated electron satisfies the electron identification requirements (hadronic fraction, shower shape, cluster matching) and the photon conversion rejection requirements (dist, dcot, number of missing reconstructed hits) from the good electron definition. A Stage 3 electron is a good electron.

Each stage introduces an efficiency that can be measured from data.

The tag and probe method attempts to select $Z \rightarrow ee$ events in order to obtain a pure sample of electrons on which to measure the various efficiencies. The tag electron is a good electron; or, in the case of the HLT efficiency, it is a good electron that has fired the trigger. The probe object is a less well-identified electron or supercluster such that the invariant mass of tag plus probe is within (61 GeV, 121 GeV). For a given efficiency $\epsilon_x = n_x/d_x$, the denominator is the number of tag and probe pairs, while the numerator is the number of tag and probe pairs such that the probe passes the stage of the electron identification whose efficiency is under consideration.

We measure the efficiencies in order from Stage 1 to Stage 3, followed by the trigger efficiency. The definition of the probe object evolves accordingly. Thus:

- The Stage 1 efficiency $\epsilon_{ele} = n_{ele}/d_{ele}$ is the fraction of superclusters that are matched ($\Delta R < 0.1$) to Stage 1 electrons. The probe object is a supercluster with $E_T > 20$ GeV and $|\eta| < 1.442$ or $1.560 < |\eta| < 2.5$.

- The Stage 2 efficiency $\epsilon_{iso} = n_{iso}/d_{iso}$ is the fraction of electrons that are track and calorimeter isolated. The probe object is a Stage 1 electron.
- The Stage 3 efficiency $\epsilon_{id} = n_{id}/d_{id}$ is the fraction of isolated electrons that satisfy the electron identification and photon conversion rejection requirements. The probe object is a Stage 2 electron.
- The trigger efficiency $\epsilon_{trig} = n_{trig}/d_{trig}$ is the fraction of good electrons that fire the combination of electron triggers. The probe object is a Stage 3 electron. We consider it to have fired the trigger when it is matched ($\Delta R < 0.1$) to one of the trigger objects for this event. For this efficiency, we impose the additional requirement on the tag electron that it also be matched to an HLT trigger object.

By defining the probe object in a cumulative fashion and measuring the efficiencies in a fixed order, we account for the correlations between them, and the resulting efficiencies can be multiplied as though they were independent quantities [76].

As the Stage 1 efficiency $\epsilon_{ele}$ and the Stage 2 efficiency $\epsilon_{iso}$ have the weakest probe object definitions, they exhibit the greatest degree of background contamination. A curve-fitting procedure is used to control the backgrounds in these cases. For the Stage 3 efficiency $\epsilon_{id}$ and the trigger efficiency $\epsilon_{trig}$, the background contribution is negligible, so we can count the numerator and denominator totals directly.

The tag and probe measurements of the Stage 1 and Stage 2 efficiencies suffer from substantial fake electron background contamination that affects the denominators much more than the numerators, thereby underestimating the true efficiency values. The two efficiencies in question are $\epsilon_{ele} = n_{ele}/d_{ele}$ and

$\epsilon_{iso} = n_{iso}/d_{iso}$. Each numerator and denominator is a count for which we need an estimate. Take the $d_{ele}$ case as an example; the other three follow the same procedure.

Whenever a tag and probe pair satisfies the denominator conditions for the Stage 1 efficiency, we add the invariant mass of tag plus probe to a histogram whose range is the Z mass window, (61 GeV, 121 GeV). This histogram will contain a mixture of contributions from signal and background. We assume that the signal entries follow a scaled Breit-Wigner distribution centered on the Z mass [77], and that the background distribution can be modeled by a polynomial. Therefore, we fit the histogram with a function of the form

$$F(x; p_0, p_1, p_2, p_3, p_4, p_5) = \frac{p_0}{2\pi} \frac{p_2}{(x - p_1)^2 + p_2^2/4} + p_3 x^2 + p_4 x + p_5. \tag{7.4}$$

Once the parameters have been fitted, we take the integral of the Breit-Wigner term over the mass window to obtain a count. This is the estimate of the signal yield for $d_{ele}$.

We implement the fitting process in ROOT, which returns a matrix of covariances for the fitted parameters. Since $d_{ele}$ is a function of $p_0$, $p_1$ and $p_2$, we calculate its variance by

$$\mathrm{Var}(d_{ele}) \approx \sum_{i=0}^{2} \sum_{j=0}^{2} \frac{\partial d_{ele}}{\partial p_i} \frac{\partial d_{ele}}{\partial p_j} \mathrm{Cov}(p_i, p_j). \tag{7.5}$$

More specifically, if we denote the interval of integration by $(A, B)$, then the fitted value for $d_{ele}$ is

$$d_{ele} = \int_A^B \frac{p_0}{2\pi} \frac{p_2}{(x - p_1)^2 + p_2^2/4} \, dx \tag{7.6}$$

$$= \frac{p_0}{\pi} \tan^{-1} \left[ \frac{2}{p_2} (x - p_1) \right]_A^B \tag{7.7}$$

The partial derivatives of this expression with respect to each of the three parameters are

$$\frac{\partial d_{ele}}{\partial p_0} = \frac{1}{\pi}\tan^{-1}\left[\frac{2}{p_2}(x-p_1)\right]_A^B, \tag{7.8}$$

$$\frac{\partial d_{ele}}{\partial p_1} = -\frac{p_0 p_2}{2\pi}\frac{1}{(x-p_1)^2+p_2^2/4}\Bigg|_A^B, \tag{7.9}$$

$$\frac{\partial d_{ele}}{\partial p_2} = -\frac{p_0}{2\pi}\frac{x-p_1}{(x-p_1)^2+p_2^2/4}\Bigg|_A^B. \tag{7.10}$$

These expressions are the source of the systematic uncertainties quoted for $d_{ele}$ and the other three fitted event counts.

Figure 7.3 shows the fitted invariant mass histograms for the four event counts. In each case, the fitted function $F$ is superimposed on the histogram in black. The Breit-Wigner and polynomial terms are plotted individually in blue and red, respectively. Note: it is not necessarily our contention that the fitted background curve is an accurate representation of the number of background events in the histogram. However, we find that the ratio of numerator to denominator events after subtracting the background curve is a reasonably good model for the Stage 1 and Stage 2 efficiencies.

Suppose we have now obtained some numerator and denominator counts $n_x$ and $d_x$ for a particular efficiency $\epsilon_x = n_x/d_x$, whether from the fitting process or direct observation. Since the events in the numerator are a subset of those in the denominator, $n_x$ and $d_x$ are not independent variables. Define $f_x = d_x - n_x$; that is, $f_x$ is the number of events that fail the numerator condition. Then $n_x$ and $f_x$ are independent, and $\epsilon_x = n_x/(n_x + f_x)$. Therefore, we can express the variance of $\epsilon_x$ as

$$\mathrm{Var}(\epsilon_x) \approx \left(\frac{\partial \epsilon_x}{\partial n_x}\right)^2 \mathrm{Var}(n_x) + \left(\frac{\partial \epsilon_x}{\partial f_x}\right)^2 \mathrm{Var}(f_x) \tag{7.11}$$

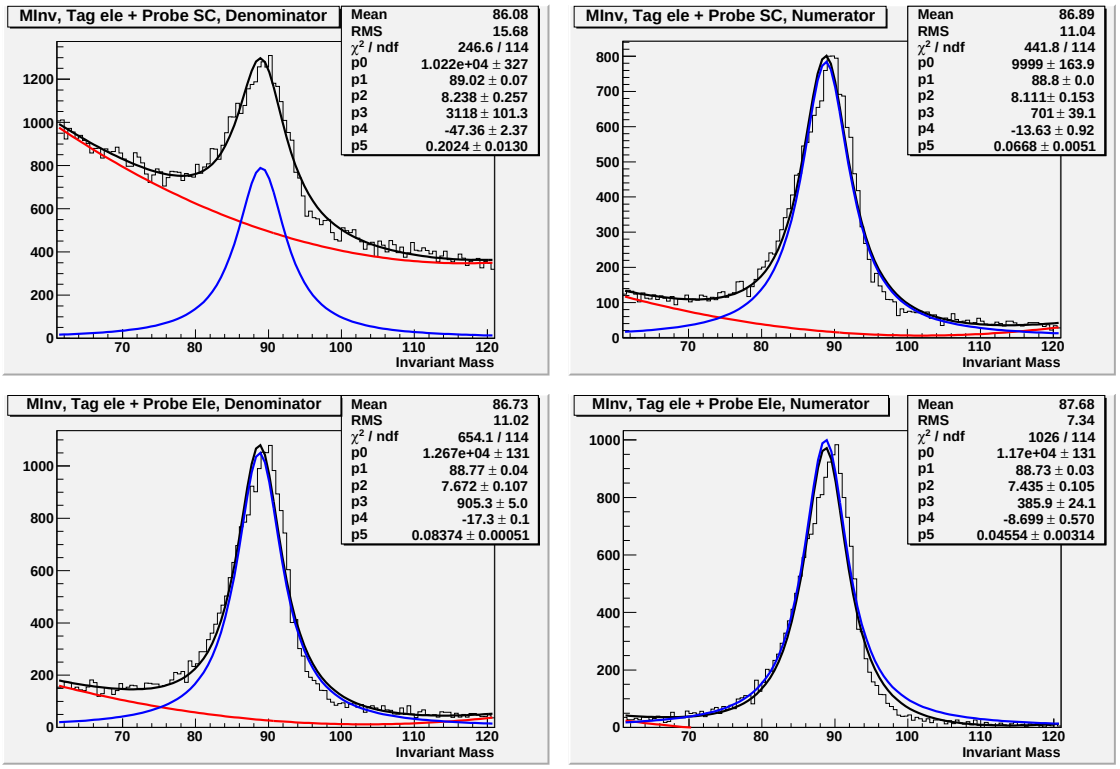


Figure 7.3: Results of curve fitting procedure for the four tag and probe counts $d_{ele}$ and $n_{ele}$ (top row), and $d_{iso}$ and $n_{iso}$ (bottom row). The overall fit function is in black, while the Breit-Wigner and polynomial components are in blue and red, respectively.

$$= \frac{1}{(n_x + f_x)^4} \left[ f^2 \mathrm{Var}(n_x) + n^2 \mathrm{Var}(f_x) \right]. \tag{7.12}$$

If we note that $\mathrm{Var}(d_x) = \mathrm{Var}(n_x + f_x) = \mathrm{Var}(n_x) + \mathrm{Var}(f_x)$, then we can rewrite the above in terms of $d_x$ and $n_x$ as

$$\mathrm{Var}(\epsilon_x) = \frac{1}{d_x^2} \left[ (1 - 2\epsilon_x)\, \mathrm{Var}(n_x) + \epsilon_x^2 \mathrm{Var}(d_x) \right]. \tag{7.13}$$

This expression is used to calculate the uncertainties on all of the measured efficiencies.

Table 7.3 shows the results for numerator, denominator and efficiency for all stages of the electron identification, and for the HLT. The statistical uncertainties on $\epsilon_{ele}$ and $\epsilon_{iso}$ arise from the tag and probe method plus fitting, while those

on $\epsilon_{id}$ and $\epsilon_{trig}$ arise from assigning the standard Poisson uncertainties to the numerator and denominator. Also shown is the total efficiency per electron of the electron identification process, which is given by $\epsilon = \epsilon_{ele} \cdot \epsilon_{iso} \cdot \epsilon_{id}$. The latter number agrees very well with that measured in an earlier study on 2.9 $pb^{-1}$of data from the `HLT_Ele15_SW_CaloEleId_L1R` trigger [78].

Table 7.3: Tag and probe results for numerator, denominator and efficiency for each of the stages of electron identification, and for the HLT efficiency, using electron-triggered data. Statistical uncertainties are due to the background fitting process for $\epsilon_{ele}$ and $\epsilon_{iso}$, and due to Poisson statistics for $\epsilon_{id}$ and $\epsilon_{trig}$. The final entry is $\epsilon = \epsilon_{ele} \cdot \epsilon_{iso} \cdot \epsilon_{id}$, which is the total efficiency for reconstructing a good electron from a supercluster.

| Quantity | | Value |
|---|---|---|
| Stage 1 | $n_{ele}$ | 18280 ± 950 |
| | $d_{ele}$ | 18700 ± 1900 |
| | $\epsilon_{ele}$ | 0.979 ± 0.085 |
| Stage 2 | $n_{iso}$ | 21550 ± 270 |
| | $d_{iso}$ | 23280 ± 800 |
| | $\epsilon_{iso}$ | 0.926 ± 0.022 |
| Stage 3 | $n_{id}$ | 16440 ± 130 |
| | $d_{id}$ | 19750 ± 140 |
| | $\epsilon_{id}$ | 0.832 ± 0.003 |
| HLT | $n_{trig}$ | 15880 ± 130 |
| | $d_{trig}$ | 16290 ± 130 |
| | $\epsilon_{trig}$ | 0.975 ± 0.001 |
| Good electron | $\epsilon$ | 0.755 ± 0.070 |

To assess a possible systematic dependence on the width of the Z mass window, we repeated the procedure using intervals of (66 GeV, 116 GeV) and (71 GeV, 111 GeV). All of the efficiency values were found to agree with those in Table 7.3 to within statistical uncertainty. Therefore, we assume that our method is reasonably independent of the width of this interval. We choose to consider results from (61 GeV, 121 GeV) because they have the most observations, and therefore the smallest statistical uncertainties.

Next, we apply this same procedure to the complete set of Standard Model Monte Carlo files, weighted to correspond to a luminosity of 33.84 $pb^{-1}$. To distinguish them from the values measured on data, the efficiencies measured on simulated files will be denoted $\epsilon'_x = n'_x/d'_x$. The results are given in Table 7.4. Because there is no trigger information available for the Monte Carlo files, we do not calculate $\epsilon'_{trig}$.

Table 7.4: Tag and probe Monte Carlo results for numerator, denominator and efficiency for each of the stages of electron identification. Statistical uncertainties are due to the background fitting process for $\epsilon'_{ele}$ and $\epsilon'_{iso}$, and due to Poisson statistics combined with the dataset weights for $\epsilon'_{id}$. The final entry is $\epsilon' = \epsilon'_{ele} \cdot \epsilon'_{iso} \cdot \epsilon'_{id}$, which is the total efficiency in simulation for reconstructing a good electron from a supercluster.

| Quantity | | Value |
|---|---|---|
| Stage 1 | $n'_{ele}$ | 27090 ± 930 |
| | $d'_{ele}$ | 29400 ± 1200 |
| | $\epsilon'_{ele}$ | 0.923 ± 0.026 |
| Stage 2 | $n'_{iso}$ | 38220 ± 810 |
| | $d'_{iso}$ | 39600 ± 1300 |
| | $\epsilon'_{iso}$ | 0.966 ± 0.024 |
| Stage 3 | $n'_{id}$ | 37523 ± 32 |
| | $d'_{id}$ | 42756 ± 35 |
| | $\epsilon'_{id}$ | 0.878 ± 0.002 |
| Good electron | $\epsilon'$ | 0.783 ± 0.029 |

The efficiencies $\epsilon, \epsilon_{trig}$ and $\epsilon'$ can be used to construct a correction factor to the Monte Carlo background normalizations. For example, consider a leptonic $t\bar{t}$ event. For it to pass the event selection criteria, both electrons must be reconstructed, and at least one of them must satisfy the trigger. Therefore the probability that this event will be selected in data is

$$P_{ele}(\epsilon) = \epsilon^2 \left[1 - \left(1 - \epsilon_{trig}\right)^2\right]. \tag{7.14}$$

The probability in simulation is

$$P_{ele}(\epsilon') = \epsilon'^2, \tag{7.15}$$

since the trigger efficiency is taken to be 100%. The correction factor for the Monte Carlo background is then $P_{ele}(\epsilon)/P_{ele}(\epsilon')$.

By the same reasoning, this correction factor also applies to the WW background. In principle, the correction factors for the WZ and ZZ backgrounds should take a slightly different form that reflects the different permutations of decay products that could give rise to two good electrons. However, since these backgrounds are very small relative to $t\bar{t}$, we disregard any such modifications and use the same correction factor $P_{ele}(\epsilon)/P_{ele}(\epsilon')$ in all cases.

Combining this expression with the weight found in the previous section yields the overall scale factor associated with process $x$:

$$n_x = \frac{\mathcal{L}\sigma_x}{N_x}\frac{P_{ele}(\epsilon)}{P_{ele}(\epsilon')}. \tag{7.16}$$

Note that the scale factors associated with different processes are correlated due to the shared values of $\mathcal{L}$ and the various electron efficiencies.

### 7.2.3 Jet Energy Scale and Other Systematics

Other issues that might affect the comparison between Monte Carlo simulation and data are the jet energy scale and $\not\!\!E_T$ resolution. To test the dependence on jet energy scale, we recalculate all of the five Monte Carlo backgrounds after scaling all of the jet $p_T$ values by a factor of 1.1, and again by a factor of 0.9. In the signal region, let $x$ be the original unscaled count in the signal region, and

let $x_{1.1}$ and $x_{0.9}$ be the new counts after rescaling. The systematic uncertainty on $x$ associated with jet energy scale is the larger of $|x - x_{1.1}|$ or $|x - x_{0.9}|$. The results are listed in Table 7.5.

Table 7.5: Effect of jet energy scale on the Monte Carlo unscaled backgrounds, and the systematic uncertainties assigned.

| Name | Original unscaled | ×0.9 | ×1.1 | Systematic |
|---|---|---|---|---|
| TTjets | 159 | 148 | 166 | ±11 |
| WW | 16 | 14 | 18 | ±2 |
| WZ | 30 | 29 | 33 | ±3 |
| ZZ | 38 | 35 | 41 | ±3 |

The $\not\!\!E_T$ resolution has a Gaussian distribution in the central region, and long non-Gaussian tails. The latter feature occurs when a large $\not\!\!E_T$ value is measured for events whose true $\not\!\!E_T$ is small. This is expected to happen more often in data than in simulation. In a previous study [65], sensitivity to this effect was simulated by scaling up each Monte Carlo background by factors ranging from 1.5 to 3. In the present analysis, it is clear from the very small numbers of observed signal region events that scaling up the Monte Carlo backgrounds would easily remove any trace of a signal. Thus, we omit this step for the time being, but note for future work that an understanding of the $\not\!\!E_T$ resolution in data is essential before attributing an excess of high-$\not\!\!E_T$ events to a new physics signal.

## 7.3 Summary of Inputs and Uncertainties

The following quantities all contribute to the calculation of the signal.

- The number of events observed in the signal region in 33.84 $\text{pb}^{-1}$of

electron-triggered data is $d = 1 \pm 1.0$ (stat).

- The number of fake electron events in the signal region is estimated to be $q = 0.010 \pm 0.001$ (stat) $\pm$ 0.005 (sys). The systematic uncertainty is due to the effects of jet energy scale and trigger bias.
- The backgrounds that are estimated from Monte Carlo simulations take the form $n_x x$, where $x$ ranges over the processes TTjets, WW, WZ and ZZ (the Zjets contribution is zero). The event count $x$ has a Poisson statistical uncertainty and a systematic uncertainty due to jet energy scale. The coefficient $n_x$ has systematic uncertainties due to the luminosity of the dataset, the cross section of the process, and the electron reconstruction efficiencies in data and simulation.

The total background $b$ is then given by

$$b = q + \sum_x n_x x. \tag{7.17}$$

We must now determine whether there is a statistically significant difference between $d$ and $b$.

## 7.4 A Statistical Model

The inputs to the analysis are the data event count $d$, the background estimates $x$ and $q$, and the components that make up the normalization coefficients $n_x$. Each one has an associated uncertainty, which may include both statistical and systematic contributions. All of these quantities are used to calculate the signal in the signal region. To assess whether this signal represents a significant devi-

ation from the Standard Model, the statistical and systematic uncertainties on $b$ and $d$ must be properly propagated.

In this section, we review Bayesian posterior probability distribution functions and frequentist confidence intervals, and we describe the Monte Carlo computer simulation used to propagate the uncertainties on the inputs.

### 7.4.1 Bayesian and semi-frequentist formulations

Each input to the calculation of the background is the observed value of some variable that has an expected value and a standard deviation. Given an observed value $y$, let the corresponding expected value be $\langle y \rangle$, and let the standard deviation be $\sigma_y$.

- **Bayesian formulation**: Having now observed $b$ and $d$ in the signal region, we want to find the posterior probability distribution function (pdf) for the expected value $\langle s \rangle$. Given expected values $\langle d \rangle$ and $\langle b \rangle$, we have $\langle s \rangle = \langle d \rangle - \langle b \rangle$. The observed values for the data and for the various contributions to $b$ are used to construct pdfs for $\langle b \rangle$ and $\langle d \rangle$. Then the mean and standard deviation of the distribution for $\langle s \rangle$ are determined by integrating the quantity $\langle d \rangle - \langle b \rangle$ over these pdfs. A mean value of $\langle s \rangle$ that is several standard deviations above zero indicates the presence of a signal that is distinct from the Standard Model background.

  Given an expected value $\langle b \rangle$, we can also calculate the Poisson probability that an observation of $b$ will equal or exceed the observed signal $d$. This value, integrated over the pdf for $\langle b \rangle$, represents the probability that the

background alone could fluctuate high enough to account for the observed data.

- **Frequentist formulation**: Given a hypothesis for the expected value $\langle s \rangle$, we want to find the probability of observing a particular value of $d$. Given also the expected value $\langle b \rangle$, the expected value for $d$ is $\langle d \rangle = \langle s \rangle + \langle b \rangle$. Thus, $d$ is modeled with a Poisson distribution that has a mean value of $\langle s \rangle + \langle b \rangle$:

$$P(d|\langle s \rangle, \langle b \rangle) = \frac{(\langle s \rangle + \langle b \rangle)^d \, e^{-(\langle s \rangle + \langle b \rangle)}}{d!}. \tag{7.18}$$

  By varying $\langle s \rangle$ and $d$, we can construct a two-dimensional map of the probabilities of observing different $d$ values, given different hypotheses for $\langle s \rangle$. The particular value of $d$ that is observed in the experiment will fall somewhere on this probability map; the range of $\langle s \rangle$ values for which this observation is likely constitute a confidence interval.

  We do not have a precise value for $\langle b \rangle$, but we can construct a posterior pdf for it out of the observed values of the various backgrounds. Then $P(d|\langle s \rangle, \langle b \rangle)$ is integrated over this pdf to eliminate dependence on $\langle b \rangle$:

$$P(d|\langle s \rangle) = \int P(d|\langle s \rangle, \langle b \rangle) P(\langle b \rangle) \, d\langle b \rangle \, . \tag{7.19}$$

  Since the posterior pdf for $\langle b \rangle$ is a necessary component of the calculation, the confidence intervals so constructed are not fully frequentist, but semi-Bayesian.

Thus, both approaches depend on constructing a pdf for $\langle b \rangle$ and then integrating over it. In practice, this amounts to running a Monte Carlo computer simulation over many different values of $\langle b \rangle$. We now construct the distributions that go into the simulation.

### 7.4.2 Simulation of uncertainties

For each independent input, we construct a probability distribution for the expected value $\lambda$ whose mean is the observed value $k$ and whose standard deviation is the total uncertainty $\sigma$. Because all of the inputs – luminosity, cross sections, efficiencies and event counts – are nonnegative quantities, we simulate each of them using a Gamma distribution:

$$P(\lambda) = \frac{\lambda^{\alpha-1} e^{-\lambda/\beta}}{\beta^{\alpha}\Gamma(\alpha)}. \tag{7.20}$$

The mean of this distribution is $\alpha\beta$, and the variance is $\alpha\beta^2$. Therefore, we choose $\alpha$ and $\beta$ such that $\alpha\beta = k$ and $\alpha\beta^2 = \sigma^2$.

The appropriate distribution is constructed for each independent input to the background calculation. For every iteration of the computer simulation, a new random value is selected from each distribution, and these values are used to calculate $\langle b \rangle$. If a variable occurs more than once in the calculation, the same random value is used in every instance. Thus, the simulation correctly models correlations between different components of the background. The resulting $\langle b \rangle$ is then used in the Bayesian and frequentist probability calculations described above.

For the Bayesian formulation, it is straightforward to maintain running computations of the mean and variance of the simulated $\langle s \rangle$ values. The construction of confidence intervals is somewhat more involved, and is described in Section 7.4.3.

### 7.4.3 Semi-frequentist confidence intervals

The Poisson probability $P(d|\langle s\rangle, \langle b\rangle)$ from Equation 7.19 must be numerically integrated over the pdf for $\langle b\rangle$. In each iteration of the computer simulation, we calculate $\langle b\rangle$, then perform a scan over a grid of $\langle s\rangle$ and $d$ values. At each point in the grid, we construct the expected value $\langle d\rangle = \langle b\rangle + \langle s\rangle$, and calculate the Poisson probability of observing $d$. The probabilities at each $\langle s\rangle - d$ point are averaged over many iterations to yield $P(d|\langle s\rangle)$ at that point. Once $P(d|\langle s\rangle)$ has been constructed for the entire grid, the Feldman-Cousins recipe for unified confidence intervals [79] can be applied as follows.

- For each value of $d$:
  - Find the maximum value of $P(d|\langle s\rangle)$ by looping over all $\langle s\rangle$. Denote this value $P_{\max}(d)$.
  - Form the likelihood ratio $R(d, \langle s\rangle) \equiv P(d|\langle s\rangle)/P_{\max}(d)$ for all $\langle s\rangle$ at the given $d$.
- Then, for each value of $\langle s\rangle$:
  - Rank the $d$ values according to $R(d, \langle s\rangle)$.
  - Form the acceptance region beginning with the $d$ of highest rank, and successively including $d$ values of lower rank until the summed $P(d|\langle s\rangle)$ has reached the desired confidence level.

Thus, an acceptance region is a collection of $d$ values at a fixed $\langle s\rangle$. The union of these acceptance regions over all $\langle s\rangle$ is the confidence belt. The frequentist confidence interval is the range of $\langle s\rangle$ values enclosed by this belt at the observed value of $d$.

The Bayesian and semi-frequentist results will be reported and compared in the next section.

## 7.5 Results

Table 7.6 lists the Bayesian and semi-frequentist results after 10000 iterations of the toy Monte Carlo simulation. Plots of the Bayesian distributions for data, signal and background are shown in Figure 7.4. The probability map and semi-frequentist 95% confidence belt are shown in Figure 7.5.

The Bayesian expectation value for the signal is $\langle s \rangle = 0.238 \pm 0.996$ (stat) $\pm$ 0.304 (sys). The probability that the background alone will fluctuate high enough to account for the observation in data is 51.6%. The semi-frequentist analysis indicates that $\langle s \rangle \in [0, 4.4]$ with 95% confidence. All of these results are in agreement with each other, and they indicate that the observation is consistent with zero signal.

Table 7.6: Bayesian and semi-frequentist results in the multi-electron channel.

| Quantity | Result |
|---|---|
| Data | $\langle d \rangle = 0.985 \pm 0.969$ (stat) |
| TTjets | $\langle n_t t \rangle = 0.715 \pm 0.159$ (stat) $\pm$ 0.107 (sys) |
| WW | $\langle n_{ww} ww \rangle = 0.011 \pm 0.003$ (stat) $\pm$ 0.002 (sys) |
| WZ | $\langle n_{wz} wz \rangle = 0.008 \pm 0.002$ (stat) $\pm$ 0.001 (sys) |
| ZZ | $\langle n_{zz} zz \rangle = 0.003 \pm 0.001$ (stat) $\pm$ 0.001 (sys) |
| Fake ele | $\langle q \rangle = 0.0100 \pm 0.0001$ (stat) $\pm$ 0.0001 (sys) |
| Background | $\langle b \rangle = 0.747 \pm 0.158$ (stat) $\pm$ 0.104 (sys) |
| Signal | $\langle s \rangle = 0.238 \pm 0.996$ (stat) $\pm$ 0.304 (sys) |
| prob bkg fluc | 0.516 $\pm$ 0.005 (stat) |
| 95% confidence interval | $[0, 4.4]$ |

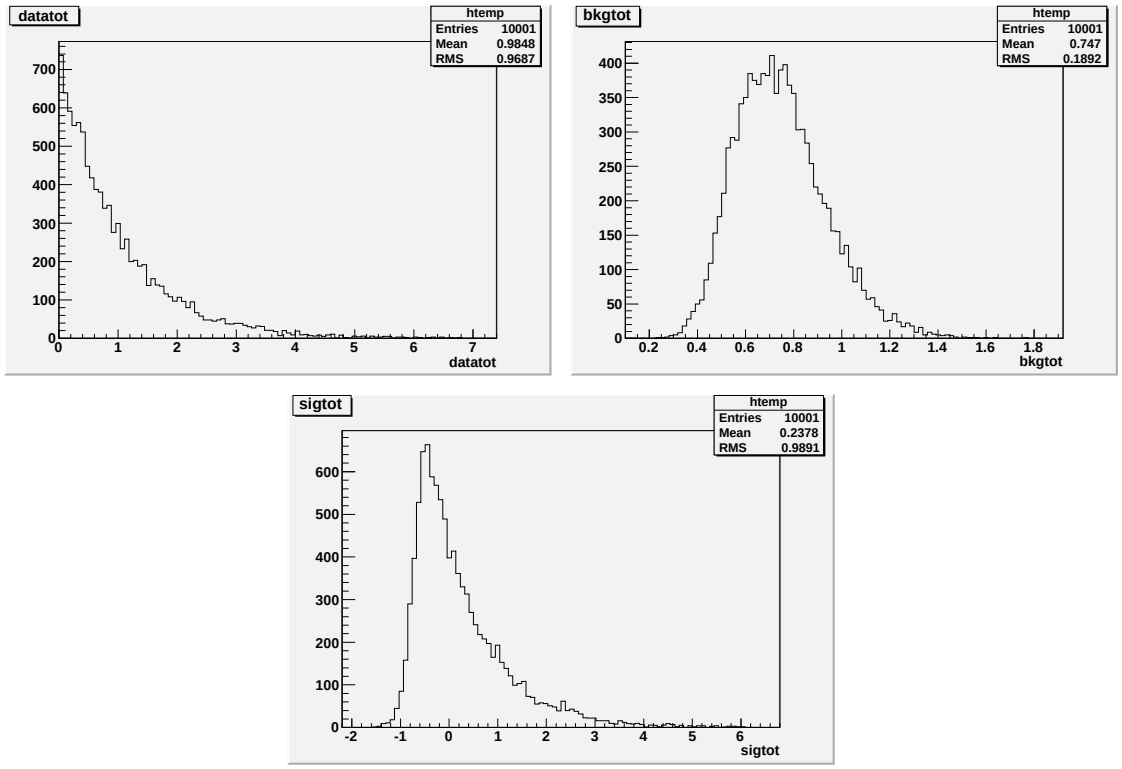


Figure 7.4: Bayesian distributions for $\langle d \rangle$ (top left), $\langle b \rangle$ (top right), and $\langle s \rangle$ (bottom). The mean of the signal distribution is within less than one standard deviation of zero.

## 7.6 Test Points in mSUGRA Parameter Space

The above analysis was designed to be model-independent. However, the technique can be adapted to assess whether the observed events in data are consistent with a given new physics hypothesis. As examples, we take two low mass (LM) points in the minimal supergravity model for which Monte Carlo files have been generated.

The points we consider are labeled LM0 and LM1. They are specific selections from the five-dimensional parameter space $\left\{\tan\beta, m_0, m_{1/2}, A, \text{sign}(\mu)\right\}$. Their definitions are listed in Table 7.7. Information about the correspond-

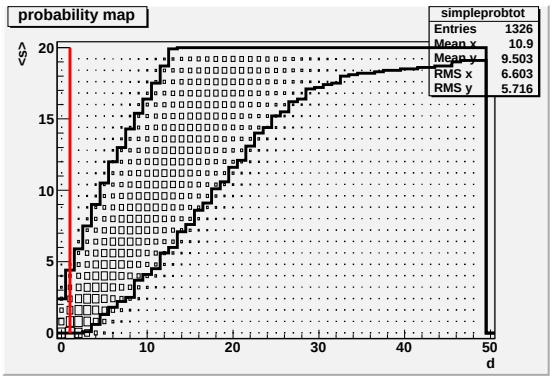


Figure 7.5: The probability map generated by the statistics simulation. The limits of the 95% confidence belt are marked in black. The observed data value is marked in red.

ing datasets, including cross sections and weights, is shown in Tables 7.8 and 7.9. The final cross sections used in the computation of the weights are next-to-leading order, and they were obtained by multiplying the leading order values by the given k-factors. These particular points were chosen from a larger set of available LM test points because they had the largest cross sections, and therefore they made the largest contributions to the signal region. The contributions from these two points are shown in Table 7.10.

Table 7.7: Parameter values for the low mass (LM) mSUGRA test points.

| Name | $\tan\beta$ | $m_0$ | $m_{1/2}$ | $A_0$ | sign($\mu$) |
|---|---|---|---|---|---|
| LM0 | 10 | 200 | 160 | -400 | + |
| LM1 | 10 | 60 | 250 | 0 | + |

Table 7.8: Names of LM test point datasets.

| Name | Dataset |
|---|---|
| LM0 | /LM0_SUSY_sftsht_7TeV-pythia6/Fall10-START38_V12-v1/AODSIM |
| LM1 | /LM1_SUSY_sftsht_7TeV-pythia6/Fall10-START38_V12-v1/AODSIM |

To determine whether the observed number of signal region events in data

Table 7.9: Cross sections, k-factors and weights for the LM test point datasets. The weights were calculated using the NLO cross sections, which are (LO cross section) × (k-factor). The cross section of the end product is 33.84 $pb^{-1}$. The systematic uncertainty on $\sigma$(NLO) is taken to be $\sigma$(NLO) − $\sigma$(LO).

| Name | $\sigma$(LO) (pb) | k-factor | $\sigma$(NLO) (pb) | # Events | Weight |
|---|---|---|---|---|---|
| LM0 | 38.93 | 1.41 | 54.89 | 219595 | $8.459 \times 10^{-3}$ |
| LM1 | 4.888 | 1.34 | 6.550 | 219190 | $1.011 \times 10^{-3}$ |

favors or disfavors a particular LM hypothesis, we include the predicted number of LM events as another Monte Carlo background, and repeat the statistical simulation. If $l$ represents the unweighted LM event count and $n_l$ represents its overall scale factor, then

$$n_l = \frac{\mathcal{L}\sigma_l}{N_l} \frac{P_{ele}(\epsilon)}{P_{ele}(\epsilon')}, \tag{7.21}$$

where $\mathcal{L}$ is the total luminosity, $\sigma_l$ is the NLO cross section of the LM point, $N_l$ is the number of simulated LM events, and $P_{ele}(\epsilon)$ and $P_{ele}(\epsilon')$ are the measured and simulated probabilities for an event to contain two good electrons, as discussed in Section 7.2.2. We take the systematic uncertainty on $\sigma_l$ to be $\sigma_l$(NLO)−$\sigma_l$(LO). The systematic uncertainty on $l$ due to jet energy scale is listed in Table 7.10 for each of the candidate points. The uncertainties on the other quantities are as discussed for the Standard Model Monte Carlo backgrounds.

Table 7.10: Numbers of events in the signal region in 33.84 $pb^{-1}$for the LM test points. Statistical uncertainty and systematic uncertainty due to jet energy scale are both shown.

| Name | Signal Events |
|---|---|
| LM0 | 2.99 ± 0.16 (stat) ± 0.07 (sys) |
| LM1 | 1.00 ± 0.03 (stat) ± 0.01 (sys) |

The total background now takes the form

$$b = \sum_x n_x x + q + n_l l. \tag{7.22}$$

With this new formulation, the difference between the predicted background and the observation in data represents the deviation from the particular LM hypothesis under consideration; that is, a signal of zero means that the data are consistent with the LM point.

Table 7.11 shows the Bayesian and semi-frequentist results for the LM0 test point. Figure 7.6 shows the Bayesian distributions for data, background and signal. The probability map and 95% confidence belt are shown in Figure 7.7.

The expected value of the signal is $\langle s \rangle = -2.58 \pm 1.24\ (\text{stat}) \pm 1.23\ (\text{sys})$, which is within about 1.5 standard deviations of zero. Since $\langle b \rangle > d$, we reverse the interpretation of the probability of background fluctuation: the probability for a Poisson distribution with expected value $\langle b \rangle$ to fluctuate as low as $d$ is about 5%. Finally, the semi-frequentist 95% confidence interval for $\langle s \rangle$ is $[0, 2.82]$. All of these results indicate that we can exclude LM0 to approximately $1.5\sigma$ with the given observations.

Since the point LM1 has an even smaller signal region contribution, it is not surprising to find that it is also compatible with the observed data. When the above analysis is repeated using LM1, the expected value of the signal is $\langle s \rangle = -0.70 \pm 1.04\ (\text{stat}) \pm 0.37\ (\text{sys})$, the probability for the background to fluctuate as low as the observed data is about 21%, and the 95% confidence interval for $\langle s \rangle$ is $[0, 3.53]$. All of these figures indicate that the observation is consistent with the LM1 prediction. Table 7.12 lists the numerical results for the statistics simulation. Figures 7.8 and 7.9 show the Bayesian pdfs, probability map, and 95% confidence belt.

Table 7.11: Bayesian and semi-frequentist results in the multi-electron channel when LM0 is included in the background calculation.

| Quantity | Result |
|---|---|
| Data | $\langle d \rangle = 0.997 \pm 0.969$ (stat) |
| LM0 | $\langle n_l l \rangle = 2.83 \pm 0.59$ (stat) $\pm 1.23$ (sys) |
| TTjets | $\langle n_t t \rangle = 0.715 \pm 0.156$ (stat) $\pm 0.101$ (sys) |
| WW | $\langle n_{ww} ww \rangle = 0.011 \pm 0.003$ (stat) $\pm 0.002$ (sys) |
| WZ | $\langle n_{wz} wz \rangle = 0.008 \pm 0.002$ (stat) $\pm 0.001$ (sys) |
| ZZ | $\langle n_{zz} zz \rangle = 0.003 \pm 0.001$ (stat) $\pm 0.001$ (sys) |
| Fake ele | $\langle q \rangle = 0.0100 \pm 0.0001$ (stat) $\pm 0.0001$ (sys) |
| Background | $\langle b \rangle = 3.58 \pm 0.73$ (stat) $\pm 1.25$ (sys) |
| Signal | $\langle s \rangle = -2.58 \pm 1.24$ (stat) $\pm 1.23$ (sys) |
| prob bkg fluc | $0.950 \pm 0.002$ (stat) |
| 95% confidence interval | $[0, 2.82]$ |

Table 7.12: Bayesian and semi-frequentist results in the multi-electron channel when LM1 is included in the background calculation.

| Quantity | Result |
|---|---|
| Data | $\langle d \rangle = 0.990 \pm 0.980$ (stat) |
| LM1 | $\langle n_l l \rangle = 0.942 \pm 0.189$ (stat) $\pm 0.347$ (sys) |
| TTjets | $\langle n_t t \rangle = 0.716 \pm 0.153$ (stat) $\pm 0.104$ (sys) |
| WW | $\langle n_{ww} ww \rangle = 0.011 \pm 0.003$ (stat) $\pm 0.002$ (sys) |
| WZ | $\langle n_{wz} wz \rangle = 0.008 \pm 0.002$ (stat) $\pm 0.001$ (sys) |
| ZZ | $\langle n_{zz} zz \rangle = 0.003 \pm 0.001$ (stat) $\pm 0.001$ (sys) |
| Fake ele | $\langle q \rangle = 0.0100 \pm 0.0001$ (stat) $\pm 0.0001$ (sys) |
| Background | $\langle b \rangle = 1.69 \pm 0.34$ (stat) $\pm 0.39$ (sys) |
| Signal | $\langle s \rangle = -0.70 \pm 1.04$ (stat) $\pm 0.37$ (sys) |
| prob bkg fluc | $0.792 \pm 0.004$ (stat) |
| 95% confidence interval | $[0, 3.53]$ |

## 7.7 Conclusion

This document has presented the results of a search for evidence of physics beyond the Standard Model in a channel with two good electrons, two jets, and $\not\!\!E_T > 150$ GeV. The total number of events observed in this channel from

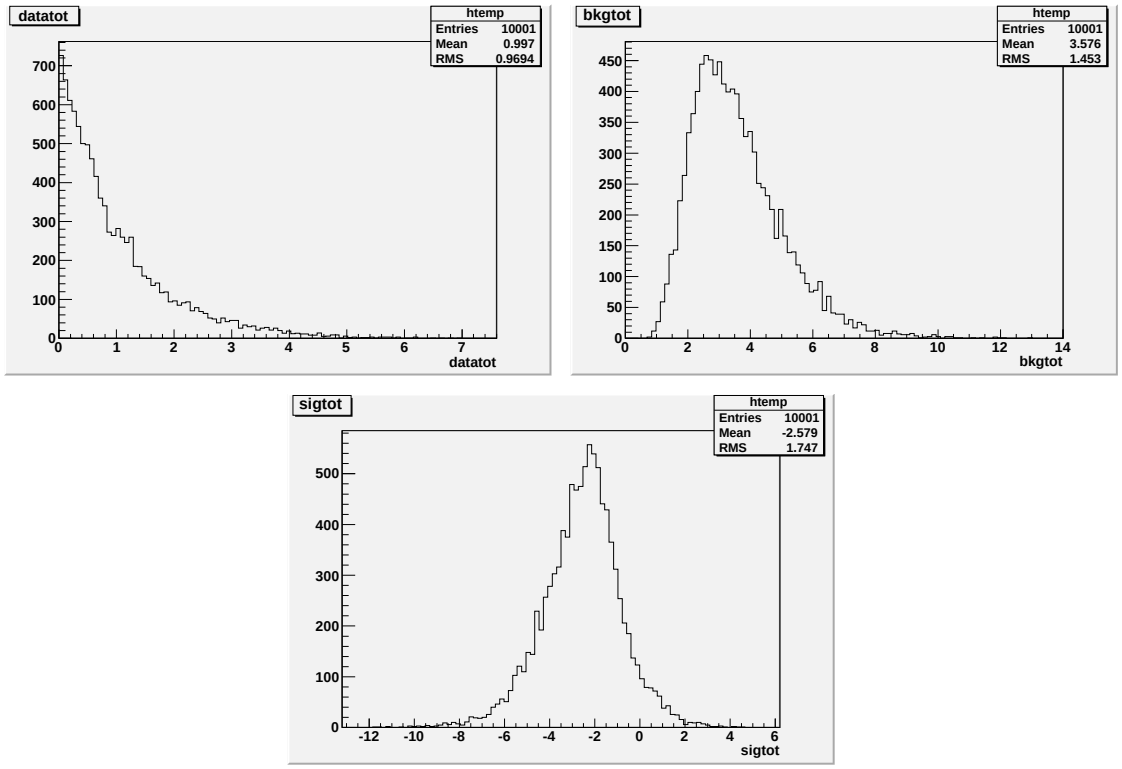


Figure 7.6: Bayesian distributions for $\langle d \rangle$ (top left), $\langle b \rangle$ (top right), and $\langle s \rangle$ (bottom), when the Monte Carlo contribution from LM0 is included in the background. The mean of the signal distribution is about 1.5 standard deviations from zero.

33.84 pb$^{-1}$ of electron-triggered data is $d = 1 \pm 1.0$ (stat).

The background in this channel due to jets that are misidentified as electrons is estimated using a data-driven technique. The electron fake rate is measured on a jet-triggered dataset, and a veto on certain jets is imposed to suppress trigger bias. Tests of the fake rate on jet-triggered and photon-triggered datasets yield agreement between prediction and observation to within $1.4\sigma$ or less. Using the fake rate method, the fake electron background in the multi-electron channel is estimated to be $q = 0.010 \pm 0.001$ (stat) $\pm$ 0.005 (sys).

The other Standard Model processes that contribute to the multi-electron

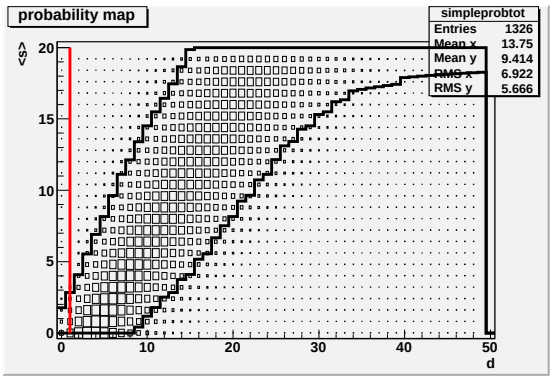


Figure 7.7: The probability map generated by the statistics simulation when the Monte Carlo contribution from LM0 is included in the background. The limits of the 95% confidence belt are marked in black. The observed data value is marked in red.

channel are due to Zjets, TTjets, WW, WZ and ZZ events. These backgrounds are estimated from Monte Carlo simulations. A correction factor for the electron reconstruction efficiency is applied, where the efficiency is measured using the tag and probe method. Systematic uncertainties due to the luminosity measurement, the NLO or NNLO cross sections, and the jet energy scale are also calculated.

The Standard Model and fake electron backgrounds are subtracted from the observation in data to obtain the signal. All of the statistical and systematic uncertainties are propagated using a toy Monte Carlo simulation. The Bayesian expected value for the signal in this channel is $\langle s \rangle = 0.238 \pm 0.996\,(\text{stat}) \pm 0.304\,(\text{sys})$. The semi-frequentist 95% confidence interval for the signal is $[0, 4.4]$. These results demonstrate that the observed data events are consistent with zero signal due to new physics processes.

The data are also compared to two low-mass points in mSUGRA parameter space, LM0 and LM1. For LM0, the predicted number of new physics events

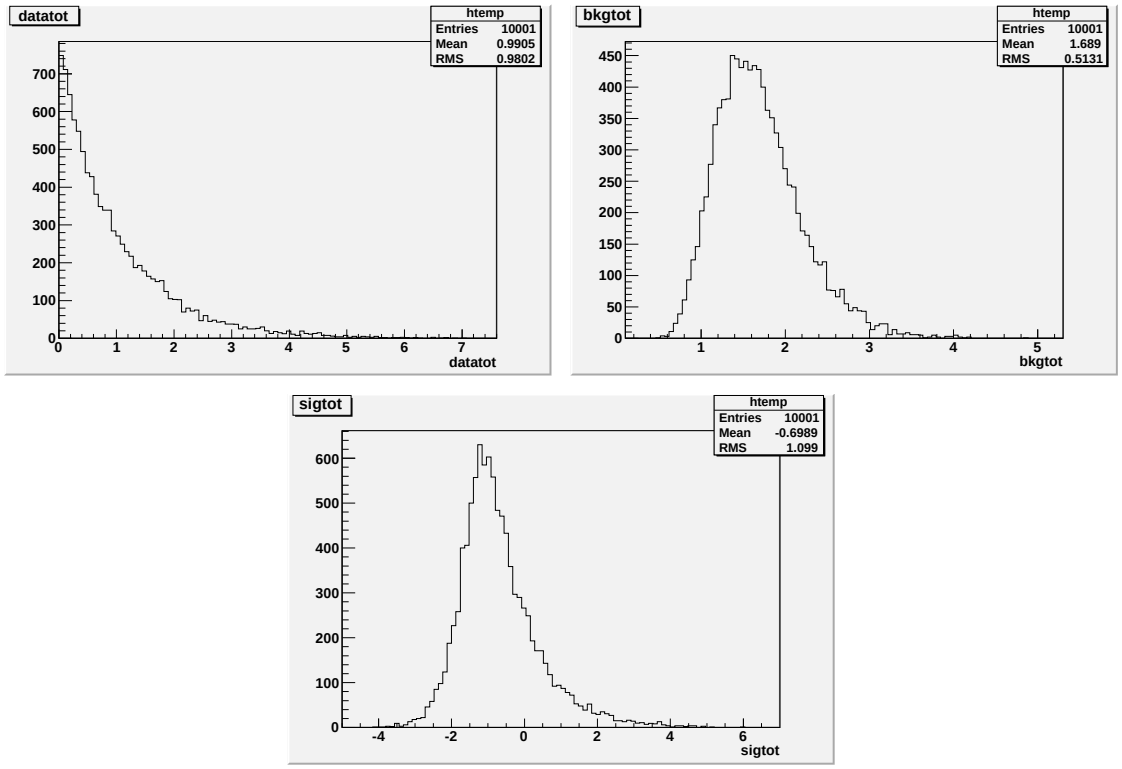


Figure 7.8: Bayesian distributions for $\langle d \rangle$ (top left), $\langle b \rangle$ (top right), and $\langle s \rangle$ (bottom), when the Monte Carlo contribution from LM1 is included in the background. The mean of the signal distribution is within one standard deviation of zero.

in the signal region is $l = 2.99 \pm 0.16$ (stat) $\pm$ 0.07 (sys). The observation in data excludes this hypothesis to approximately $1.5\sigma$. For LM1, the predicted number of new physics events in the signal region is $l = 1.00 \pm 0.03$ (stat) $\pm 0.01$ (sys). The data are consistent with this hypothesis to within less than $1\sigma$.

As more CMS observations are accumulated, the statistical uncertainties on the signal region event counts will decrease. At the same time, the understanding of systematic effects such as jet energy scale uncertainty will improve, so systematic uncertainties will also decrease. The techniques presented in this document will continue to be applicable to studies that are performed on larger quantities of integrated luminosity, where their capacity for unambiguously

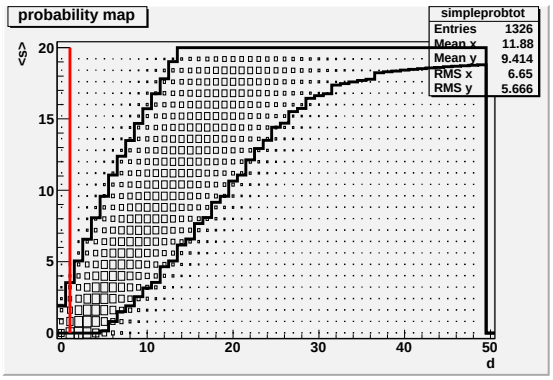


Figure 7.9: The probability map generated by the statistics simulation when the Monte Carlo contribution from LM1 is included in the background. The limits of the 95% confidence belt are marked in black. The observed data value is marked in red.

identifying new physics signals can only improve.

## BIBLIOGRAPHY


[1] "LHC Machine Outreach" (2010).
http://lhc-machine-outreach.web.cern.ch/lhc-machine-outreach/

[2] CMS Collaboration, "The CMS Physics Technical Design Report, Volume 1, Section 8.2: LHC beam parameters," *CERN/LHCC* **2006-001** (2006) 316-317.

[3] "Trigger Menu Development Group" (2011).
https://twiki.cern.ch/twiki/bin/view/CMS/TriggerMenuDevelopment

[4] CMS Collaboration, "The CMS Experiment at the CERN LHC, Section 1.1: Overall concept," *JINST* **3** S08004 (2008) 2-5.

[5] CMS Collaboration, "The CMS Physics Technical Design Report, Volume 1" *CERN/LHCC* **2006-001** (2006).

[6] CMS Collaboration, "The CMS Experiment at the CERN LHC" *JINST* **3** S08004 (2008).

[7] CMS Collaboration, "The CMS Physics Technical Design Report, Volume 1, Section 1.2: Coordinate conventions," *CERN/LHCC* **2006-001** (2006) 4.

[8] CMS Collaboration, "The TriDAS Project Technical Design Report, Volume 1, Section 1: General Overview," *CERN/LHCC* **2000-38** (2000) 1-11.

[9] CMS Collaboration, "The CMS Physics Technical Design Report, Volume 1, Section 2.3: Event Filter," *CERN/LHCC* **2006-001** (2006) 38-45.

[10] CMS Collaboration, "The CMS Experiment at the CERN LHC, Section 3.2: Pixel detector," *JINST* **3** S08004 (2008) 33-55.

[11] CMS Collaboration, "The CMS Physics Technical Design Report, Volume 1, Section 1.5: CMS: the overall concept," *CERN/LHCC* **2006-001** (2006) 7-25.

[12] S. Das [*CMS Collaboration*], "The status and performance of the CMS pixel detector," *CMS Conference Report* **2009/058** (2009).

[13] "Pixel Online Software" (2010).
https://twiki.cern.ch/twiki/bin/viewauth/CMS/PixelOnlineSoftware

[14] "TTCci User Guide" (2007).
http://cmsdoc.cern.ch/cms/TRIDAS/ttc/modules/ttcci/index.html

[15] "Pixel Online Software" (2010).
https://twiki.cern.ch/twiki/bin/view/CMS/PixelOnlineSoftwareDocs

[16] CMS Collaboration, "The CMS Experiment at the CERN LHC, Section 3.3: Silicon strip tracker," *JINST* **3** S08004 (2008) 55-89.

[17] CMS Collaboration, "The CMS Experiment at the CERN LHC, Chapter 4: Electromagnetic calorimeter," *JINST* **3** S08004 (2008) 90-121.

[18] CMS Collaboration, "The CMS Physics Technical Design Report, Volume 1, Section 4.1: Description of the ECAL," *CERN/LHCC* **2006-001** (2006) 146150.

[19] CMS Collaboration, "The CMS Experiment at the CERN LHC, Chapter 5: Hadron calorimeter," *JINST* **3** S08004 (2008) 122-155.

[20] CMS Collaboration, "The CMS Experiment at the CERN LHC, Chapter 7: The muon system," *JINST* **3** S08004 (2008) 162-246.

[21] CMS Collaboration, "The CMS Physics Technical Design Report, Volume 1, Chapter 2: Software Components," *CERN/LHCC* **2006-001** (2006) 28-91.

[22] MG/ME Development Team, "MadGraph Version 4" (2010).
http://madgraph.hep.uiuc.edu/index.html

[23] T. Sjostrand, S. Mrenna, and P. Skands, "Pythia 6.4 Physics and Manual." arXiv:hep-ph/0603175.

[24] M. Dobbs and J.B. Hansen, "HepMC: A C++ Event Record For Monte Carlo Generators," *Comput. Phys. Commun.* **134** (2001) 41.

[25] **GEANT4** Collaboration, S. Agostinelli et al., "GEANT4: A simulation toolkit," *Nucl. Instrum. and Methods* **A506** (2003) 250-303.

[26] "Physics Analysis Toolkit (PAT)" (2011).
https://twiki.cern.ch/twiki/bin/view/CMSPublic/SWGuidePAT

[27] CMS Collaboration, "The CMS Physics Technical Design Report, Volume 1, Chapter 9: Muons," *CERN/LHCC* **2006-001** (2006) 332-364.

[28] CMS Collaboration, "The CMS Physics Technical Design Report, Volume 1, Section 10.1: ECAL clustering and superclustering," *CERN/LHCC* **2006-001** (2006) 365-368.

[29] CMS Collaboration, "The CMS Physics Technical Design Report, Volume 1, Section 10.3: Photon reconstruction and selection," *CERN/LHCC* **2006-001** (2006) 375-390.

[30] CMS Collaboration, "The CMS Physics Technical Design Report, Volume 1, Section 10.4: Electron reconstruction and selection," *CERN/LHCC* **2006-001** (2006) 390-403.

[31] CMS Collaboration, "The CMS Physics Technical Design Report, Volume 1, Chapter 11: Jets and Missing Transverse Energy," *CERN/LHCC* **2006-001** (2006) 404-436.

[32] M. Cacciara and G. Salam, "The anti-$k_t$ jet clustering algorithm," *JHEP* **04** (2008) 063. arXiv:0802.1189v2.

[33] "Jet Energy Corrections" (2011).
https://twiki.cern.ch/twiki/bin/view/CMSPublic
/WorkBookJetEnergyCorrections

[34] CMS Collaboration, "Jet energy calibration with photon+jet events," *CMS Physics Analysis Summary* **JME-09-004** (2009).

[35] CMS Collaboration, "The CMS Physics Technical Design Report, Volume 1, Section 11.4: Jet resolution," *CERN/LHCC* **2006-001** (2006) 409-411.

[36] CMS Collaboration, "The CMS Physics Technical Design Report, Volume 1, Section 11.5: Missing transverse energy," *CERN/LHCC* **2006-001** (2006) 411-420.

[37] M. Peskin and D. Schroeder, "Chapter 20: Gauge Theories with Spontaneous Symmetry Breaking," *An Introduction to Quantum Field Theory*, Westview Press, Boulder (1995) 689-730.

[38] T.-P. Cheng and L.-F. Li, "Chapter 14: Grand Unification," *Gauge Theory of Elementary Particle Physics*, Clarendon Press, Oxford (1984) 428-452.

[39] A. Seiden, "Chapter 13: Physics at Higher Energies," *Particle Physics: A Comprehensive Introduction*, Addison Wesley, San Francisco (2005) 441-444.

[40] A. Zee, "Chapter 14: Grand Unification," *Quantum Field Theory in a Nutshell*, Princeton University Press, Princeton (2003) 391-415.

[41] S. Martin, "A Supersymmetry Primer" (2008). arXiv:hep-ph/9709356.

[42] M. Peskin and D. Schroeder, "Chapter 22: Quantum Field Theory at the Frontier," *An Introduction to Quantum Field Theory*, Westview Press, Boulder (1995) 781-800.

[43] K. Nakamura et al. (Particle Data Group), "Review of Particle Physics, Section 22: Dark Matter" *J. Phys. G* **37**, 075021 (2010).

[44] D.N. Spergel et al. (WMAP Collaboration), "First Year Wilkinson Microwave Anisotropy Probe (WMAP) Observations: Determination of Cosmological Parameters," *Astrophys. J. Suppl.* **148** (2003) 175. arxiv:astro-ph/0302209.

[45] M. Drees, R. Godbole, and P. Roy, *Theory and Phenomenology of Sparticles*, World Scientific Publishing Co. Pte. Ltd., Singapore (2004).

[46] M. Drees, R. Godbole, and P. Roy, "Chapter 2: Preliminaries," *Theory and Phenomenology of Sparticles*, World Scientific Publishing Co. Pte. Ltd., Singapore (2004) 19-28.

[47] S. Weinberg, "The Poincaré Algebra," *Quantum Theory of Fields*, Volume 1, Cambridge (1995) 58-62

[48] S. Coleman and J. Mandula, "All Possibly Symmetries of the S Matrix," *Phys. Rev.* **159** (1967) 1251.

[49] M. Drees, R. Godbole, and P. Roy, "Chapter 3: Algebraic Aspects," *Theory and Phenomenology of Sparticles*, World Scientific Publishing Co. Pte. Ltd., Singapore (2004) 29-48.

[50] M. Drees, R. Godbole, and P. Roy, "Chapter 4: Free Superfields in Super-

space," *Theory and Phenomenology of Sparticles*, World Scientific Publishing Co. Pte. Ltd., Singapore (2004) 49-70.

[51] M. Drees, R. Godbole, and P. Roy, "Chapter 8: Basic Structure of the MSSM," *Theory and Phenomenology of Sparticles*, World Scientific Publishing Co. Pte. Ltd., Singapore (2004) 161-182.

[52] M. Drees, R. Godbole, and P. Roy, "System of Interacting Chiral Superfields," *Theory and Phenomenology of Sparticles*, World Scientific Publishing Co. Pte. Ltd., Singapore (2004) 71-76.

[53] M. Drees, R. Godbole, and P. Roy, "Chapter 9: Soft Supersymmetry Breaking in the MSSM," *Theory and Phenomenology of Sparticles*, World Scientific Publishing Co. Pte. Ltd., Singapore (2004) 183-218.

[54] M. Drees, R. Godbole, and P. Roy, "Chapter 12: Gravity Mediated Supersymmetry Breaking," *Theory and Phenomenology of Sparticles*, World Scientific Publishing Co. Pte. Ltd., Singapore (2004) 273-322.

[55] C. Csáki, J. Hubisz, G. Kribs, P. Meade, and J. Terning, "Big Corrections from a Little Higgs," *Phys. Rev. D* **67**, 115002 (2003). arXiv:hep-ph/0211124.

[56] N. Arkani-Hamen, A. G. Cohen, and H. Georgi, "Electroweak symmetry breaking from dimensional deconstruction," *Phys. Lett. B* **513** (2001) 232. arXiv:hep-ph/0105239.

[57] H. C. Cheng and I. Low, "TeV Symmetry and the Little Hierarchy Problem," *JHEP* **0309** (2003) 051. arXiv:hep-ph/0308199.

[58] M. Perelstein, "Little Higgs Models and Their Phenomenology," *Prog. Part. Nucl. Phys.* **58** (2007) 247. arXiv:hep-ph/0512128.

[59] J. Hubisz and P. Meade, "Phenomenology of the Littlest Higgs with T-Parity," *Phys. Rev. D* **71**, 035106 (2005). arXiv:hep-ph/0411264.

[60] J. Hubisz, P. Meade, A. Noble, M. Perelstein, "Electroweak Precision Constraints on the Littlest Higgs Model with T Parity," *JHEP* **0601** (2006) 135. arXiv:hep-ph/0506042.

[61] L. T. Wang and I. Yavin, "A Review of Spin Determination at the LHC," *JHEP* **0704** (2007) 032. arXiv:hep-ph/0605296.

[62] G. Hallenbeck, M. Perelstein, C. Spethmann, J. Thom, and J. Vaughan, "Model Discrimination at the LHC: a Case Study," *Phys. Rev. D* **79** 075024 (2009). arXiv:0812.3135v3.

[63] "PGS 4: Pretty Good Simulation of High Energy Collisions" (2009). http://physics.ucdavis.edu/~conway/research/software/pgs/pgs4-general.htm

[64] R. Johnson and D. Wichern, *Applied Multivariate Statistical Analysis, Third Edition*, Prentice Hall, Upper Saddle River (1992) 140-152.

[65] L. Agostino et al., "Sensitivity study for new physics in final states with electrons, jets, and large missing $E_T$," *CMS Analysis Note* **2010/046** (2010).

[66] "Index of /cms-service-dqm/CAF/certification" (2010). https://cms-service-dqm.web.cern.ch/cms-service-dqm/CAF/certification/Collisions10/7GeV/StreamExpress/

[67] "The official CMS Luminosity Calculation" (2011). https://twiki.cern.ch/twiki/bin/viewauth/CMS/LumiCalc

[68] "Recipes for the analysis of the data from 7TeV collision of 2010" (2010). https://twiki.cern.ch/twiki/bin/view/CMS/Collisions2010Recipes

[69] "Fall 2010 CMS MonteCarlo Production (7 TeV)" (2011). https://twiki.cern.ch/twiki/bin/view/CMS/ProductionFall2010

[70] "Standard Model Cross Sections for CMS at 7 TeV" (2010). https://twiki.cern.ch/twiki/bin/viewauth/CMS/StandardModelCrossSections

[71] "Electron Identification Based on Simple Cuts" (2011). https://twiki.cern.ch/twiki/bin/view/CMS/SimpleCutBasedEleID

[72] L. Agostino et al., "Estimation of Fake Electron Background using Data-Driven Techniques," *CMS Analysis Note* **2010/043** (2010).

[73] "Photon Identification Subtask" (2010). https://twiki.cern.ch/twiki/bin/view/CMS/PhotonID

[74] The CMS Collaboration, "Measurement of CMS Luminosity," *CMS Physics Analysis Summary* **EWK-10-004** (2010).

[75] L. Agostino et al., "Validation of Electron Identification Using a $Z \to e^+e^-$ Cross Section Measurement," *CMS Analysis Note* **2010/044** (2010).

[76] G. Daskalakis, D. Evans, C.S. Hill, et al., "Measuring Electron Efficiencies at CMS with Early Data," *CMS Analysis Note*, **2007/019** (2007).

[77] K. Nakamura et al. (Particle Data Group), "Review of Particle Physics," *J. Phys. G* **37**, 075021 (2010).

[78] J. Alcaraz et al., "Updated Measurements of the Inclusive W and Z Cross Sections at 7 TeV," *CMS Analysis Note* **2010/264** (2010).

[79] G. Feldman and R. Cousins, "Unified approach to the classical statistical analysis of small signals," *Phys. Rev. D* **57** (1998), 3873-3889.